MAGNETIC-PLASMONIC MULTILAYERED NANORODS

by

ORATHAI THUMTHAN

Presented to the Faculty of the Graduate School of
The University of Texas at Arlington in Partial Fulfillment
of the Requirements
for the Degree of

DOCTOR OF PHILOSOPHY

THE UNIVERSITY OF TEXAS AT ARLINGTON

May 2015

Acknowledgements

My deep gratitude goes to Dr.Yaowu Hao, my advisor, who always supports me in every aspect of working. He introduced me to an interesting research topic as well as helped me get through many challenges during my research. I would like to express my gratitude to my committee members, Dr. Pranesh Aswath, Dr. Efstathios Meletis, Dr. Choong-Un Kim, and Dr.Fuqiang Liu, for their helpful advice in my research.

I would like to thank my labmates, Chivarat Muangphat, Punnapob Punnakitikashem, Chienwen Huang, Chiajen Hsu, Sina Moeendarbari, Shinh-Hsin Chang, Jiaqi Wu, Megha Panuganti, Rishi Wadhwa, Jingwen He, Yi-Jiun Li, Yu-jen Chiu, Akshay S Hande, and Ruiqian Jiang for their great friendship and helpful discussion. I would also like to thank Dahn Truong, Jinglei, and Ahana for their help in cell study.

I would like to thank Jennifer Standlee and Robinson Beth for their support and encouragement. And I would like to thank staff from Nanofab and CCMB for their exellent training on equipments.

Finally, I highly appreciate my family members for their inspiration, encouragement, and persistent support in every aspect.

May 1, 2015

Abstract

MAGNETIC-PLASMONIC MULTILAYERED NANORODS

Orathai Thumthan, Ph.D.

The University of Texas at Arlington, 2015

Supervising Professor: Yaowu Hao

Multilayered nanorods which consist of alternating magnetic layers separated by Au layers combine two distinctive properties, magnetic properties and surface plasmonic resonance (SPR) properties into one nano-entity. Their magnetic properties are tunable by changing the layer thickness, varying from single domain to superparamagnetic state. Superparamagnetic is a key requirement for magnetic nanoparticles for bioapplications. Superparamagnetic nanoparticles exhibit high magnetic moments at low applied magnetic field while retain no magnetic moments when magnetic field is removed preventing them from aggregation due to magnetic attraction. Au layers in the nanorods provide anchorage sites for functional group attachment. Also, Au nanodisks exhibit SPR properties. The SPR peak can be tuned from 540 nm to 820 nm by controlling the thickness of magnetic segments while keeping Au thickness constant.

In this research, three types of multilayered nanorod have been fabricated: Au/NiFe nanorods, Au/Fe nanorods, and Au/Co nanorods. These magnetic nanorods were fabricated by templated electrodeposition into the channels in Anodic Aluminum Oxide (AAO) membrane. The setup for AAO membrane

fabrication was developed as a part of this research. Our fabricated AAO membrane has channels with a diameter ranging from 40nm to 80 nm and a thickness of 10um to 12um.

Magnetic properties of nanorods such as saturation field, saturation moment, coercivity and remanence are able to manipulate through their shape anisotropy. The magnetization will be easier in long axis rather than short axis of particle. In addition, Au nanodisks in the nanorod structure are not only serving as anchorage sites for functional groups but also provide SPR properties. Under irradiation of light, Au nanodisks strongly absorb light at SPR frequency ranging from 540 nm to 820 nm by controlling the thickness of magnetic segments while keeping Au thickness constant. The SPR tunability of nanorods in near-infrared region can be used in in-vivo biomedical applications such as photo thermal therapy because tissue has an absorption maximum in the infrared range.

The magnetic nanorods were explored for the following two applications: 1) as active component orientation-tunable ferrogel for cell culture matrix, 2) as MRI contrast agent. The results show that Au/NiFe magnetic nanorods can be aligned along applied magnetic field. Using MTT assay for 3T3 fibroblast cells, the biocompatibility of Au/Co nanorods was investigated. It shows that cell proliferation after 72 hours of incubation with nanorods decreases as the concentration of nanorods increases. However, cell viability quantified by counting dead cell/live cell reveals that only few cells died after three days of incubation. Au/Co multilayered nanorods were tested as T_2 MRI-contrast agent, and a very large relaxivity was observed.

In summary, we have successfully fabricated multilayered nanorods with tunability in both magnetic and SPR properties. These nanorods can potentially be used in biological and biomedical fields.

Table of Contents

List of Illustrations

List of Tables

Chapter 1

Introduction

Using magnetic nanoparticles for biological and biomedical applications can be traced back to more than a half century ago[1]. Magnetic nanoparticles for magnetic cell separation[2] and magnetic resonance imaging (MRI) contrast enhancement agents[3, 4] have been routinely used in biological research and medical diagnostics. In the last decade, explorations of other bioapplications of magnetic nanoparticles such as targeted drug and gene delivery [5-7], hyperthermia treatment[3, 8-10], biophysical studies [11-14] and biosensors have attracted unprecedented attention.

Currently, superparamagnetic iron oxide nanoparticles are commercially available for MRI contrast agents and magnetic cell separation. For MRI, small iron oxide particles (<20 nm) coated with a biocompatible polymer are usually used. For cell separation, large (>1 μm) spherical beads consisting of dispersed iron oxide particles in a polymer matrix are commonly used to get enough magnetic moment. Most research on other new biomagnetic applications has conveniently utilized these magnetic nanoparticles, and has produced many promising results. To overcome the most prominent shortcoming of iron oxide nanoparticles, their low saturation magnetization (typically 80 emu/g), recent research on magnetic nanoparticles for bioapplications has been focused on core-shell-type superparamagnetic nanoparticles with high saturation moment materials such as Co (160 emu/g), Fe (190 emu/g) and FeCo (235 emu/g) as the core and biocompatible materials such as Au, silicon oxide or iron oxide as the shell to shield core materials' corrosiveness and toxicity and provide functionalization sites.

However, at room temperature the superparamagnetic phenomenon only occurs in very small nanoparticles. For example, the critical sizes at which superparamagnetic occurs at room temperature are estimated as 7 nm for Co and 6 nm for Fe. Small size particles generate small net magnetic moments. For some biomagnetic applications such as magnetic biosensing, bioseperation, cell and DNA mechanics, and drug and gene targeted delivery, there exists a minimum net magnetic moment requirement for individual particles to generate enough magnetic signals or magnetic forces. To obtain a high magnetic moment, simply making particles larger cannot be an option at all, resulting in a strong aggregation due to magnetic attraction since particles are no longer superparamagnetic. Embedding multiple nanoparticles in a matrix can generate large magnetic moment while still keeping superparamagnetic characteristics, but the size of the entire particle becomes very large due to the low percentage of embedded magnetic nanoparticles, typically 10-20 %, to avoid magnetic interactions between nanoparticles. After the requirement for net magnetic moment is satisfied, the size of the particles becomes a very important concern, usually the smaller the better. Therefore, for many biomagnetic applications, available and under-development superparamagnetic particles are either too small (< 20nm) to possess enough magnetic moment or too big (> 100nm) to have desired optimum performances.

In this dissertation, a new type of magnetic particles, together with their fabrication methods and several applications, are described. In these nanoparticles, two key magnetic requirements for bioapplications, a high saturation magnetic moment and a near zero remanent moment are achieved by a non-superparamagnetic mechanism, namely, the magnetostatic coupling between magnetic layers. These high moment nanoparticles can fill the superparamagnetic nanoparticle size gap, from 20 nm to 100 nm. To produce large quantities of these multilayered magnetic nanoparticles, a template electrodeposition process is proposed. The process involves the fabrication of Anodic aluminum oxide membrane which is used as templates for electrodeposition.

Two particular applications using different types of multilayered magnetic nanoparticles have been explored: as active components in orientation-adjustable hydrogel for cell culture; as MRI contrast agent.

Abovementioned multilayered nanoparticles comprising of alternating magnetic layers separated by Au nanodisks. In the last decade, gold nanoparticles have been a subject of intensive research for their surface plasmon resonance properties, and their bioapplications.

Surface plasmon resonance is a nanoscale size effect of the interaction of an electromagnetic wave with the conduction electrons in a metal. When a metal is under the irradiation of light, the electric field drives the conduction electrons to oscillate. This collective motion of electrons has its resonance frequency, plasma frequency, and the quanta of this collective oscillation are called plasmons. When dimensions (at least one) of the metal is much smaller than the wavelength of the light, this collective excitation mode of the plasma will be localized near the surface, and the resonant frequency will shift from the ordinary plasma frequency to Surface Plasmon Resonance (SPR) frequency. The SPR frequencies lie in visible light range for Cu, Ag and Au nanoparticles. The incident light at SPR frequency is strongly absorbed by these metal nanoparticles, giving them intense colors and other interesting optical properties. Some of the absorbed photons will be released with the same frequency in all directions, which is known as scattering; some photons will be converted into phonons, which is referred to as absorption. The SPR frequency and cross-section of SPR scattering and absorption are dependent on the size and shape of nanoparticles, inter-particle interactions and dielectric properties of the surrounding medium.

A theoretical study on Au nanodisks has predicted that two SPR peaks exist corresponding to the oscillation along its long axis (in disk plane) and short axis (perpendicular to the disk plane), and the long axis SPR peak exhibits a large red shift (to longer wavelength) with the increase of the diameter of the disks, very similar to the transverse (along short axis) and longitudinal (along long axis) SPR peaks for nanorods. The multilayered magnetic nanoparticles proposed above are just the combination of Au nanodisks and a magnetic segment. Here, we can combine SPR properties from Au nanodisks with magnetic properties from magnetic segments. This dual-functionality will have a great impact on biological research and biomedical diagnostics. For example, a diseased cell identified by the optical microscope can be immediately separated for further diagnostic analysis.

The outline of this dissertation is as follows. Chapter 2 provides brief background information on the magnetic nanoparticles, optical properties of Au, and anodization of Al. In chapter 3, the fabrication of AAO templates is presented. In chapter 4 the fabrication conditions for multilayered nanodisks are provided. The magnetic properties of multilayered nanodisks are discussed in chapter 5. The optical properties are presented in chapter 6. In Chapter 7, the preliminary studies of their applications are provided, and finally the major scientific contributions from this research are summarized in chapter 8.

Chapter 2

Background Information

In this chapter, the general information about magnetic properties of nanoparticles is introduced, and a brief description on optical properties of Au is also provided. Finally, the aluminum anodization process and its conditions are described

2.1 Magnetics

2.1.1 Energy Terms Associated with Magnetic Nanostructures

Thermal energy: kT, acts to randomize the directions of magnetization.

Exchange energy: exchange energy measures the interaction of spin between two electrons. For ferromagnetic and ferrimagnetic materials, which are usually referred as magnetic materials, this energy will reach minimum value when magnetic moments aligned parallel to each other.

Zeeman energy: Zeeman energy is the magnetic potential energy, the tendency of magnetization to align in an external magnetic field. Zeeman energy is given by

$$E_Z = -\vec{H}_{ext} \cdot \vec{M} \tag{2.1}$$

where $\vec{H}_{ext}$ is external applied field vector, and $\vec{M}$ is magnetization vector. Zeeman energy is minimal when magnetization is parallel to the external field direction.

Magnetostatic energy: In any magnetized magnetic specimen with free surfaces, there is a demagnetizing field inside the specimen which is in the opposite direction of magnetization direction. This magnetic potential energy is called magnetostatic energy. To reduce the magnetostatic energy, permanent magnet tends to break into domains. The demagnetizing field is dependent on the shape of the specimen, and is proportional to the magnetization, and is given by

$$E_{ms} = \frac{1}{2} H_d M = \frac{1}{2} N_d M M = \frac{1}{2} N_d M^2 \tag{2.2}$$

where N_d is demagnetizing factor, determined by shape. M is magnetization. (More discussion about magnetostatic energy can be found in shape anisotropy).

Anisotropy energy: In most crystalline magnetic materials, magnetization tends to align to a preferential crystallographic direction. This is called magnetocrystalline anisotropy. The uniaxial anisotropy energy density is given by

$$E_{ani} = K_{u1} \sin^2 \theta + K_{u2} \sin^4 \theta \tag{2.3}$$

where K_{u1} and K_{u2} are anisotropy energy constants, and θ is angle between magnetization direction and easy axis orientation. In cubic system, an isotropy energy density can be expressed as

$$E_{ani} = K_1 (\alpha_1^2 \alpha_2^2 + \alpha_2^2 \alpha_3^2 + \alpha_3^2 \alpha_1^2) + K_2 (\alpha_1^2 \alpha_2^2 \alpha_3^2) \tag{2.4}$$

where K_1 and K_2 are anisotropy constant, and α_1, α_2, and α_3 are the projections of unit vector on three crystalline easy axes. HCP Cobalt has a uniaxial crystalline anisotropy with easy axis in basal plane [0001] direction while FCC Ni and BCC Fe have a cubic crystalline anisotropy with easy axis in [111] direction for Ni and [100] direction for Fe.

2.1.2 Shape Anisotropy

There is also another type of anisotropy, shape anisotropy. Spherical specimen with no crystalline anisotropy will have the same magnetization in any direction after it is magnetized by applied field. For non-spherical specimen with no crystalline anisotropy, magnetization direction points to the elongated axis of specimen to have smaller magnetostatic energy. This phenomenon is called shape anisotropy.

If a rod-shaped specimen is subjected to a uniform magnetic field, as shown in Figure 2.1, the specimen will be magnetized with north pole and south pole at each end. Magnetic field goes from north pole to south pole as seen from outside. However, inside this specimen, the magnetic field also goes from north pole to south pole which opposes the magnetization of the material. The opposed field inside material will demagnetize the specimen and known as demagnetizing field, H_d.

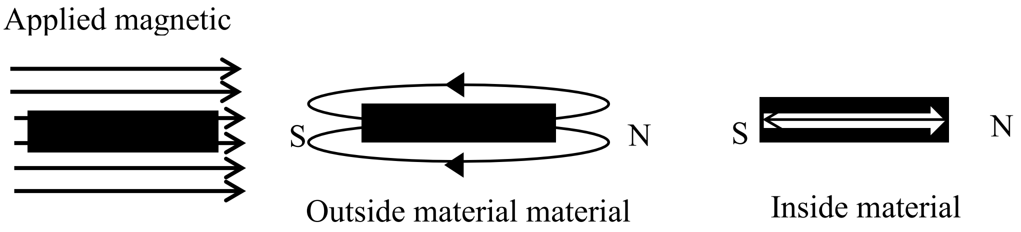

Figure 2.1 Ferromagnetic materials in uniform magnetic field

Demagnetizing field opposes the magnetization which creates it and can be defined as

$$\overrightarrow{H} = -N_d \overrightarrow{M} \tag{2.5}$$

where N_d is magnetizing factor and depends on the shape of the specimen.

The magnetostatic energy E_D (erg/cm^3) in specific direction of magnetization can be written as

$$E_D = \frac{1}{2} N_d M_s^2 \tag{2.6}$$

where M_s is saturation magnetization of material (emu/cm^3)

Shape anisotropy in ellipsoid

In a general ellipsoid, where 3 axes a, b, and c, $c \geq b \geq a$, the demagnetizing factors along these axes are designated as N_a, N_b, and N_c, respectively. $N_a + N_b + N_c = 4\pi$.

There are three special types of ellipsoids, as shown in Figure 2.2: prolate spheroid, slender ellipsoid, and oblate spheroid. The demagnetizing factors for each case are provided below.

1) Prolate spheroid (c>a=b), m=c/a

$$N_a = N_b = 4\pi \frac{m}{2(m^2-1)} \times [m - \frac{1}{2(m^2-1)^{1/2}} \times \ln(\frac{m+(m^2-1)^{1/2}}{m-(m^2-1)^{1/2}})] \tag{2.7}$$

$$N_C = 4\pi \frac{1}{m^2-1} \times [\frac{m}{2(m^2-1)^{1/2}} \times \ln(\frac{m+(m^2-1)^{1/2}}{m-(m^2-1)^{1/2}}) - 1] \tag{2.8}$$

2) Slender ellipsoid (c>>b>a), m=c/a

$$N_a = 4\pi \frac{b}{a+b} - \frac{1}{2}\frac{ab}{c^2}\ln(\frac{4c}{a+b}) + \frac{ab(3a+b)}{4c^2(a+b)} \tag{2.9}$$

$$N_b = 4\pi \frac{a}{a+b} - \frac{1}{2}\frac{ab}{c^2}\ln(\frac{4c}{a+b}) + \frac{ab(a+3b)}{4c^2(a+b)} \tag{2.10}$$

$$N_C = 4\pi \frac{ab}{c^2}[\ln(\frac{4c}{a+b}) - 1] \tag{2.11}$$

3) Oblate spheroid (c=b>a), m=c/a

$$N_a = 4\pi \frac{m^2}{m^2-1}[1 - \frac{1}{(m^2-1)^{1/2}} \times \arcsin\frac{(m^2-1)^{1/2}}{m}] \tag{2.12}$$

$$N_b = N_c = 4\pi \frac{1}{2(m^2-1)} \times [\frac{m^2}{(m^2-1)^{1/2}} \times \arcsin\frac{(m^2-1)^{1/2}}{m} - 1] \tag{2.13}$$

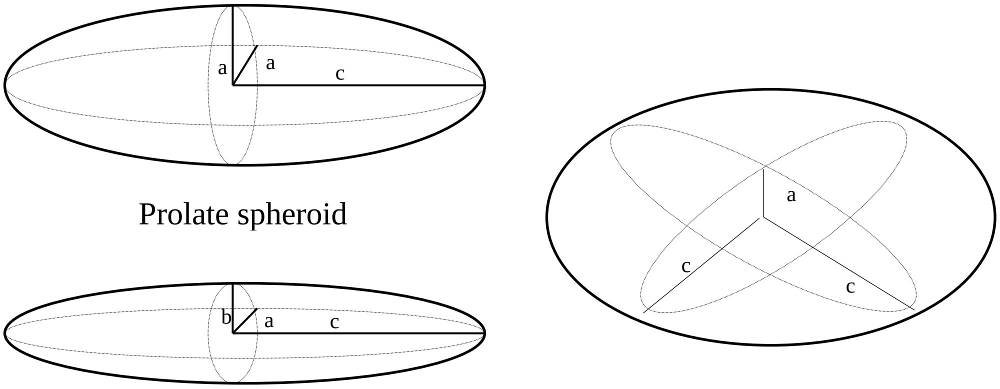

Prolate spheroid

Slender ellipsoid

Oblate spheroid

Figure 2.2 Schematic drawing of ellipsoid

2.1.3 Size Effect of Magnetic Properties of Nanoparticles

As the size of the particles decreases, magnetic particles change from multi domain to single domain, and further to superparamagnetic.

Multi domain particles

Domains are the region where magnetic moments are aligned in parallel, and are separated from each other by domain walls. In a bulk magnetic material, usually multi domain structures are present. The size and shape of domains are determined by considering exchange energy, magnetostatic energy, and anisotropy energy of the system. Balance between exchange energy and anisotropy energy determines the thickness of domain walls, of which the minimum energy is achieved. As the volume of the magnetic particles decreases, size of domain and width are reduced which lead to the increase of the domain wall energy. If the volume continues to decrease, domain wall energy may increase too much, and become larger than the reduction of magnetostatic energy. In this case, because the total energy does not get reduced, the particle no longer divides into domains but maintains single domain.

Single domain particles

The critical size where magnetic particles will stay as a single domain has range in a few tens of nanometers and depends on the saturation magnetization of

the particle, anisotropy energy and exchange energy. The critical diameter of spherical particle, D_c, when it reaches a single domain state is given by

$$D_C = 18\sqrt{AK_a}/(\mu_0 M^2) \tag{2.14}$$

where A is the exchange constant, K_a is anisotropy constant, μ_0 is the vacuum permeability, and M is saturation magnetization. The critical diameter of spherical Fe and Ni particles are 15nm and 55nm, respectively.

Superparamagnetic particles

Magnetic nanoparticles are extensively used and explored in biology and data storage fields which particle size, shape composition, and surface chemistry controlling are crucial to the desired magnetic properties [15]. To increase storage capacity in recording media the number of bits per square inch must increase causing the bit size must decrease until it reaches superparamagnetic limit which it becomes thermal unstable so that high coercivity media are required to allow smaller bit to be stable [16]. Therefore, in recording media industry the magnetic materials with high magnetic moment and high coercivity are required. In 1990, one of the earliest suggestions, magnetic nanowire arrays can be used as a future magnetic recording media [17]. The geometry of nanowires suggests that shape anisotropy prefers perpendicular alignment of magnetization and this recording media called perpendicular media [18]. The interested nanowire arrays compost of the single component ferromagnetic nanowires [19, 20] and the multi-segmented or multilayered of ferromagnetic (Fe, Ni, Co) and non-magnetic materials (Au, Pt, Cu) nanowires [21-25].

However, in bioapplications the high magnetic moment and high coercivity materials are not applicable, because of aggregation of magnetic nanoparticles due to magnetic attraction, and new magnetic state is preferred called superparamagnetic. Superparamagnetic nanoparticles possess remarkable magnetic susceptibility which exhibit high saturation magnetization at low magnetic field and no remanent moment when magnetic field is removed so that solving aggregation of nanoparticles [26]. In 1930, first prediction of a critical particle size of a superparamagnetic nanoparticle of ferromagnetic material was given by Frankel and Dorfman and stated that critical radius for common material is below 15 nm [27]. In 1996, Lesli-Pelecky and Rieke determined the critical radius of Fe nanosphere for superparamagnetic at r = 6 nm when anisotropy energy ($K\frac{4}{3}\pi r^3$) is lower than about 10 times of thermal energy (kT) [28].

Superparamagnetism occurs only in a very small nanoparticle at room temperature, such as 7nm, Co and 6nm Fe particles. In these particles, the magnetic anisotropy energy which is proportional to the volume of the particle determines the direction of magnetization. As particle size decreases this energy decreases to be comparable with thermal energy so that magnetization will become random in response to thermal fluctuation, which leads to zero remanence and zero coercivity. Superparamagnetic nanoparticles do not experience aggregation due to the magnetic attraction. Therefore, superparamagnetic behavior is a desirable property for biomedical applications.

The switching of magnetization in a magnetic nanoparticle from one direction to opposite direction can be considered as a thermally activated process. In a superparamagnetic nanoparticle, the thermal energy is large enough to overcome anisotropy energy, KV, and causes fluctuation of the magnetization direction. This energy barrier ΔE is related to anisotropy energy. The switching probability per unit time, r, can be described by Arrhenius relation.

$$r = f_0 e^{-\frac{\Delta E}{kT}} \tag{2.15}$$

where f_0 is thermal attempting frequency, typical value is $10^9\ s^{-1}$, ΔE is energy barrier, k is Boltzmann constant, and T is temperature.

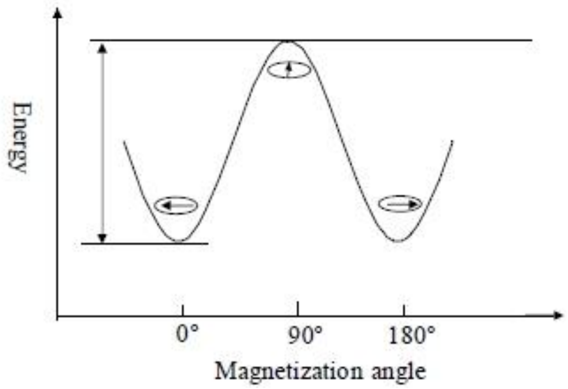

Figure 2.3 Process of magnetization switching in superparamagnetic

2.1.4 Hysteresis Loops

If a ferromagnetic or ferrimagnetic material is placed in a magnetic field, one often sees hysteresis loop which shows the irreversibility in the magnetization process. The shape of hysteresis loop is influenced by particle size. For large multidomain particles, a narrow hysteresis loop is usually observed, since it takes relatively small field to move the domain walls. On the other hand, for smaller single-domain particles, a broad hysteresis loop is usually observed because the magnetization change comes from the rotation of all spins aligned in the same direction, which requires much larger applied magnetic field. For superparamagnetic particles where the magnetic moment of particles as a whole is free to fluctuate in response to thermal energy while the individual atomic moments maintain their ordered state relative to each other, one can see anhysteretic, but still sigmoidal M-H curve.

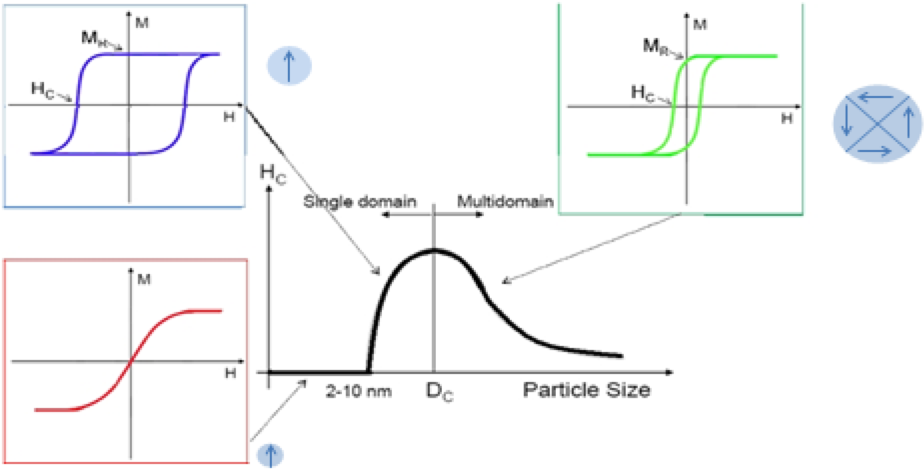

Figure 2.4 Hysteresis loops of multi domain, single domain and superparamagnetic particle

2.2 Optical Properties of Gold

Surface Plasmon Resonance (SPR) properties of gold nanostructures have attracted the extensive research interests in the last decade. SPR is an optical phenomenon resulting from the interaction between an electromagnetic wave and the conduction electrons in a metal [10]. Under the irradiation of light, the conduction electrons in gold nanostructure are driven by electric field to collective oscillate at a resonant frequency relative to the lattice of positive ions. The incident light is absorbed by the nanostructure at this resonant frequency. Some of the photons will be released with the same frequency in all direction which is known as scattering. At the same time, some of these photons will be converted into phonon which is known as absorption. Generally, SPR peak of Au nanostructures include both scattering and absorption components. The cross-sections of these two components depend on the size and shape of nanostructure.

The SPR spectra of Au nanostructures can be calculated by solving Maxwell's equations. For spherical particles, the calculation of the total cross-section was accomplished by Gustav Mie, a German physicist, in 1908, called Mie theory [29],

$$C_{ext} = \frac{24\pi^2 R^3 \varepsilon_m^{3/2}}{\lambda} \frac{\varepsilon_2}{(\varepsilon_1 + 2\varepsilon_m)^2 + \varepsilon_2^2} \tag{2.16}$$

where ε_m is the dielectric constant of the surrounding medium, $\varepsilon = \varepsilon_1 + i\varepsilon_2$ is the complex dielectric constant of the particle. From equation 2.16, it can be seen that a resonance peak occurs when $\varepsilon_1 = -2\varepsilon_m$.

Richard Gans in 1912 [30] modified Mie theory for Au nanorods, which is as follows:

$$C_{ext} = \frac{2\pi V}{3\lambda} \varepsilon_m^{3/2} \sum_j \frac{(1/P_j^2)\varepsilon_2}{(\varepsilon_1 + \frac{1-P_j}{P_j}\varepsilon_m)^2 + \varepsilon_2^2} \tag{2.17}$$

where V is the volume of the rod, P_j (j=A, B, C; A>B=C, A =length, B=C=width) are the depolarization factors for the nanorods, which are given by

$$P_A = \frac{1-e^2}{e^2}[\frac{1}{2e}\ln(\frac{1+e}{1-e}) - 1] \tag{2.18}$$

$$P_B = P_C = \frac{1-P_A}{2} \tag{2.19}$$

where e is referred to as the rod ellipticity given by $e^2 = 1-(A/B)^{-2}$.

2.3 Anodization of Aluminum

Anodization of bulk aluminum such as aluminum foil or aluminum sheet under a dc constant potential in acidic electrolyte can produce a highly ordered porous aluminum oxide in a hexagonal close-packed array as shown in Figure 2.5. Each hexagonal cell contains a cylindrical pore

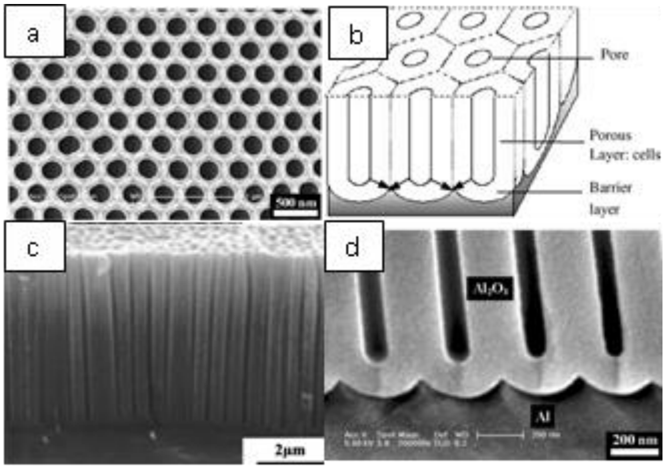

Figure 2.5 SEM of (a) bottom side after pore opening [31], (b) pore geometry [32],(c) SEM cross-section view [33],(d) SEM of U-shape at bottom side [31].

The characteristics of porous AAO membrane are defined by pore diameter, inter pore distance or cell size (DC) thin barrier layer at bottom, and pore wall. Cell size can be controlled by anodizing potential and the types of electrolyte. AAO cell size ranges from 50-500nm as shown in Figure 2.6 [34]. According to the potentials applied, the anodization processes can be classified into two categories: conventional mild anodization (MA) and high field hard anodization (HA). In MA region, cell diameter is linearly proportional to anodizing potential ranging from 50nm to 100 nm and from 400-500 nm, and HA in oxalic acid fills the gap of 200-300nm that could not be obtained for conventional MA.

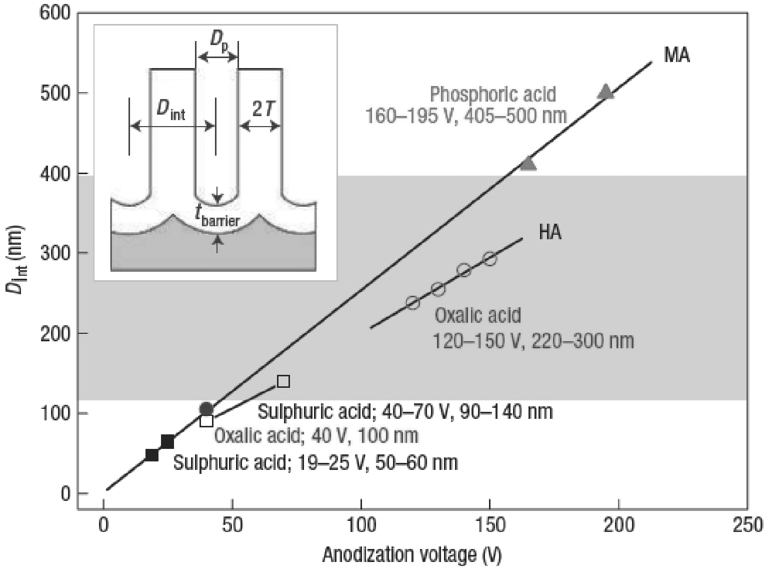

Figure 2.6 Range of cell diameter made with different anodizing potential [34]

2.3.1 Pore Formation in Porous Aluminum Oxide

A hexagonal-shaped cell can be formed by anodizing aluminum at a constant current density or constant potential. Typical current density-time and anodizing potential-time transients recorded during the anodization of aluminum with the schematic illustrations of kinetics of porous oxide growth are shown in Figure 2.7.

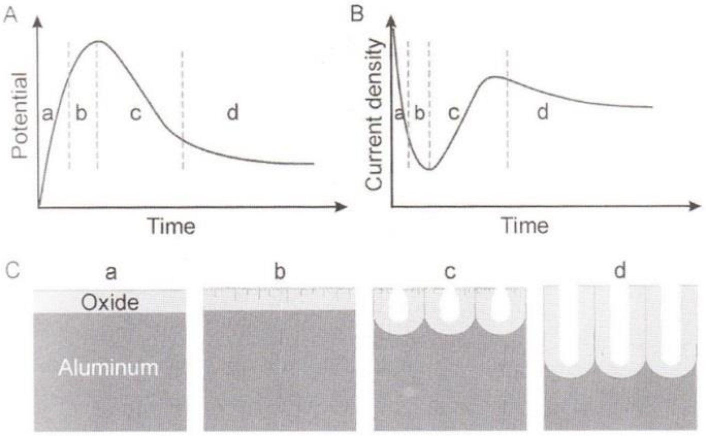

Figure 2.7 Schematic illustrations of porous oxide growth in (A) constant current, (B) constant potential, and pore formation in each stage (C) [35].

At the start of the process under constant applied potential (stage a), current density rapidly decreases with time because of a linear growth of high resistant oxide film (barrier film) on aluminum. Further anodizing (stage b) causes the propagation of individual paths through the barrier film. At local minimum of current density (stage c), the breakdown of a tight barrier film occurs and a porous structure begins to be produced. Finally, the steady- state growth of anodic porous alumina proceeds (stage d) and the current density is remained constant.

The balance between formation of aluminum oxide in Al/oxide layer interface and the dissolution of aluminum oxide in oxide/electrolyte interface enable a vertical growth downward into Al metal. The chemical reactions during oxide formation and dissolution were written as:

Formation of aluminum oxide

$$2Al(s) + 3H_2O \rightarrow Al_2O_3(s) + 6H^+(aq) + 6e^- \qquad (2.20)$$

Dissolution of aluminum oxide

$$Al_2O_3(s) + 6H^+(aq) + 3H_2O \qquad (2.21)$$

These processes involve the diffusion of oxide carrying ions (O^{2-} , OH^-) and Al anions (Al^{3+}) which are diffusing in opposite direction as shown in Figure 2.8.

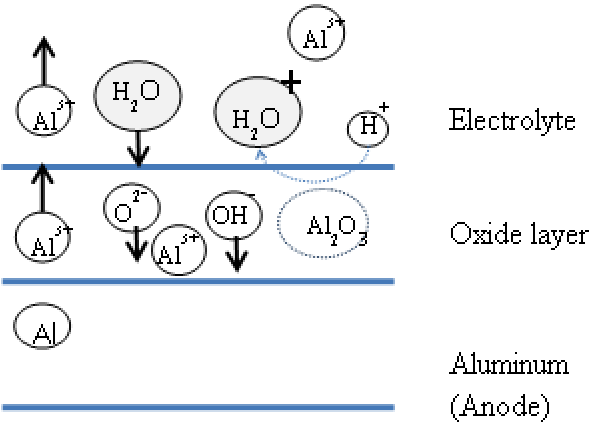

Figure 2.8 Schematic diagram of ions migrate inside the oxide layer.

Net diffusion of Al^{3+} across oxide layer is

$$Al(s) \rightarrow Al^{3+}(aq) + 3e^{-} \tag{2.22}$$

These electrons are diffused to electrolyte and reduce protons so that net diffusion of Al^{3+} across oxide layer is

$$6H^{+}(aq) + 2Al(s) \rightarrow 2Al^{3+}(aq) + 3H_2 \tag{2.23}$$

2.3.2 Highly Ordered Self-Ordering AAO Membrane

High quality AAO membranes can also be obtained. Three practical processing issues have direct effects on the quality of AAO.

First, the cleaning processes. There are three main cleaning methods To prepare Al foil for anodization 1) Al foil was degreased its surface with acetone, ethanol and isopropanol which is basic procedure for every anodization, 2) Al foil was annealed at 500 ^{0}C for 4h in Argon atmosphere [36] to increase the domain size of porous structures, and 3) Al foil was treated to reduce surface roughness by electropolishing [31-32, 34, 37-40] under constant current in the mixture of $HClO_4$ and ethanol, chemical polishing and alkaline degreasing [34].

Second, the purity of Al foil. High-purity (99.99%) aluminum sheets or foils are widely used for making AAO. Recently, in 2013, Marta et.al [41] attempted to reduce the cost by using AA1050 (99.95%) foil which is much cheaper than that of the high purity aluminum. The fabrication conditions that they suggested are; 1) 2 step-anodization in the mixture of sulfuric acid 0.3M, water and glycol with 3:2 v/v, 2) anodizing potentials are varying from 15, 20, 30, and 35V, 3) temperature constant at -1 ^{0}C, anodizing time are 17 h for 1st anodization and 30 min for 2nd anodization. They claimed that there are no significantly difference in pore size distribution in both high purity and low purity aluminum as shown the Figure 2.9.

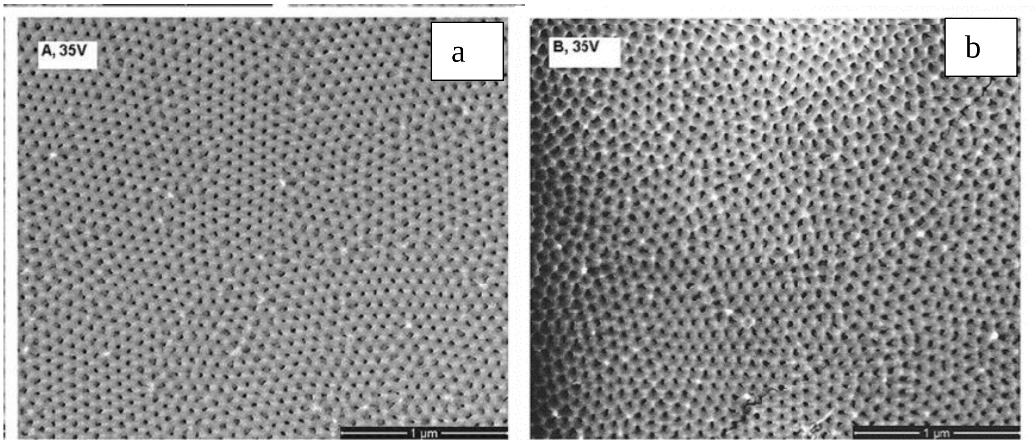

Figure 2.9 SEM micrographs top view of AAO membrane generated from a) high purity aluminum and b) low purity aluminum at 35V [41].

Third is the electric field during anodization. Recently, it is found that a highly ordered self-ordering of pore arrangement in AAO membrane can be achieved at the maximum voltage required to induce high current density, which is called anodization at high field or hard anodization (HA) [31-32, 34, 39].

A high anodizing potential, for instance, 195V in 3M tartaric acid [32] and 150V in 0.3M oxalic acid [34], is needed. The rapid growth of porous oxide layer under a high field induces a compressive force at the barrier layer between each cell boundary as shown in Figure 2.10a. The bottom of each cells press against each other to obtain the highly ordered self-ordering porous structures. The cell arrangement under low field and high field are illustrated as in Figure 2.10b.

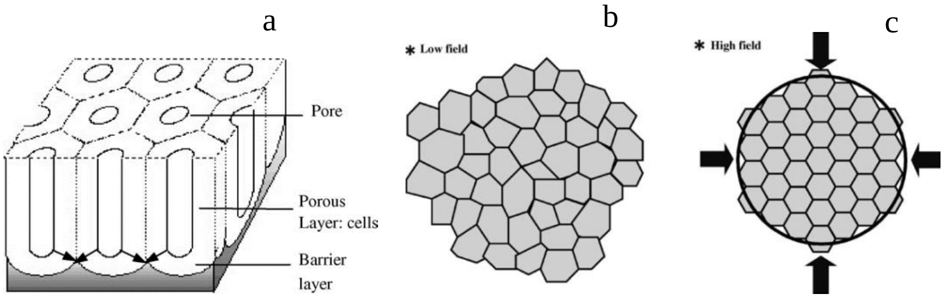

Figure 2.10 Model structure of AAO (a), illustration of cells under low field (b) and under high field (c) [32]

During anodization under high field, high current density was generated as well as a heat that was building up at pore bottom due to Joule heating in oxide/electrolyte interface, leading to a phenomenon called burning. Burning happens when the extremely high current flow at local spots leading to local thickening of oxide film. During burning vigorous gas evolution occurs at the entire surface [32-33, 41-42]. The burning area exhibits a dark area at the edge of specimen as shown in the inset of Figure 2.11 a.

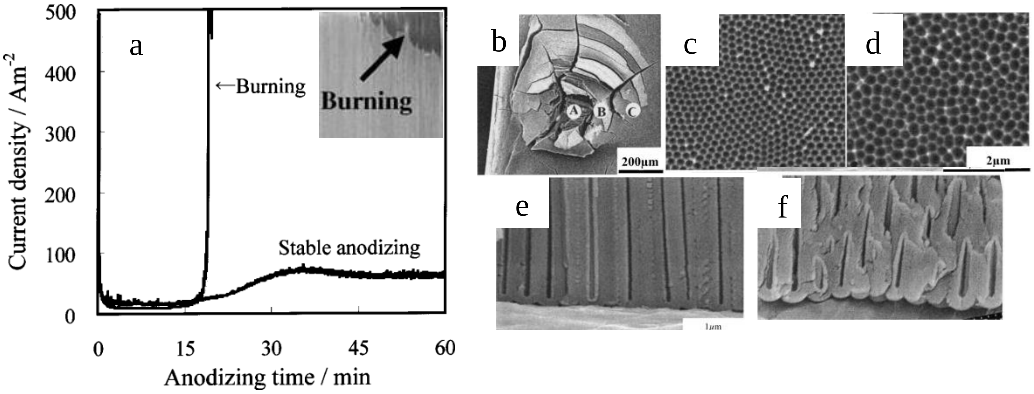

Figure 2.11 Current density during burning (a), (b) SEM micrograph of burning area, (c)SEM top-view of the center spot of burning (point A in b), (d) top view of its edge (point C in b), (e) cross-sectional view of point A, (f) cross-section view of point C [32-33]

From top view SEM micrographs it shows that even at burning area the high self-ordering still can be maintained but with different barrier layer thickness. It was reported that the barrier layer thickness at point A was 150nm and further from the center at point C the barrier layer was 216nm [33].

Chapter 3

Fabrication of Anodic Aluminum Oxide (AAO) Templates

AAO templates are considered as one of the ideal deposition templates for mass production of nanomaterials ranging from a few ten of nanometers of nanodisks to nanowires with a very high aspect ratio without the use of the expensive lithographical instruments. The inter pore distance can be adjusted from 50-500nm [34] by the selection of electrolytes, anodizing potential, pH and temperature.

This chapter mainly focuses on the fabrication process that has developed in our lab in order to meet the requirement of desired nanostructures, nanodisks with a diameter around 100nm. Experiments were carried out to determine the effect of processing parameters on the pore diameter of AAO membranes.

3.1 Anodization Setup

The electrochemical cell consists of a Pt mesh as cathode and an Al foil as anode. The electrodes are connected to a DC power supply. The distance between two electrodes is at 2.5”. To prevent high current density at local spot which causes a burning on AAO membrane, a copper plate and copper rod are attached to Al foil. Hydrogen bubbles are generated during the process and tend to agglomerate into a big bubble which causes a drop in current density so that a rotator is employed to stir the electrolyte to prevent the formation of larges hydrogen bubbles. The anodization was conducted under a constant temperature at 4 °C. The DC power supply was controlled by a computer using LABVIEW software. After anodizing potential was applied the transient of current density was recorded. The anodization setup is shown in Figure 3.1.

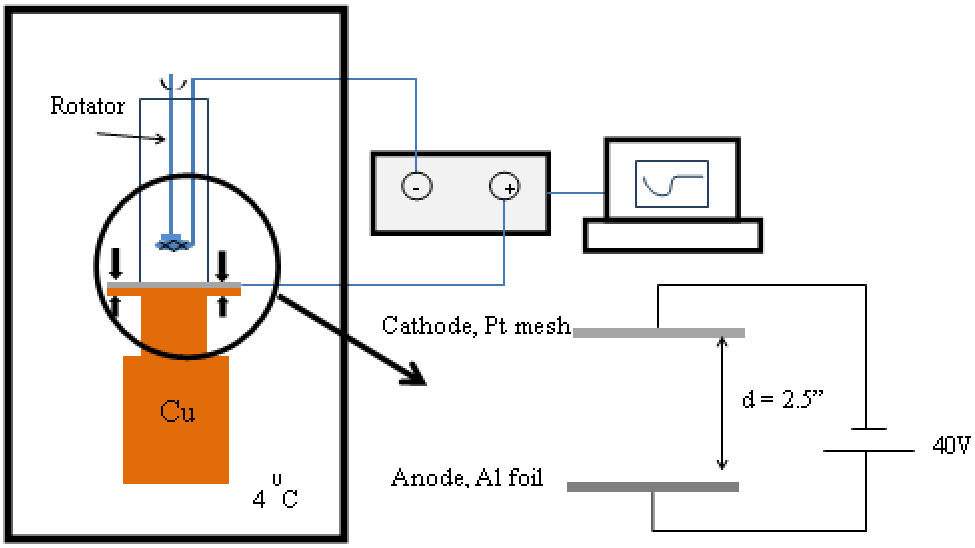

Figure 3.1 Schematic diagram of anodization unit

3.2 Anodization Process

Experimental procedures are described in Figure 3.2. Firstly, aluminum foil with purity 99.45% was cut into 2x2 cm^2. Then it was placed on a copper plate which was attached to a copper rod. The glass vessel was used as the anodization cell, and the O-ring was used to prevent the leakage and allowed Al foil with area of 1.77cm^2 exposed to the electrolyte. Next, Al foil in the cell was cleaned with acetone and then ethanol to get rid of grease on the surface. After rinsed with DI water, the cell was placed in the freezer for 10 minutes to make the copper rod cold enough before the anodization. 0.23M oxalic acid was poured into the cell and then the cell was placed inside a refrigerator. The cell was connected to power supply which was controlled by a computer. Anodization of Al was then carried out under a constant anodizing voltage of 40V for 6 hours at temperature of 4 ^{o}C.

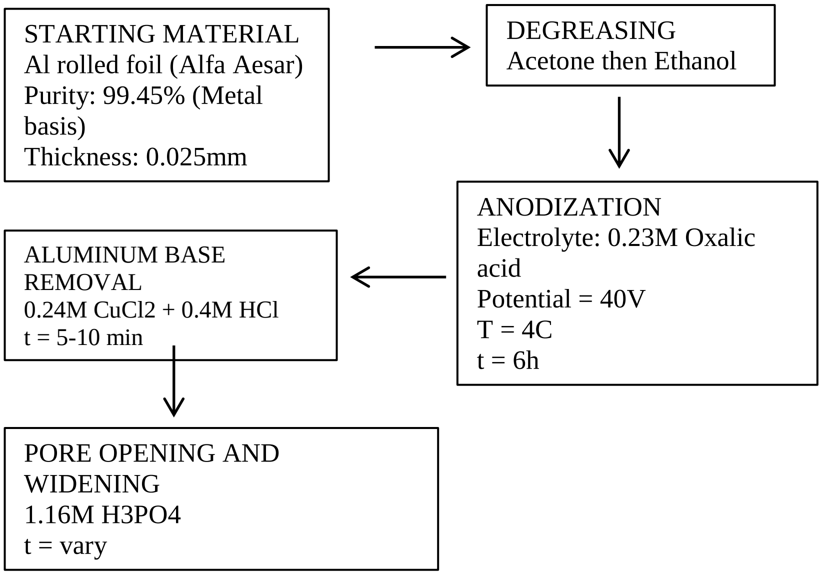

Figure 3.2 Diagram of anodization process

After anodization porous aluminum oxide structures were obtained. However, the structures were not ready to be used unless the through-hole structures had achieved. Therefore, the bottom Al base needs to be removed as shown in Figure 3.3.

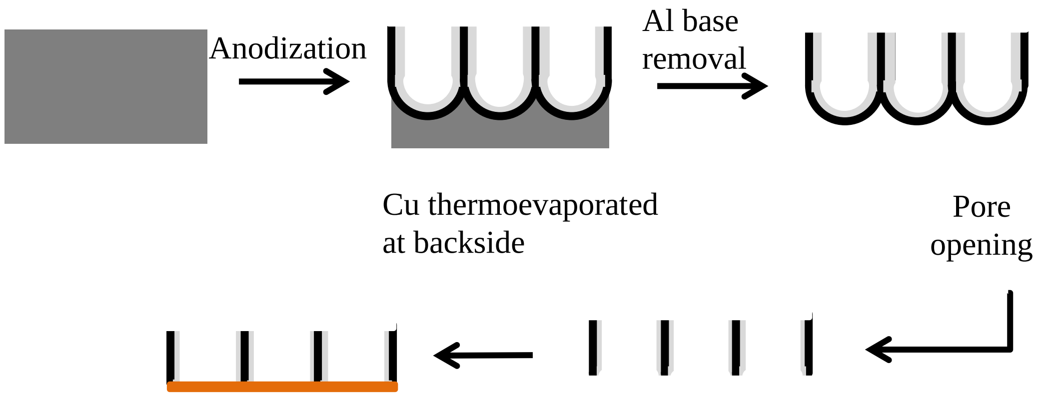

Figure 3.3 Schematic diagram of AAO membrane template fabrication process

To remove the bottom base layer of Al, the mixture of 0.24M of $CuCl_2$ and 0.4M of HCl were used There were two reactions occur:

$$2Al(s)+6HCl(aq)\rightarrow 2AlCl_3(aq)+3H_2(g) \qquad (3.1)$$

$$2Al(s)+3CuCl_2(aq)\rightarrow 3Cu(s) \qquad (3.2)$$

Next, 1.16M of phosphoric acid was used in pore opening and pore widening process. The barrier layer was dissolved. Pore diameters can be adjusted by different pore opening times.

The reaction during pore opening is as follows,

$$Al_2O_3(s)+3H_3PO_4(aq)\rightarrow 2AlPO_4+3H_2O(l) \qquad (3.3)$$

3.3 Results and Discussions

3.3.1 Current Density

During the anodization process, current and anodizing time was monitored as shown in Figure 3.4. There are three distinguished region in the current density curve over the entire anodizing time. In the first region, insulated aluminum oxide layer was developed in early stage as shown with an abruptly dropped current in first 10 seconds with current changing from about 200mA to 1mA. Then in the second region, current gradually increased indicating a random formation of pits on the oxide layer. Pits grew and became pores close to 5 minutes after anodization had begun. Further anodization, a constant current density had been reached indicating the straight pores had been formed with as the growth of oxide front in oxide/Al interface and dissolution of oxide layer in oxide/electrolyte interface were balanced. In our setup, the current density was approximately 17 A/m^2 which was considered as mild anodization.

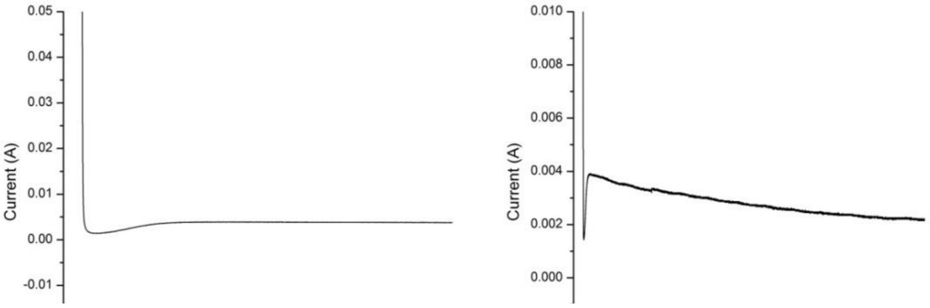

Figure 3.4 Anodizing current as a function of time (a) over 20 min, and (b) over 6 hrs

3.3.2 Rate of Pore Opening and Widening

After the removal of the Al base, the through pores can be obtained by etching the barrier layer in 1.16M phosphoric acid (H_3PO_4). In this process, pores will also be widened to desired pore diameter according to different immersing times. The top side of AAO membranes before and after opening at different times was observed in SEM as shown in Figure 3.5.

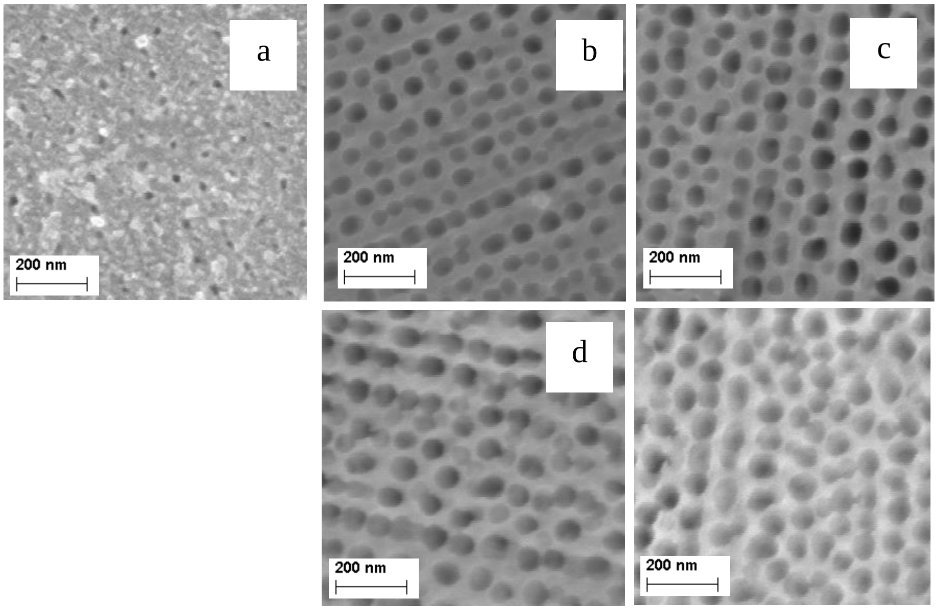

Figure 3.5 SEM images of top side of AAO membrane at pore opening time (a) 0 min, (b) 60min, (c) 70min, (d) 80 min, and (e) 90 min

Pores forming on the top side were randomly arranged and some of them were merged together. The surface roughness, defects and impurity on the surface of Al foil have effects on pore formation in the early stage. Figure 3.6 shows SEM images of the bottom side of AAO membranes with pore widening time of 0, 60, 70, 80, and 90 minutes.

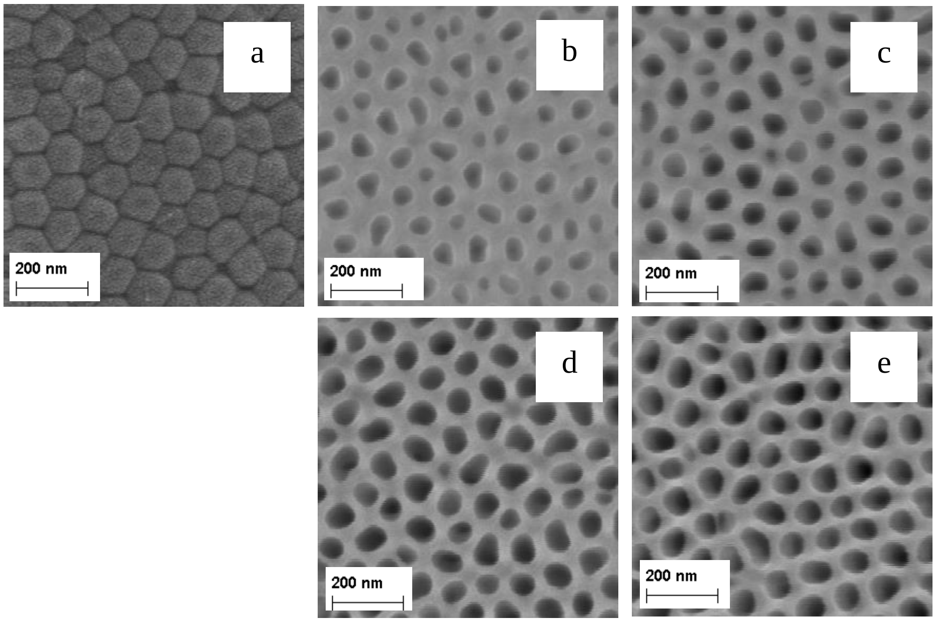

Figure 3.6 SEM images of bottom side of AAO membrane at pore opening time (a) 0 min, (b) 60min, (c) 70min, (d) 80 min, and (e) 90 min.

SEM image (a) shows the arrays of hemispheres arranged in hexagonal-close packed pattern with an average cell size of 115 nm. Theoretically, cell size of AAO membrane anodized in oxalic acid at anodizing potential over 20V can be calculated as follows:

$$D_C = -1.70 + 2.81xV \qquad (3.4)$$

So that at anodizing potential of 40V the calculated cell size is 110.7 nm which is close to our obtained cell size.

The pore opening was carried out at different immersing time in order to obtain the etching rate. Figure 3.7 shows rate of pore opening and widening as an average pore diameter at different pore opening time. The average pore diameter was measured according to SEM micrographs. From 0 to 60 minutes, the etching rate on the bottom side is approximately 1.2nm/min while in the top side the rate is slower at approximately 0.45nm/min.

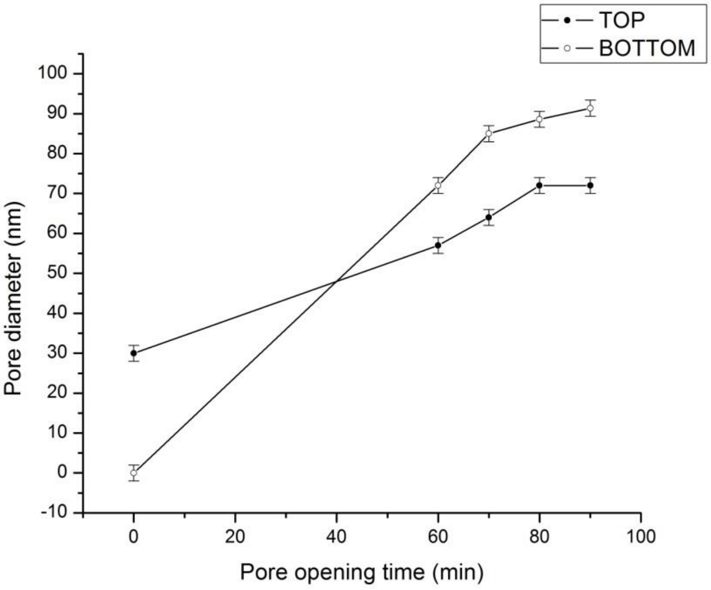

Figure 3.7 Pore diameter of top and bottom part of AAO membranes at different pore widening time.

This indicates that the materials built up at the barrier layer are more susceptible to the chemical reaction with phosphoric acid (H_3PO_4) than the materials in the inner pore wall. Barrier layer is a growth front of oxide layer which constantly build up in oxide/metal interface while dissolution is happening in oxide/electrolyte interface. Considering the ion species in this process as shown in Figure 3.8, regardless of oxide formation and dissolution, H_2O and oxalate anion ($C_2O_4{}^{-2}$) migrated into the oxide layer due to the electric field between cathode and anode to form $Al_2(C_2O_4)_3$ which has lower density than pure Al_2O_3.

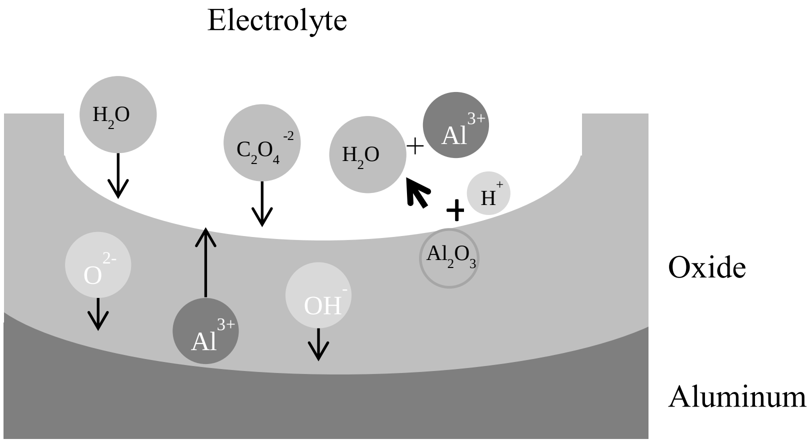

Figure 3.8 Schematic diagram showing ions movement and dissolution of oxide in oxalic acid

According to the growth model proposed by Patermarakis and colleagues [42], the oxalate anions have maximum concentration at the center of barrier layer and gradually decrease to cell wall. Therefore, the bottom side which has anion incorporated has faster etching rate than that of the top side. In addition, the plotting shows that the barrier layer will be etched completely after 70 minutes, and after that the etching rate decreases to 0.32nm/min which indicates that it reaches anion-free oxide layer.

Figure 3.9 shows cross-sectional SEM images of 10 um thick AAO membranes before and after pore opening for 80 minutes.

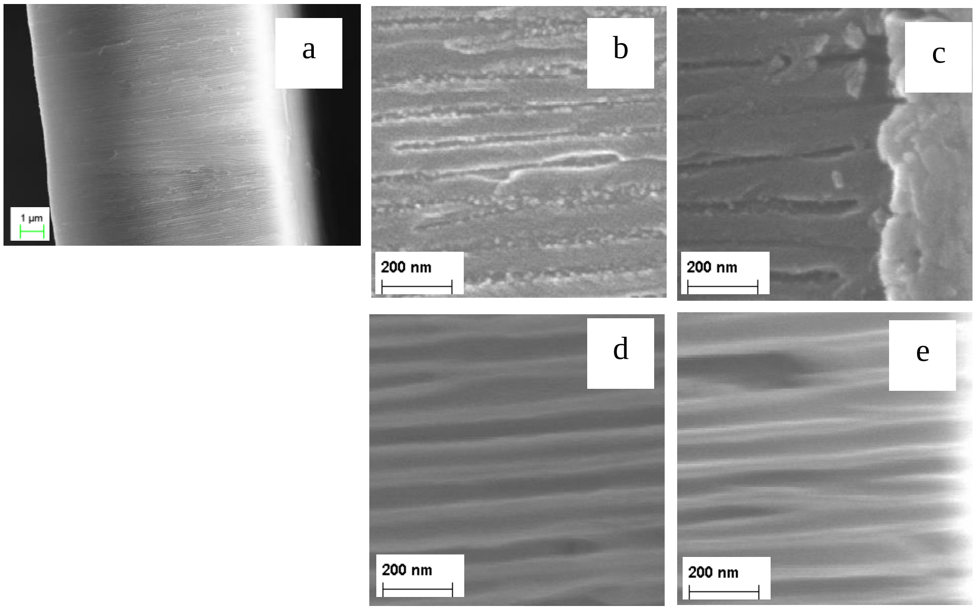

Figure 3.9 SEM images of (a) cross-section view of AAO membrane, (b) middle part of membrane, (c) bottom part before pore opening and (d) middle part of membrane, (e) bottom part of membrane after pore opening

Before pore opening, there were U shape structures at the bottom of membrane(c), and then became through-hole structure as shown in image (e) after 80 minutes of pore opening. In addition, the channels were enlarged and became more parallel as shown in image (d) comparing to image (b).

It should be noted that AAO membranes will be completely dissolved after 100 minutes of pore opening. It can be concluded that the etching rate is relatively linear with time in first 70 minutes and the pore size can be controlled by varying the pore opening time.

3.3.3 Porosity of AAO Membranes (α)

Porosity of AAO membrane, defined as a ratio of a surface area containing pores to the whole surface area of membrane, depends on the rates of oxide growth, chemical dissolution of oxide in acidic electrolyte, anodizing potential, pH, and concentration of electrolyte.

The porosity can be calculated considering a single circular hole inside the hexagon cell.

$$\alpha = 0.907\left(\frac{D_P}{D_C}\right)^2 \tag{3.5}$$

D_P is pore diameter, and D_C is cell size or inter-pore distance.

According to Table 3.1 porosity of AAO membrane before pore opening is approximately 6%. The porosity of AAO membrane at different pore opening time was calculated from bottom side of the AAO membrane.

Table 3.1 Porosity of AAO membranes at different pore widening time

Pore widening time (min)	Pore diameter, top (nm)	Pore diameter, bottom (nm)	Porosity ($\alpha = 0.907(\frac{D_P}{D_C})^2$)
0	30	0	0.06*
60	57	72	0.36
70	64	85	0.50
80	72	88.6	0.54
90	72	91.4	0.57

* calculated from top side of membrane

At 90 min the porosity is too high and consequently the membrane is very fragile and difficult to handle. Therefore in our experiment the optimum pore opening time is in the range of 70-80 min.

3.4 Summary

In summary, based on the understanding of the anodization proceess, we have optimized the processing parameters, including electrolyte, potential, time and pore opening and widening time, and successfully fabricated the AAO membranes that can be used as the templates for fabrication of multilayered nanorods. The pore diameter of AAO membrane is below 100 nm, which meets the designed nanorod diameter and can be varied from 40 nm to 100 nm by changing the pore opening and widening time after the anodization process.

Chapter 4

Fabrication of Multilayered Nanorods

To make multilayered magnetic nanoparticles, template-based synthesis by pulse electrodeposition into AAO templates was employed throughout this research. This method is simple, low cost, and can be used for mass production. AAO membrane with pore diameter about 80nm and thickness of 10-12um was first coated with 350 nm Cu layer to cover one end of membrane using thermal evaporation. The Cu layer also acts as working electrode for electrodeposition. Long Cu rods about 5 um long were first electrodeposited as a sacrificial layer and SEM micrograph shows a uniformity of Cu rods inside AAO channels which confirms the quality of homemade AAO membrane as shown in Figure 4.1.

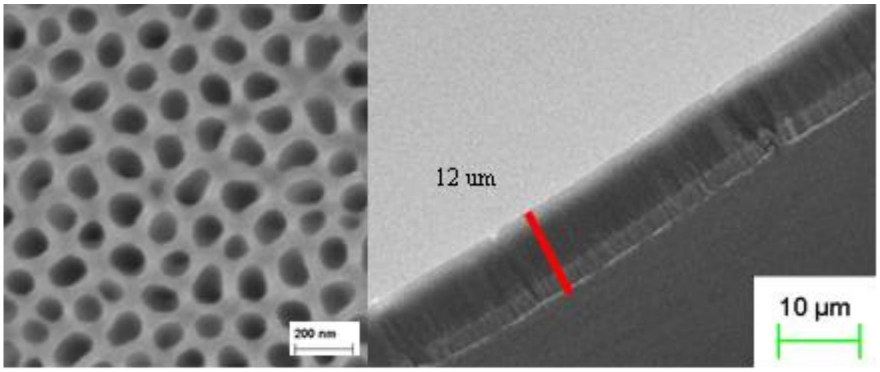

Figure 4.1 Top view SEM image of AAO membrane with pore diameter about 80nm (a), and cross-sectional view SEM image of Cu rods inside AAO template (b).

Consequently, the magnetic material was electrodeposited by pulse electrodeposition inside the channels. The deposited magnetic nanoparticles were released into water suspension by dissolution of AAO template in 2M NaOH. The general procedure of fabrication process is illustrated in Figure 4.2.

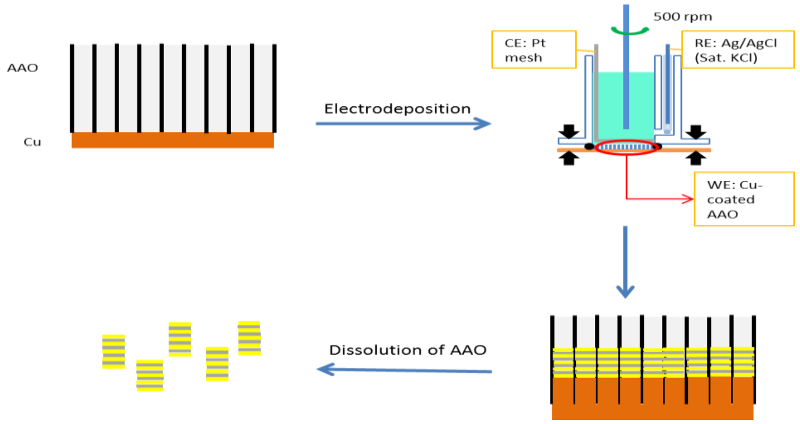

Figure 4.2 Schematic of the general fabrication process of magnetic nanoparticles

In this chapter, the fabrication of (1) Au/NiFe, (2) Au/Fe, (3) Au/Co multilayered nanoparticles will be discussed.

4.1 Layer by Layer Electrodeposition of Au/NiFe Nanorods

Au and NiFe were separately electrodeposited layer by layer into AAO template by changing electrolyte solution. First, cyclic voltammetry (CV) was performed to determine the proper applied potential for the deposition of each metal layer inside AAO channels. CV was carried out from -0.1V to -1.3V with scan rate of 5mV/s. Commercial Au electrolyte solution (Technic 434 HS RTU (0.066Tr.Oz/lit.)) was used, and the reduction peak in the CV curve was at -0.55V, as shown in Figure 4.3(a).

In order to figure out the optimum applied potential for NiFe electrodeposition, NiFe, Ni, and Fe electrolyte were prepared. The reduction peaks in the CV curve for NiFe was at -0.7V, for Ni reduction at -0.93V, and for Fe at -0.9V. CV curve for NiFe is shown in Figure 4.3(b).

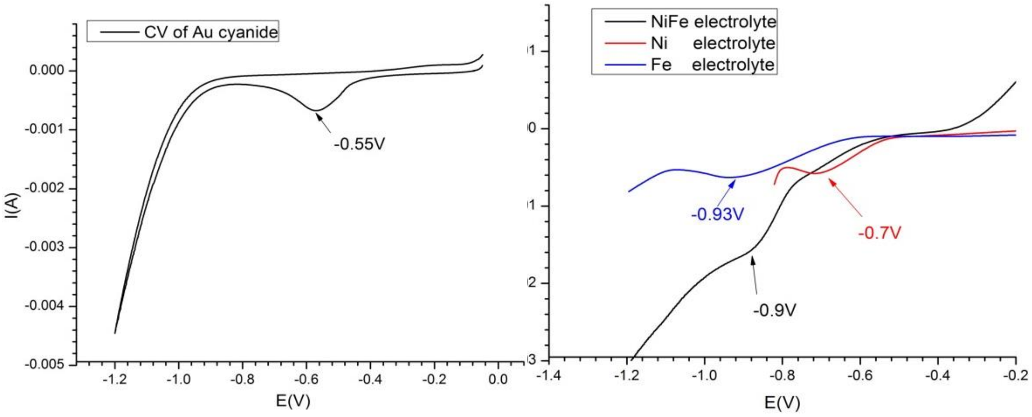

Figure 4.3 Cyclic voltammetry of Au 434HS RTU (a), NiFe electrolyte (b)

The applied potential for Au was chosen at -0.5V (VS. Ag/AgCl (sat.KCl)) while for NiFe was varied from -0.7, -0.75,-0.8, -0.85, -0.9, -0.95, -1.0, and-1.1V (VS. Ag/AgCl (sat.KCl)).

4.1.1 Optimum Applied Potential for Fabrication of Au/NiFe Nanorods

Since there are two ions species in NiFe electrolyte solution which were reduced at different potentials so that the experiment was conducted to find the optimum applied potential to achieve NiFe co-deposition. The applied potentials were varied from -0.7 to -1.1V ((VS. Ag/AgCl (sat.KCl)) after the long Cu rods were deposited (-0.001V (VS. Ag/AgCl (sat.KCl)) as sacrificial layer. The SEM micrographs and the magnetic signals from VSM confirmed the electrodeposition of NiFe that can be deposited from -0.8V to -1.1V as shown in Figure 4.4.

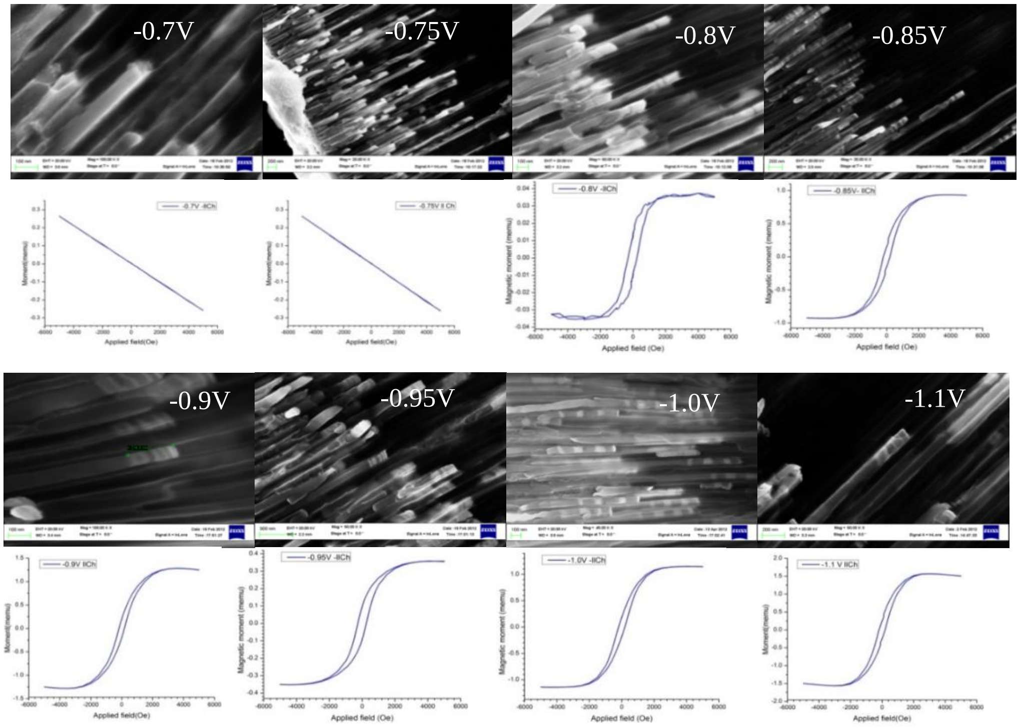

Figure 4.4 SEM micrographs and magnetic signals of Au/NiFe which NiFe was electrodeposited at different potential from -0.7V to -1.1V

4.1.2 Crystal Structure of Au/NiFe Nanorods

Sample of NiFe with long Cu inside AAO was measured in an X-ray diffractometer and XRD pattern shows that electrodeposited NiFe has FCC structure with the peaks at 2theta of NiFe (111), NiFe (200), and NiFe (220).

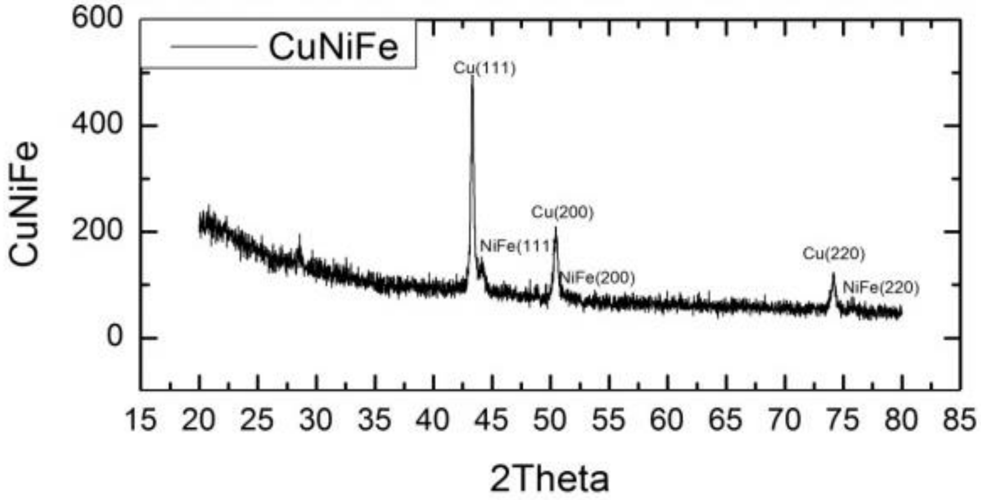

Figure 4.5 XRD patterns of Cu/NiFe in AAO template

In summary, Au/NiFe nanorods can be electrodeposited at -0.5 V for Au and from -0.8 V to -1.1 V for NiFe. The electrodeposited NiFe has FCC structure. The magnetic properties of Au/NiFe samples were studied on and will be discussed in the next chapter.

Table 4.1 Electrolyte compositions and conditions for Au/NiFe electrodeposition

Electrolyte	Compositions	Electrodeposition conditions
Cu	$CuSO_4.5H_2O$ 0.5M H_2SO_4 0.5 ml DI water 100ml	-0.001V VS. Ag/AgCl (Sat.KCl), 5C
Au	Technic 434 HS RTU 0.066 Tr.Oz/l	-0.5V
NiFe	$NiSO_4.6H_2O$ 0.05M $FeSO_4.7H_2O$ 0.009M H_3BO_3 0.04M Saccharine 0.016M DI water 100ml pH 3.0 adjusted by sat.KOH	-0.7V - -1.1 V VS. Ag/AgCl (Sat.KCl)

4.2 Fabrication of Au/Fe and Au/Co Multilayered Nanorods with One-Bath Electrodeposition.

4.2.1 Electrodeposition of Au/Fe Multilayered Nanorods

Au/Fe multilayered nanodisks were fabricated by pulse electrodeposition into AAO template using the electrolyte solution contained both Au^+ and Fe^{2+} ions; the concentration of Fe^{2+} (0.026M $FeSO_4 .7H_2 O$) is much higher than the concentration of Au^+ (0.3mM $KAu(CN)_2$) to avoid the co-deposition of Au in Fe. Cyclic voltammetry (CV) of the electrolyte solution was performed on Au coated Si wafer to figure out the optimum pulse potentials for electrodeposition. CV was carried out from -0.1V to -1.3V with scan rate of 5mV/s. As shown in Figure 4.6, there were two peaks existed at -0.58V and -1.1V, corresponding to the reduction of Au^+ ions and Fe^{2+} ions. The applied potentials were chosen as -0.45V for Au deposition and -1.2V for Fe deposition.

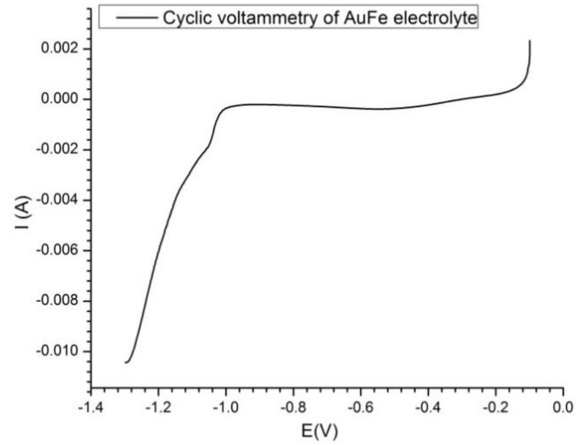

Figure 4.6 Cyclic voltammetry of single bath Au/Fe electrolyte solution.

During electrodeposition, the effect of stirring electrolyte was studied. SEM micrographs reveal the alternating layers of Au (bright) and Fe (dark) with uniform segmental thickness of each metal (Figure 4.7(a)). If the electrolyte was not agitated during electrodeposition non-uniform structures will be produced (Figure 4.7(b)).

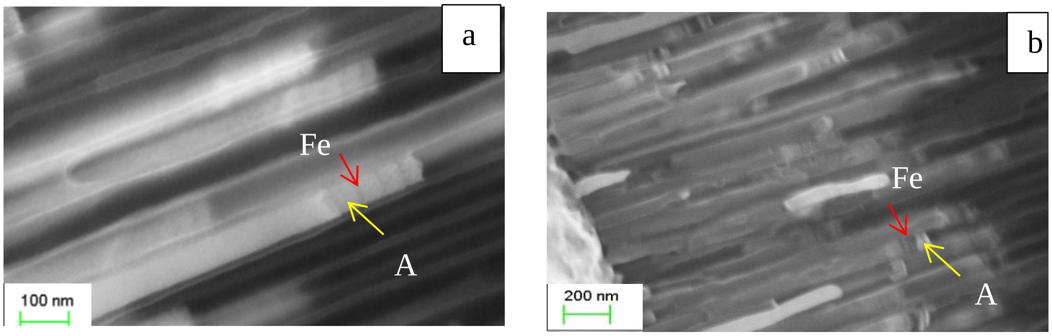

Figure 4.7 SEM micrographs of Au/Fe multilayered nanodisks (a) with stirring, (b) without stirring.

In summary, Au/Fe multilayered nanorods can be electrodeposited at -0.45 V for Au and -1.2V for Fe, and the thickness of each layer can be controlled by the deposition time. The magnetic properties of Au/Fe multilayered nanorods samples were studied on and will be discussed in next chapter.

Table 4.2 Electrolyte compositions and conditions for Au/Fe electrodeposition

Electrolyte	Compositions	Electrodeposition conditions
Cu	$CuSO_4.5H_2O$ 0.5M H_2SO_4 0.5 ml DI water 100ml	-0.001V VS. Ag/AgCl (Sat.KCl), 5C
AuFe	$KAu(CN)_2$ 0.3mM $FeSO_4.7H_2O$ 0.026M $C_6H_8O_7$ 0.049M Di water 100ml pH 6.15 adjusted by sat.KOH	Au -0.45V Fe -1.2 V VS. Ag/AgCl (Sat.KCl),

4.2.2 Electrodeposition of Au/Co Multilayered Nanorods

Au/Co multilayered nanoparticles were also fabricated by pulse electrodeposition into AAO template. The electrolyte solution containing both Au ions and Co ions was used, allowing Au and Co to be deposited inside the channel without changing the solution. To avoid co-deposition of both metals while depositing Co, a huge difference in ion concentration is required. In this experiment, the ion concentration is 0.285M and 0.3mM for Co and Au, respectively. CV was performed in (1) electrolyte containing Au ions only, (2) electrolyte containing Co only, and (3) electrolyte containing both Au ions and Co ions. There were peaks as -0.5V for Au reduction, -0.83V for Co reduction. Experimentally, it was found that at -0.8V there was no electrodeposition of Co in AAO, so that the experiments were designed to find the optimum applied potential for Co deposition at higher potential, -1.0V, -1.1V, and -1.2V. The thickness of Au and Co layers can be tuned by the deposition time.

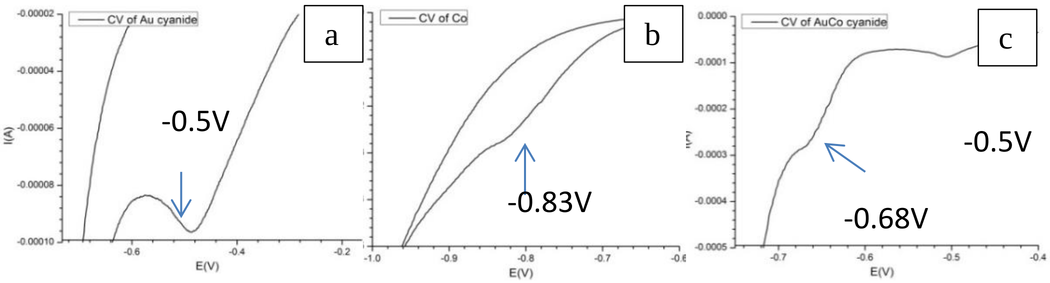

Figure 4.8 Cyclic voltammetry of Au electrolyte (a), Co electrolyte (b), and AuCo electrolyte (c).

As shown in Figure 4.9, the thickness of Au and Co layers can be controlled by pulse duration to obtain different structures from long segment of Co, bamboo-like structure in Figure 4.9(a), to a disk-like multilayered nanorod in Figure 4.9(b). Eventually, if the pulse duration of Co deposition is limited to 20 s the Co islands embed in Au matrix will be achieved as shown in Figure 4.9(c). Different structures would exhibit different magnetic properties which will be discussed later in next chapter.

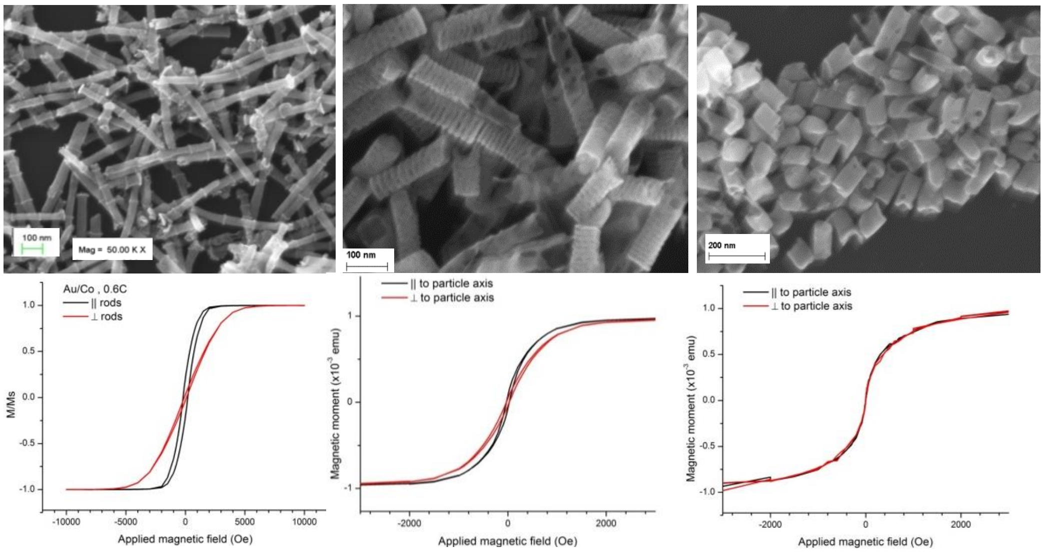

Figure 4.9 SEM images of (a) Au 10nm/Co 200nm, (b) Au 10nm/Co 10nm, (c) Co island embed in Au matrix, and VSM signals of (d) structure in (a), (e) structure in (b), and (f) structure in (c) respectively

Table 4.3 Electrolyte compositions and conditions for Au/Co electrodeposition

Electrolyte	Compositions	Electrodeposition conditions
AuCo	$KAu(CN)_2$ 0.3mM $CoSO_4.7H_2O$ 0.0285M $C_6H_8O_7$ 0.8M Di water 100ml pH 3.50 adjusted by sat.KOH	Au -0.45V, -0.5V, -0.7V Co -1.0V to -1.2 V VS. Ag/AgCl (Sat.KCl),

4.3 Summary

In summary, using templated electrodeposition into AAO membrane three types of magnetic-plasmonic multilayered nanorods have been fabricated; Au/NiFe, Au/Fe and Au/Co multilayered nanorods. The electrodeposition conditions for each material were systematically studied using cyclic voltametry, and optimum potentials were obtained. The thickness of each layer can be well controlled by deposition time.

Chapter 5

Magnetic Properties of Multilayered Nanorods

In this chapter we studied on the effect of the aspect ratio of nanorods on their magnetic properties. Shape anisotropy plays a key role in manipulating magnetic properties of nanorods from single domain to superparamagnetics. Vibrating sample magnetometer (VSM) was employed in magnetic characterization.

Magnetic properties of produced magnetic nanorods are characterized using VSM. In VSM, a uniform magnetic field generated from electromagnet is applied across an oscillating sample near a set of pick up coils. The flux of uniform field is distorted and induces a potential drop, as followed Faraday's law of induction, across pick up coils. The potential V is proportional to the magnetic moment from the sample so that the hysteresis loop (m-H curve) can be obtained by varying applied field while measuring the magnetic moment of the sample.

Faraday's law of induction is

$$V = -N \tfrac{d\phi}{dt} \tag{5.1}$$

where N is number of turns in pick-up coils and ϕ is the flux in the coils.

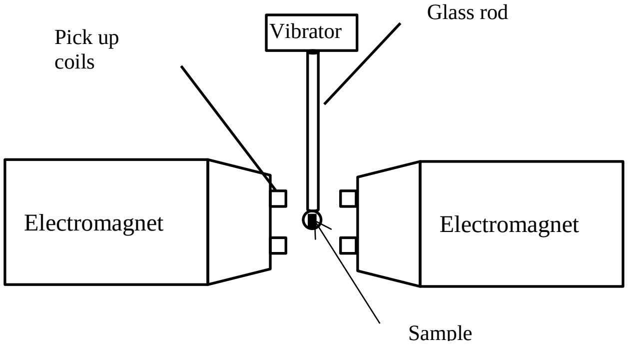

Figure 5.1 Schematic drawing of VSM measurement

Hysteresis loops were measured in two directions of applied fields, 1) parallel field and 2) perpendicular field, defined as the direction of applied field respectively to nanorod axis. Saturation moment (M_s), remanence moment (M_r), coercivity field (H_c), and saturation fields (H_s) of different sizes of magnetic nanorods were observed. Magnetic properties are determined by the thickness and number of the magnetic layers, which can be easily explained according to anisotropy energy.

5.1 Magnetocrystalline Anisotropy (E_{ca})

In single crystal magnetic materials, magnetization is preferred to align in certain crystal orientations called easy axis of magnetization. In cubic system, magnetocrystalline anisotropy energy can be expressed as:

$$E_{ca} = K_1(\alpha_1^2\alpha_2^2 + \alpha_2^2\alpha_3^2 + \alpha_3^2\alpha_1^2) + K_2(\alpha_1^2\alpha_2^2\alpha_3^2) \qquad (5.2)$$

where K_1 and K_2 are anisotropy constant, and α_1, α_2, and α_3 are the projections of unit vector on three crystalline easy axes. And the uniaxial anisotropy energy is given by:

$$E_{ca} = K_{u1} \sin^2 \theta + K_{u2} \sin^4 \theta \tag{5.3}$$

where K_{u1} and K_{u2} are anisotropy energy constants, and θ is angle between magnetization direction and easy axis orientation.

HCP Cobalt has a uniaxial crystalline anisotropy with easy axis in [0001] direction while FCC Ni and BCC Fe have a cubic crystalline anisotropy with easy axis in [111] direction for Ni and [100] direction for Fe as shown in Table 5.1.

Table 5.1 Values of magnetocrystalline anisotropy energy constant K1[15]

Material	Crystal structure	Easy axis	K_1 (erg/cm^3)
Ni	FCC	[111]	-4.5×10^4
Fe	BCC	[100]	4.8×10^5
$Ni_{78}Fe_{20}$	FCC	-	0
Co	HCP	[0001]	4.5×10^6

We have confirmed the crystal structure of NiFe in Au/NiFe magnetic nanorods and Co in Au/Co magnetic nanorods. Figure 5.2(a) shows X-ray diffraction pattern of NiFe with Cu rods, and it reveals a FCC polycrystalline structure of NiFe alloy with Ni:Fe ratio at 80:20, which is called permally. Permalloy itself is considered as magnetic material with no crystalline anisotropy In case of Au/Co nanorods, TEM micrograph shows Co has a HCP structure (a=0.25nm as inset in Figure 5.2(b)) with a grain size about 7nm

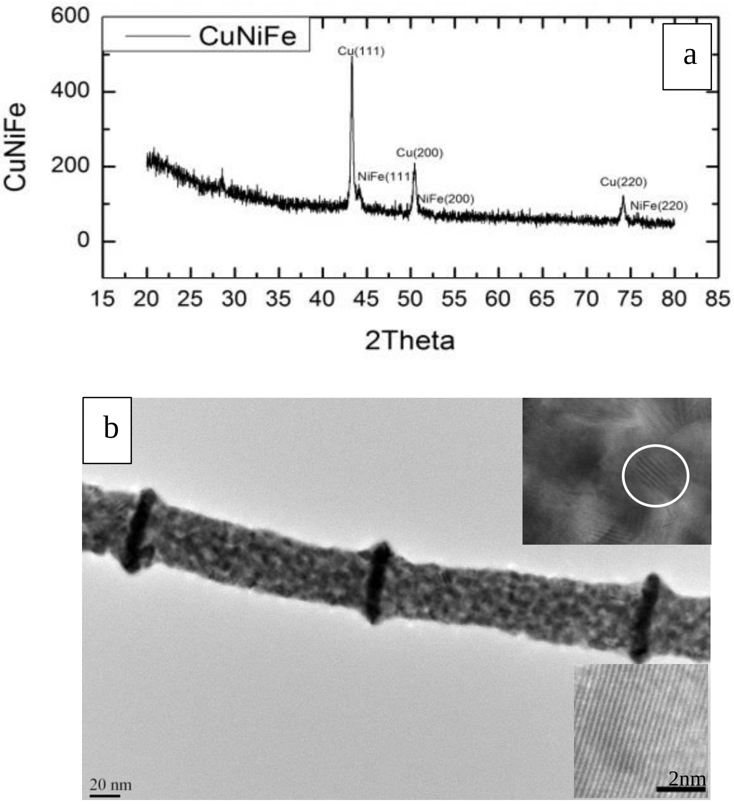

Figure 5.2 XRD patterns of Cu/NiFe nanorods (a) and (b) TEM micrograph of Au/Co nanorods.

The sample is polycrystalline without texture, so the easy axis of grains oriented randomly. The magnetocrystalline anisotropies from all grains cancel out, and do not contribute to the overall anisotropy of the rod. Non-spherical polycrystalline magnetic particles anisotropy energy will be influenced from shape anisotropy. The magnetization will be easier in long axis rather than in short axis of particle. Only shape anisotropy need to be considered for our samples.

5.2. Shape Anisotropy

Shape anisotropy depends on shape of specimen. Spherical specimen with no crystalline anisotropy will have the same magnetization in any direction after it is magnetized by applied field. For non-spherical specimen with no crystalline anisotropy, magnetization direction point to the elongated axis of specimen. This phenomenon is called shape anisotropy.

5.2.1 Shape Anisotropy in Nanorods

Au/NiFe nanorods were prepared in three aspect ratio, A.R.=1, 3.5, and 10. Figure 5.3 shows the hysteresis loops with SEM micrographs of the samples.

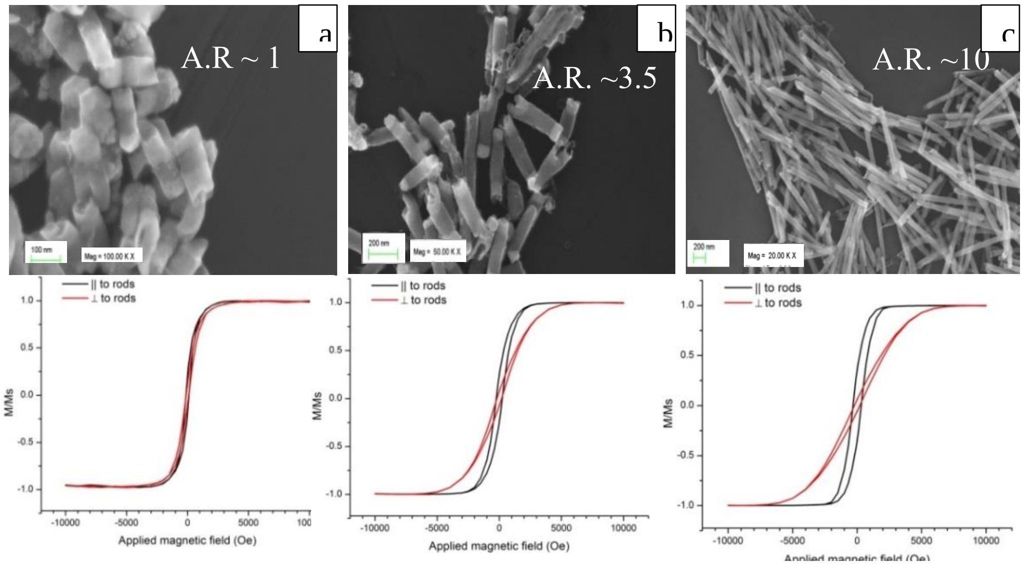

Figure 5.3 Hysteresis loops of Au/NiFe nanorods with aspect ratio a) 1, b) 3.5 and c) 10

Table 5.2 Magnetic measurement by VSM of Au/NiFe with three different lengths in parallel and perpendicular direction

Aspect ratio	Parallel field				Perpendicular field			
	Ms (memu)	Mr (memu)	Hc (Oe)	Hs (Oe)	Ms (memu)	Mr (memu)	Hc (Oe)	Hs (Oe)
1	0.15	0.03	100	3000	0.18	0.02	100	3000
3.5	1.8	0.044	200	4000	1.9	0.14	150	6000
10	3.4	1.2	300	3000	3.4	0.2	200	7000

From VSM measurement, the saturation moment (Ms) increases as the length of NiFe increases. The remanence is close to zero for sample with aspect ratio 1 and 3.5 while aspect ratio sample has higher remanence. The coercivity of sample with aspect ratio of 1 is the same in both direction as well as the saturation fields. This is the indication of zero anisotropy, i.e. the magnetization process is the same for both directions. However, in samples with aspect ratio 3.5 and 10 the coercivity in parallel direction is higher than that of in perpendicular direction which means it needs higher reverse field to reduce the magnetic moment to zero. The saturation field (Hs) in parallel direction is lower than in perpendicular direction. These are the indications of the shape anisotropy.

The anisotropy energy can be estimated from the area between hysteresis loops from easy and hard axis in 1st quadrant, which indicates the energy store in hard axis during magnetization. Here we estimate the anisotropy energy of samples with aspect ratio of 3.5 and 10 by integrating area under the curves. It can be seen that the anisotropy energy for rods with A.R 10 is twice as the anisotropy energy for rods with A.R 3.5.

A nanorod with A.R. larger than 10 can be approximated as prolate spheroid, whose anisotropy energy can be calculated. We know that the magnetostatic energy of a prolate spheroid is:

$$E_D = \frac{1}{2} N_d M_s^2 \quad (\text{erg/cm}^3) \qquad (5.4)$$

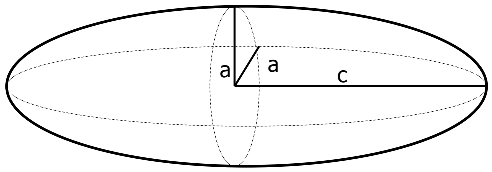

Prolate spheroid

Figure 5.4 Schematic drawing of a prolate spheroid

The demagnetizing factor N_d in short axis (N_a) and long (N_c) are written below.

$$N_a = N_b = 4\pi \frac{m}{2(m^2-1)} \times [m - \frac{1}{2(m^2-1)^{1/2}} \times \ln(\frac{m+(m^2-1)^{1/2}}{m-(m^2-1)^{1/2}})] \qquad (5.5)$$

$$N_C = 4\pi \frac{1}{m^2-1} \times [\frac{m}{2(m^2-1)^{1/2}} \times \ln(\frac{m+(m^2-1)^{1/2}}{m-(m^2-1)^{1/2}}) - 1] \qquad (5.6)$$

The shape anisotropy energy is the magnetostatic energy difference when magnetization points in two axes. At aspect ratio m is larger than 10, $N_a \approx 2\pi$ and $N_c \approx 0$ therefore the shape anisotropy energy is:

$$\Delta E_D = E_{Da} - E_{Dc} = \pi M_s^2 \qquad (5.7)$$

For $Ni_{78}Fe_{22}$, M_s is 800 emu/cm^3 the shape anisotropy energy is estimated as 2x10^6 erg/cm^3.

The shape anisotropy for Au/Co nanorods with difference aspect ratios was also studied. Samples with A.R of 1.25, 2.5 and 3.75 were prepared and hysteresis loops with external field parallel and perpendicular to the long axis of the rods were measured, which are shown below.

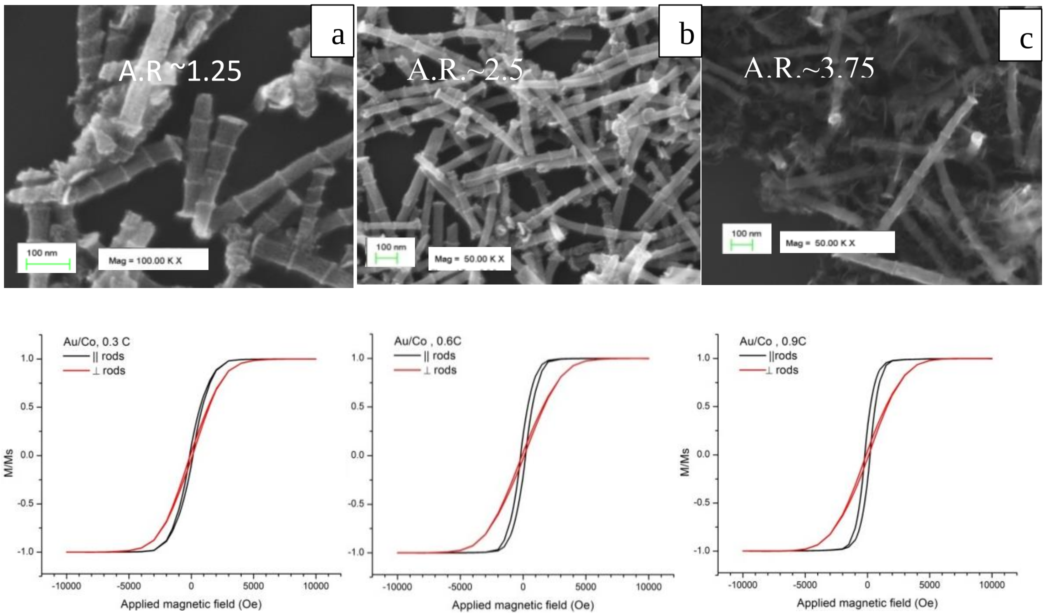

Figure 5.5 Hysteresis loops of Au/Co nanorods with aspect ratio a) 1.25, b) 2.5 and c) 3.75.

Table 5.3 Magnetic measurement by VSM of Au/Co with three different lengths in parallel and perpendicular direction

Aspect ratio	Parallel field				Perpendicular field			
	Ms (memu)	Mr (memu)	Hc (Oe)	Hs (Oe)	Ms (memu)	Mr (memu)	Hc (Oe)	Hs (Oe)
1.25	2.05	0.57	200	4000	2.01	0.08	100	6000
2.5	4.17	0.87	200	3000	3.74	0.12	80	6000
3.75	6.96	0.69	200	3000	6.48	0.23	80	6000

It can be seen that the saturation fields for parallel direction are lower than that for perpendicular direction in all cases, an indicator of shape anisotropy.

The nanorods were closely packed inside AAO membrane, so the magnetostatic interaction between rods also needed to be taken into account. Two neighboring magnetic nanorods have two possible configurations, parallel and antiparallel to each other. The parallel alignment is not energetically favored since the same poles will repel one another, whereas antiparallel configuration allows flux closure and therefore is energetically favorable. If distance between nanorods is *x* and each rod has poles at each end with pole strength *p* separated by a length *l* then the interaction field is

$$H_{\text{int}} = \frac{pl}{[x^2 + \frac{l^2}{4}]^{3/2}} \tag{5.8}$$

If *x* is much large comparing to length *l* then interaction field can be simplified as:

$$H_{\text{int}} = \frac{pl}{x^3} \tag{5.9}$$

In densely packed nanorods, this interaction field can significantly reduce the measured coercivity compared to the isolated nanorods. The shape anisotropy is suppressed in closely packed nanorods. The measured anisotropy is lower than actual anisotropy of individual rods.

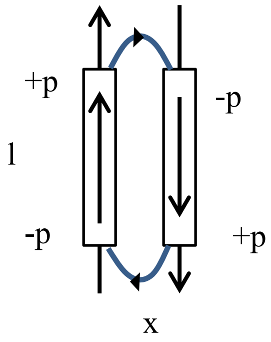

Figure 5.6 Schematic drawing of magnetization and interaction fields in two nanorods.

5.2.2 Shape Anisotropy in Au/Co Multilayered Nanorods

Au/Co multilayered nanorods were fabricated by pulse electrodeposition into AAO template. The alternating layers of Au and Co were achieved by deposition of Au at -0.5V (VS.Ag/AgCl (Sat.KCl) with 200s pulse duration for 11 layers and deposition of Co at -1.1V with 30s pulse duration for 10 layers. SEM micrograph of rods with alternating layers of Au (bright) and Co (dark) is shown in Figure 5.7.

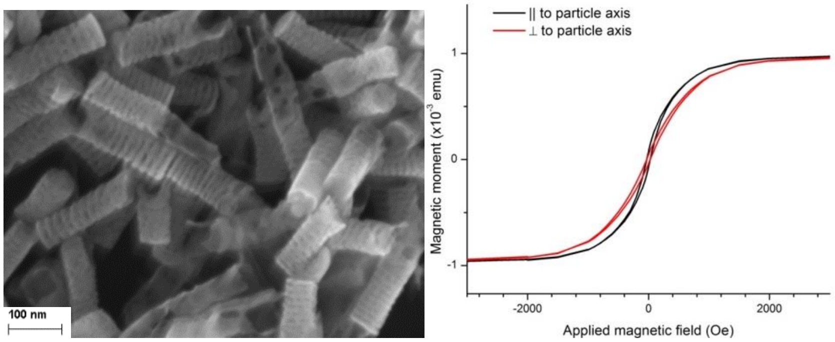

Figure 5.7 SEM micrograph of Au/Co multilayered nanorods (a), and hysteresis loop (b).

Table 5.4 Magnetic measurement by VSM of Au/Co multilayered nanorods

Field direction	Ms (memu)	Mr (memu)	Hc (Oe)	Hs (Oe)	Mr/Ms
Parallel field	0.38	0.027	20	3000	0.07
Perpendicular field	0.44	0.016	20	7000	0.04

For single disk, magnetization prefers to align along disk plane. However, when two disks are put together with an Au separation layer, these two disks are coupled with interaction magnetic field. There exists a competition between shape anisotropy and interaction field between two disks. For individual nanodisk, the easy axis aligns in disk plane. However, from VSM measurement for multilayered nanorods, the hysteresis loops in parallel and perpendicular direction are comparable; no obvious anisotropy is observed. This strongly suggests the strong interaction between neighboring Co layers greatly suppresses the anisotropy.

5.3 Superparamagnetic Nanoparticles

Superparamagnetic nanoparticles occur only in a few nanometers at room temperature such as 7nm in Co and 6nm in Fe. These particles exhibit high magnetic moment at small applied field and retain no magnetic once applied field removed.

When the Co layer thickness is reduced further, it cannot form a continuous film, and instead Co islands are formed which are covered by the subsequent Au deposition. Figure 5.8 shows the SEM micrograph and corresponding hysteresis loops of the samples made with alternating electrodeposition of Co and Au for 10 cycles with pulse duration of Au electrodeposition was kept constant at 200s while varying deposition time of Co from 10s, 15s, and 20s.

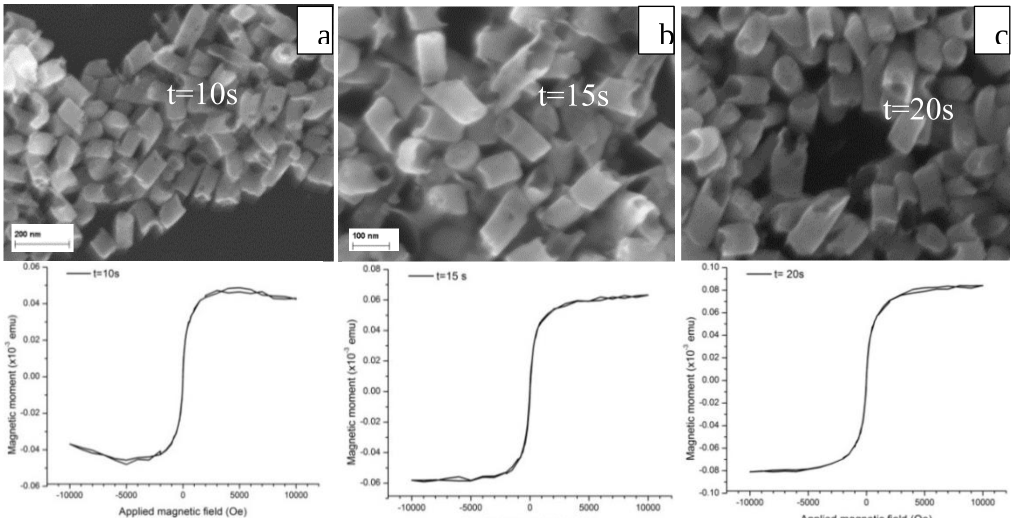

Figure 5.8 Hysteresis loops of Au/Co-Co islands at different deposition times (a) 10s, (b) 15s, and (c) 20s.

SEM images cannot reveal Co layer, but the VSM measurements clearly show magnetic response M-H curves. This indicates that Co is embedded inside Au. Also, they all clearly show superparamagnetic behavior. From Figure 5.2, we know the grain size of deposited Co is about 7 nm. The electrodeposition process is a nucleation and growth process. When the deposition time is very short, the Co is in the nucleation or early growth stage. The size of Co island is definitely smaller than 7 nm. The superparamagnetic limit for Co is about 7nm, so deposited Co islands are superparamagnetic nanoparticles. The rod becomes an aggregate of many isolated superparamagnetic nanoparticles which results in the superparamagnetic behavior of the rods shown in the hysteresis loops.

In addition, we found that such superparamagnetism can be achieved in Au/Fe magnetic nanorods as well if the Fe layer is thinner than 10nm. (see Figure 5.9).

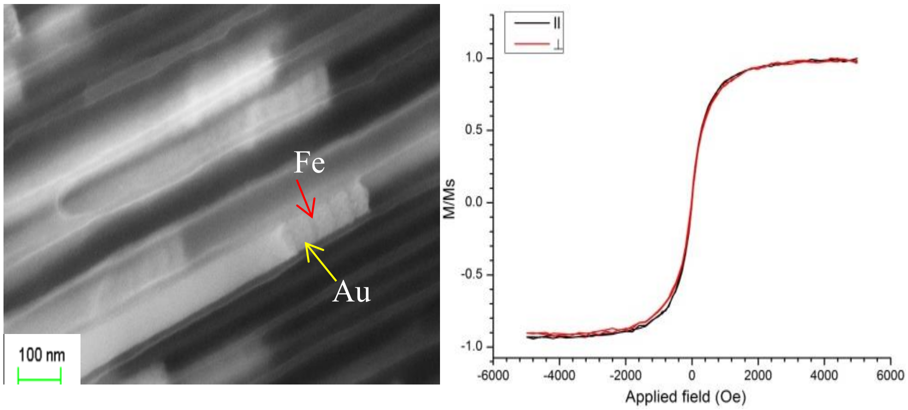

Figure 5.9 Hysteresis loops of Au (25nm)/Fe (10nm) multilayered nanorods

5.4 Summary

In summary, the magnetic properties of multilayered nanorods were characterized by VSM measurements. By comparing these experimental results with theoretical calculations, their magnetic behaviors are explained by the change of shape anisotropy with the aspect ratio (thickness: diameter) of the magnetic segments. The magnetic properties vary from single domain particles with strong shape anisotropy with magnetic easy axis along long axis for long (thickness >> diameter) magnetic segment to single domain particles with very weak anisotropy for disk-shaped magnetic segment to superparamagnetic particles for island-shaped magnetic segment. The effect of the magnetic interaction among nanorods on the measured magnetic properties were also discussed.

Chapter 6

Plasmonic Properties of Multilayered Nanorods

We have fabricated the multilayered nanorods with alternating magnetic layers separated by Au layers. The magnetic properties of such nanorods were discussed in chapter 5. Since Au nanodisks also possess plasmonic properties, so the synthesized nanorods will be multifunctional with both magnetic and plasmonic properties. In this chapter the plasmonic properties of the nanorods will be discussed. This chapter is divided into two parts: 1) the introduction of SPR and the theory explained the phenomenon; 2) the experiment results and finite difference time domain (FDTD) simulation of the optical properties of the nanorods.

6.1 Introduction of Surface Plasmon Resonance (SPR)

Surface plasmon resonance (SPR) is an optical phenomenon arising from the interaction of electromagnetic wave and the conduction electrons in the metal. When a metal is irradiated by light, the electromagnetic field drives the conduction electrons to oscillate coherently with its own resonant frequency, plasma frequency, relative to the lattice of positive ions of nuclei as shown in Figure 6.1.

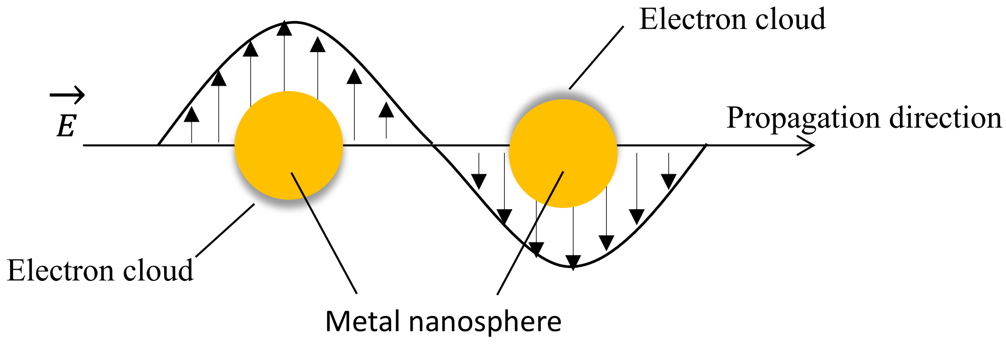

Figure 6.1 Schematic drawing of plasmon oscillation for a sphere

Coulomb interaction between electrons and nuclei cause a restoring force resulting in displacement of electron cloud. The oscillation frequency is determined by 1) the density of electron, 2) the effective electron mass, 3) the shape and 4) the size of the charge distribution [43].

The incident light is absorbed by metal nanosphere at this resonant frequency. Some of the photons will be released with the same frequency in all direction known as scattering while some of them will be converted into phonon and referred as absorption. Therefore, the SPR effect of a nanostructure includes both scattering and absorption. Au, Ag, and Cu have strong SPR peaks in visible light region while the other metals show broad and weak SPR peak in UV region [44]. 5 nm Au nanospheres show single SPR peak at 520nm [10]. For Au nanorods, SPR peaks split into two peaks respect to two difference orientations of the shape of Au nanorods. One peak is in visible region as the light propagates along short axis and another is in near infrared region as the light propagates along long axis of nanorods.

Three theories have been developed to understand this phenomenon: 1) Drude-Lorentz model which explains the interaction of light as electromagnetic wave and free electrons as dipole oscillator in metal of bulk specimen, 2) Mie theory which first describes SPR phenomenon by solving Maxwell's equation for spherical nanoparticles, and 3) Gans theory which is a modification of Mie theory for spheroid.

6.1.1 Drude-Lorentz Model

The classical theory of optical propagation, developed at the end of the nineteenth century following Maxwell's theory of electromagnetic waves, treats the light as electromagnetic waves and the atoms or molecules as classical dipole oscillator [45]. In 1878 Henrick Antoon Lorentz proposed the dipole oscillator formed from the negative charged electron and positive charged nucleus with a magnitude proportional to their separation. The natural resonant frequency ω_0 of atomic dipoles is determined by their mass and the magnitude of the restoring force for small displacement. The restoring force is determined by a spring constant K_s so that the natural frequency ω_0 is written as

$$\omega_0 = \sqrt{\frac{K_s}{\mu}} \tag{6.1}$$

where μ is the reduced mass given by

$$\frac{1}{\mu} = \frac{1}{m_0} + \frac{1}{m_N} \tag{6.2}$$

where m_0 and m_N are masses of electron and nucleus respectively.

Lorentz oscillator considers the interaction between a light wave and an atom with a single resonant frequency ω_0 due to bound electrons. The atomic diploes oscillate as damped harmonic oscillators as following equation.

$$m_0 \frac{d^2 x}{dt^2} + m_0 \gamma \frac{dx}{dt} + m_0 \omega_0^2 x = -eE \tag{6.3}$$

where γ is damping constant, e is magnitude of electric charge, x is displacement, and E is electric field of the light wave. The terms on the left hand side represent the acceleration, damping and restoring force, respectively. The term on the right hand side is the driving force due to the electric field of the light wave.

The application of Lorentz oscillator to the free electron model of metal created by Paul Drude in 1890 [46] is called the Drude-Lorentz model. As the model applies to free electron, the restoring force due to bound electrons is negligible, $\omega_0 = 0$. Considering the oscillations of a free electrons experienced the driving force from the AC electric field E(t) of an electromagnetic wave, the equation of motion of the displacement x of electron is given as

$$m_0 \frac{d^2x}{dt^2} + m_0\gamma \frac{dx}{dt} = -eE(t) = -eE_0 e^{-i\omega t} \tag{6.4}$$

where ω is the frequency of light, and E_0 is amplitude of light.

The left hand side terms represent the acceleration of electrons and the frictional damping force of medium, respectively. The right hand side term represents driving force exerted by the light.

By substituting $x = x_0 e^{-i\omega t}$ into equation (6.4), we obtain the solution as

$$x(t) = \frac{eE(t)}{m_0(\omega^2 + i\gamma\omega)} \tag{6.5}$$

The polarization P of gas is given as

$$P = -Nex \tag{6.6}$$

The electric displacement D is given as

$$\begin{aligned} D &= \varepsilon_r \varepsilon_0 E \\ &= \varepsilon_0 E + P \\ &= \varepsilon_0 E - \frac{Ne^2 E}{m_0(\omega^2 + i\gamma\omega)} \end{aligned} \tag{6.7}$$

where ε_0 is the electric permittivity of free space and ε_r is the relative dielectric constant of the medium.

Therefore, $$\varepsilon_r(\omega) = 1 - \frac{Ne^2}{\varepsilon_0 m_0} \frac{1}{(\omega^2 + i\gamma\omega)} \qquad 6.8)$$

Equation (6.8) is frequently written as

$$\varepsilon_r(\omega) = 1 - \frac{\omega_P^2}{(\omega^2 + i\gamma\omega)} \tag{6.9}$$

where
$$\omega_P = (\frac{Ne^2}{\varepsilon_0 m_0})^{\frac{1}{2}} \tag{6.10}$$

and ω_P is known as the plasma frequency.

In the case of a lightly damp system, $\gamma \approx 0$ so that

$$\varepsilon_r(\omega) = 1 - \frac{\omega_P^2}{\omega^2} \tag{6.11}$$

However, the model is not valid for nanoparticles since the electron density is no longer uniform in nanoparticle but would rather accumulate at the edge of nanoparticles.

6.1.2 Mie Theory

In 1908 Gustav Mie theoretically described the absorption of small spherical metal particle under the radiation of light by solving Maxwell's equations [47]. Mie theory is the exact solution to Maxwell's equation for a plane wave interacting with a homogeneous sphere of radius R with the same dielectric constant as bulk metal. The extinction cross-section (C_{ext}) of sphere includes scattering cross-section and absorption cross-section. The extinction efficiency factor (Q_{ext}) is defined as the ratio of the extinction cross-section (C_{ext}) to the physical cross-sectional area (πR^2). Theoretically, C_{ext} of the sphere can be obtained as a series of multipole oscillations if the boundary conditions are specified [10]. In case of the particle is much smaller than the wavelength of light ($2R \ll \lambda$) only dipole oscillation contributes to C_{ext} and the high order terms in electrodynamic calculation are negligible. Therefore, Mie theory of spherical particles is given as

$$C_{ext} = \frac{24\pi^2 R^3 \varepsilon_m^{3/2}}{\lambda} \frac{\varepsilon_2}{(\varepsilon_1 + 2\varepsilon_m)^2 + \varepsilon_2^2} \tag{6.12}$$

where ε_m is the dielectric constant of surrounding medium, $\varepsilon = \varepsilon_1 + i\varepsilon_2$ is the complex dielectric constant of particle. From equation (6.12), the resonance peak occurs when $\varepsilon_1 = -2\varepsilon_m$.

6.1.3 Gans Theory

In 1912 Richard Gans modified the Mie theory which valid for only spherical particles to include nanorod particles. The shape of a nanorod drastically changes the SPR properties such that the SPR band will split into two modes due to different orientations of nanorods with respect to the electric field of incident light [10]. According to Gans, the extinction cross-section can be written as

$$C_{ext} = \frac{2\pi V}{3\lambda} \varepsilon_m^{3/2} \sum_j \frac{(1/P_j^2)\varepsilon_2}{(\varepsilon_1 + \frac{1-P_j}{P_j}\varepsilon_m)^2 + \varepsilon_2^2} \tag{6.13}$$

where V is the volume of the rods, P_j(j=A, B, C; A>B=C, A=length, B=C= width) are the depolarization factors for elongated particles, which are given by

$$P_A = \frac{1-e^2}{e^2}[\frac{1}{2e}\ln(\frac{1+e}{1-e})-1] \tag{6.14}$$

$$P_B = P_C = \frac{1-P_A}{2} \tag{6.15}$$

where e is the rod ellipticity given by $e^2 = 1-\xi^{-2}$, and ξ is aspect ratio ($\xi = A/B$). Figure 6.2 shows the absorption spectra of Au nanorods with varying aspect ratio calculated from equation 6.13 while the medium dielectric constant is constant at 4. It can be seen that two maxima are present in the simulated absorption spectra corresponding to the transverse and longitudinal resonance across and along the nanorod axes, respectively. The longitudinal plasmon band is continuously shifted from visible region to the near infrared region as the aspect ratio of the nanorods increase whereas the transvers plasmon band is slightly shifted to shorter wavelength.

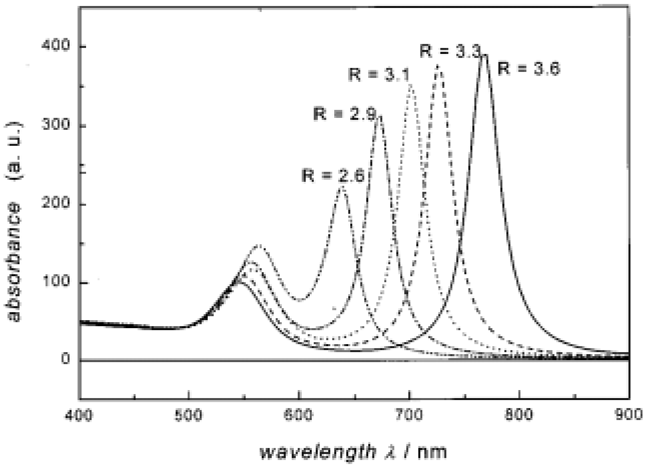

Figure 6.2 Calculated absorption spectra Au nanorods with varying aspect ratio at dielectric constant of the medium at 4 [46].

6.2 Experiment Results and Discussions

In order to study the plasmonic properties of multilayered magnetic nanorods, UV-Vis spectrometer is used in measurement of the absorption of magnetic nanorod suspension in De-ionized water with the incident light scanned from 350nm, close to UV region, to 1100nm in near infrared region. The Finite Difference Time Domain (FDTD) method is employed to investigate the effect of Co segments to plasmonic properties of the nanorods.

6.2.1 UV-Vis Measurements

The samples are divided into three groups: 1) Au/Co nanorods compose of 4 Co long segments separated by 5 Au disks, 2) Au/Co multilayered nanorods with alternating layer of 10 nm Au and 10 nm Co layers, and 3) Au/Co-Co island nanorods.

In group 1, Au/Co nanorods were prepared with three different aspect ratios of Co segments while Au layer thickness is constant with aspect ratio of 0.1.

The samples with aspect ratios of Co segment at 1.25, 2.5, and 3.75 were released from AAO templates and dispersed in deionized water. The samples were sonicated before measuring UV-Vis. The weak pink solution can be observed by naked eyes for samples with aspect ratio 1.25 and 2.5 while sample with aspect ratio 3.75 appears weak blue. UV-vis measurement reveals the absorption peaks at 637.08, 618.04, and 542.92 nm respectively as shown in Figure 6.3. The Au/Co nanorods tend to have absorption peaks shifted to shorter wavelength when the aspect ratio increases.

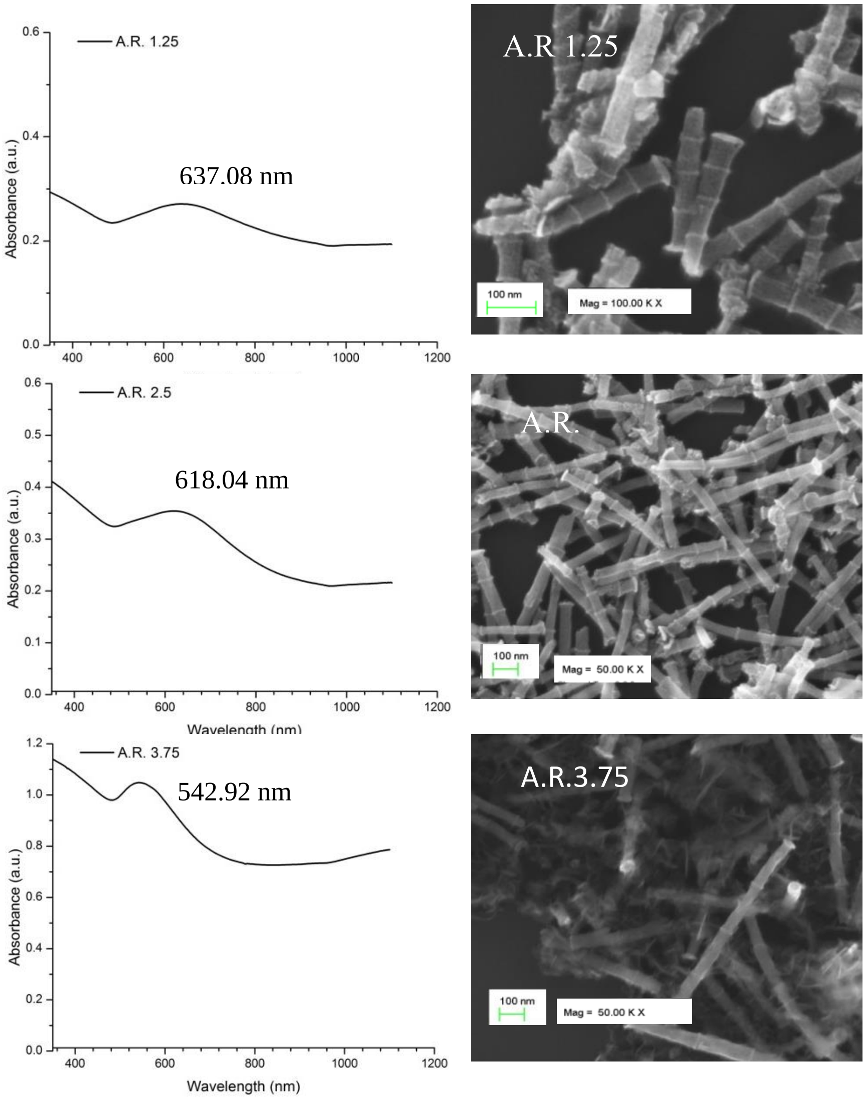

Figure 6.3 Absorption spectra of Au/Co nanorods at different aspect ratio measured by UV-Vis spectrometer.

In group 2, Au/Co multilayered nanorods with aspect ratio 1 and 3.5 were prepared. UV-Vis measurements show a broad peak for sample with A.R. 1 which possibly come from a large size distribution of particles, whereas in longer sample shows two absorption peaks at 620nm and 820nm.

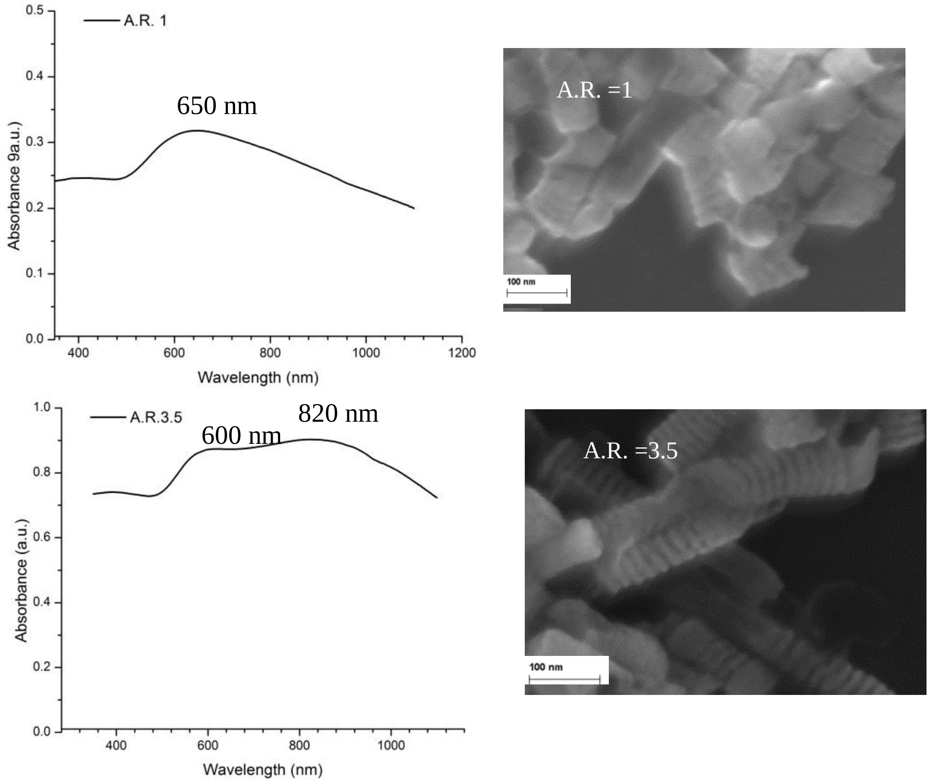

Figure 6.4 Absorption spectra of Au/Co multilayered nanorods at different aspect ratio measured by UV-Vis spectrometer

In group 3, Co segments were electrodeposited at three different deposition times; 10s, 15s, and 20s. All samples exhibit superparamagnetic and SEM micrographs show magnetic nanorods without appearance of alternating layers of Au and Co, and the aspect ratio of the nanorod is approximately 2. The absorption peaks are at 676, 640, and 672 nm, respectively.

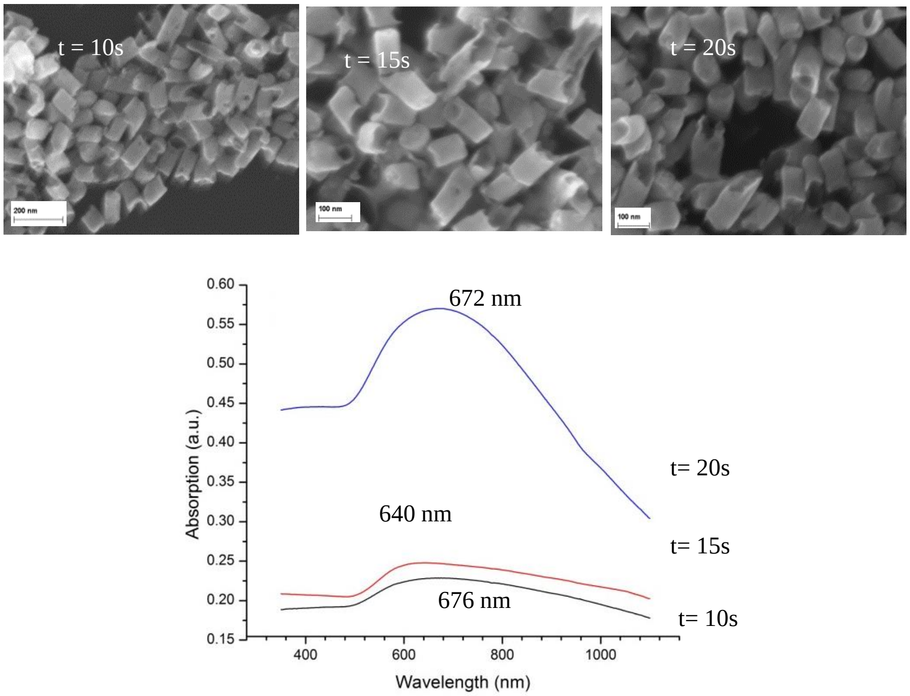

Figure 6.5 Absorption spectra of Au/Co-Co island nanorods at different deposition time but keeping aspect ratios nearly the same measured by UV-Vis spectrometer.

In order to investigate the effect of Co segments to plasmonic properties of the nanorods, the Finite Difference Time Domain (FDTD) method is employed simulate the plasmonic properties of the nanorods.

6.2.2 3D Finite Difference Time Domain (FDTD)

FDTD method is used to calculate how electromagnetic fields propagate from the light source through the structure. It is fully vectorial method that gives both time domain and frequency domain in solving Maxwell's equation. The technique is discrete in both space and time [48]. The electromagnetic fields and structural materials are described on a discrete mesh made of so-called Yee cells which have electric field components form the edges of the cube, and magnetic field components normal to the faces of the cube.

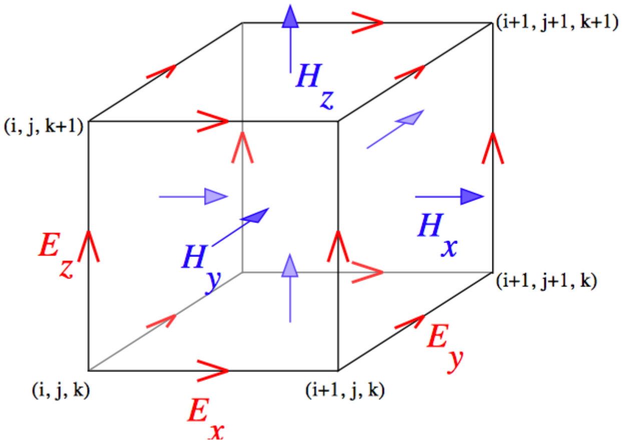

Figure 6.6 Schematic drawing of Yee cell.

In the simulation, light source, material structure and monitors are located in FDTD calculation region which is truncated by six perfectly matched layers (PMLs) boundary. Figure 6.7 shows the components of the simulation setup.

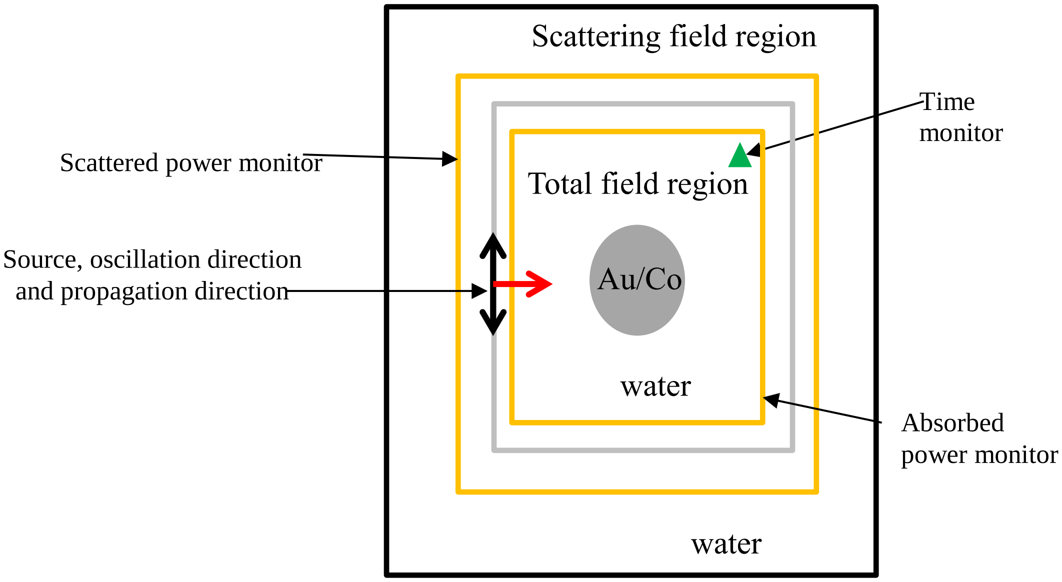

Figure 6.7 Schematic drawing of FDTD setup from xy-plane

Total-field scattered-field (TFSF) source, plane wave, is used as a light source, located in between scattered power monitor and absorbed power monitor. The red arrow shows the propagation direction (k vector) and black arrow shows the polarization (E field vector). The power scattered by the particle can be determined by measuring the power flow through the box of monitors located outside the source in the scattered field region, and the power absorbed by the particle is equal to the power flowing into the box of monitors in total field region. The particle is placed inside the water (medium). Electric field is discrete in time domain (E(t)) so that in every iteration of calculation it is observed by time monitor placed at the corner. Scattering cross-section and absorption cross-section can be calculated and the sum of them is the extinction cross-section.

In experiment, the refractive index and extinction coefficient of Au and Co were imported from the published experimental results by Johnson and Christy [49] and fit to FDTD model as shown in Figure 6.8. Au/Co nanorods with 4 different aspect ratios of Co segments; 0.6, 1.2, 2, and 2.5, were constructed and plane wave incident in two direction, parallel and perpendicular to the nanorod axis (Figure 6.9)

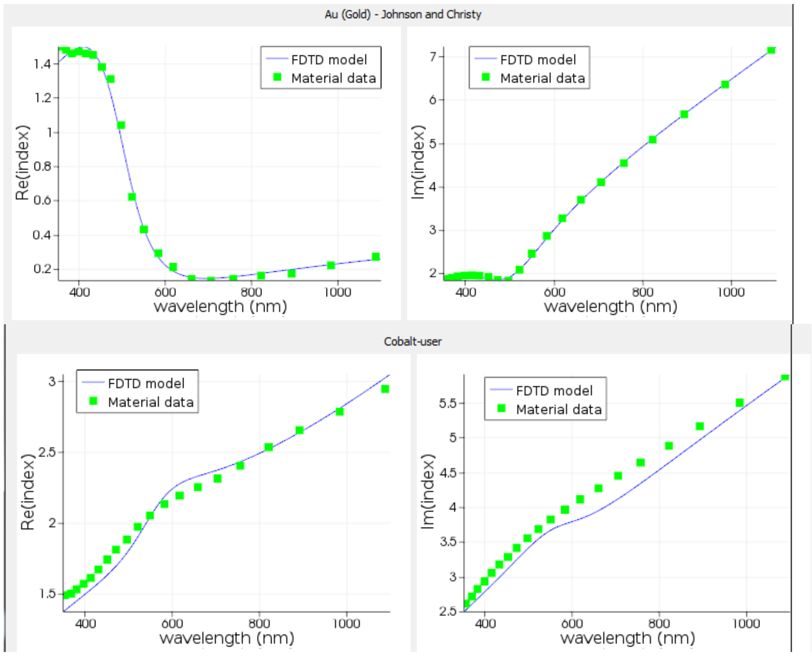

Figure 6.8 Refractive index of (a) Au and (b) Co fit in FDTD model

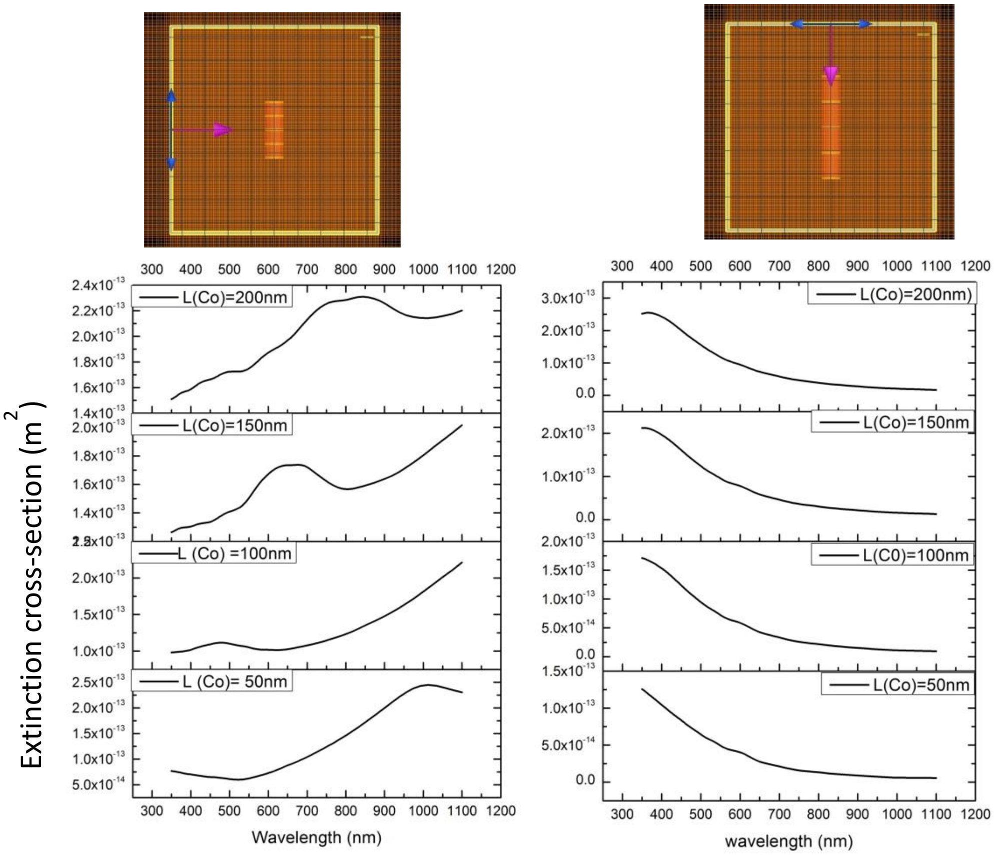

Figure 6.9 Simulated SPR responses of Au/Co nanorods in parallel and perpendicular direction

There is a significant discrepancy between calculated and experimental results (Figure 6.3). The simulation shows SPR peak shifts to higher wavelength with the length of Co segment increases. One possible reason is that in the simulation, surface roughness of Au and Co segments and the interface between two layers are not considered, while the real sample is not perfectly straight and smooth.

Also, for the absorption spectra, interband transition should be taken into account as well as damping which relates to the mean free path for electron and is strongly affected by the particle size. In 2012, Kamiskine and his colleagues [50] studied on size dependent of SPR response of Co colloid. They found that Mie theory only cannot explain its SPR response because for transition metal such as Co the interband transition is quite high due to weak interaction of electrons from s and d shells. Therefore, the dielectric function can be decomposed into two terms, free electron term and interband term [51].

$$\varepsilon_1(r) = 1 - \frac{\omega_P^2}{\omega^2 + \gamma^2(r)} + \varepsilon_{1bound-electrons} \qquad (6.16)$$

$$\varepsilon_2(r) = 1 - \frac{\omega_P^2 \gamma(r)}{\omega(\omega^2 + \gamma^2(r))} + \varepsilon_{2bound-electrons} \qquad (6.17)$$

The damping constant as a function of particle size, r, is given by

$$\gamma(r) = \gamma_{bulk} + \frac{\upsilon_F}{L} \qquad (6.18)$$

where υ_F is the velocity of electron at Fermi surface and L is the effective mean free path for collision with boundary. The comparison of experimental UV-Vis spectra of Co colloid solution with theoretical absorption cross-section curve calculated by Mie theory after modified dielectric function is shown in Figure 6.10.

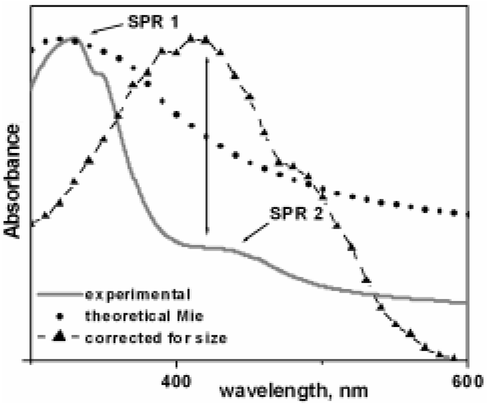

Figure 6.10 Comparison of absorbance spectra from experimental result and from calculated Mie theory and modified dielectric function [51].

Au/Co multilayered nanorods, the following configurations are used in FDTD simulation. The size and thickness are taken from the suggested dimensions of the SEM micrographs of synthesized Au/Co multilayered nanorods, diameter as 80nm, Au layer thickness as 10nm and Co layer thickness as 5nm. There are two samples: (1) 5Au/4Co layers and (2) 11Au/10 Co layers. The FDTD simulation with incident light along long axis shows SPR peaks at approximately 620nm for sample 1 and 800nm for sample 2, as shown in Figure 6.11. SPR peak for sample 1 is in good agreement with the experimental data. For sample 2, FDTD shows single SPR peak at 800nm which is close to the second peak in the experimental result. The first peak of sample 2 is close to the SPR peak for shorter sample which possibly indicates that samples 2 maybe partially break into shorter nanorods during sonication process.

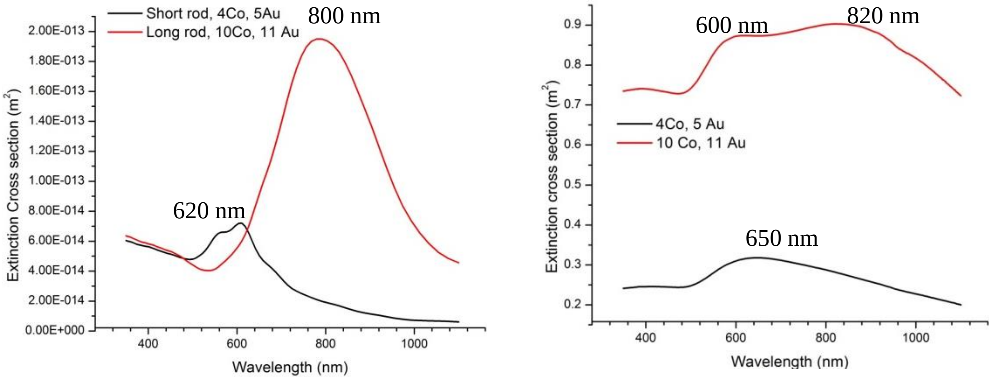

Figure 6.11 FDTD simulation (a) and UV-Vis spectra (b) of Au/Co multilayered nanorods with 10 Co and 4 Co layers

For nanorods with Co particles embedded in Au matrix, the simulation was first conducted just ignoring the inside Co particles, i.e. treating the nanorods just as simple Au nanorods.

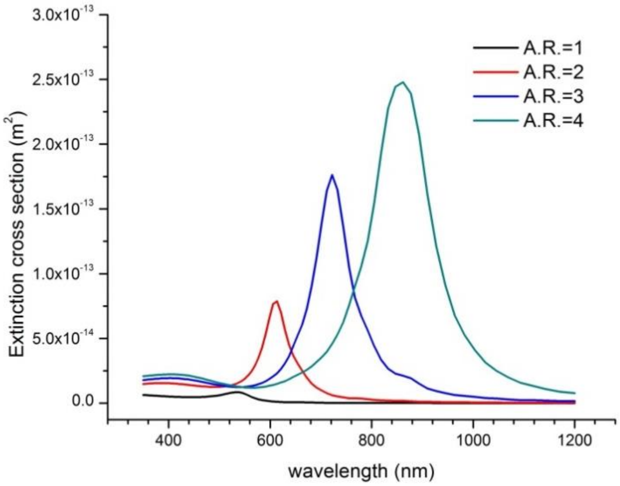

Figure 6.12 FDTD simulations of Au nanorods at aspect ratio 1, 2, 3, and 4.

Figure 6.12 show the FDTD simulation results for Au nanorods with different aspect ratios. The synthesized samples with Co deposition times of 10, 15, and 20s all have the aspect ratio approximately 2. The simulated the SPR peak with aspect ratio of 2 is located at about 610nm which is in good agreement with the experimental data. This suggests that embedded Co has little effect on the optical properties of Au nanoparticles.

6.3 Summary

In summary, the SPR response of multilayered nanorods originated from the Au layers have been investigated with experiments and computer simulations. It has been found that the SPR responses are affected by the aspect ratio of multilayered nanorods while keeping the thickness of Au layers constant with SPR absorption peaks varying from 540 nm to 820 nm. To our knowledge, this is the first time that the SPR properties of multilayered Au nanodisks have been studied, and the findings provide a new way to tune the SPR absorption peak.

Chapter 7

Applications of Multilayered Nanorods

The magnetic nanorods were explored for their bioapplications, including 1) orientation-adjustable ferrogel as cell culture matrix; 2) as MRI contrast agent.

7.1 Ferrogels

Ferrogels are the composite of magnetic nanoparticles embedded in a hydrogel matrix [52]. They represent viscoelastic soft materials which are sensitive to an external applied magnetic field. By applying a homogeneous magnetic field, the individual ferromagnetic nanoparticles will experience the magnetic torque and start to rotate into the direction of the applied field until the magnetic torque is balanced by the torque due to elastic deformation of the gel matrix [53]. In a ferrogel with high concentration of anisotropic ferromagnetic nanoparticles and the nanoparticles are pre-aligned, it is expected that the superposition of magnetic torques acting on each particles leading to a rigid body rotation of the ferrogel. This can be used as a soft actuator [54] which has been demonstrated by S.Monz and his colleagues [55]. In ferrogel, the magnetic properties of nanoparticles and elastic properties of gel are coupled so that shape distortion takes place instantaneously once magnetic field is applied and shape distortion disappears abruptly when magnetic field is removed. This property of ferrogel suggests an application as a micromanipulator or artificial muscles [56]. In 2008, Christain Gollwitzer and his colleagues demonstrated the measurement of the deformation of a ferrogel sphere in a homogeneous magnetic field by direct optical method [57]. As theory predicts a ferrogel sphere is elongated along field direction, and the elongation increases with time similar to mechanic creep experiments. By measuring elongation along the applied field direction comparing to contraction perpendicular to it, the Poisson's ratio of ferrogel can be calculated.

In addition, bioapplications of ferrogels also have been investigated such as drug delivery [58] prepared by co-precipitation of Fe^{2+} and Fe^{3+} to form magnetite (Fe_3O_4) superparamagnetic nanoparticles in presence of polyvinyl alcohol (PVA) solution followed by freezing-thawing cycles of the resulting nanoparticles dispersions, and cancer therapeutics by hyperthermia treatment[59-60]. Heat that generated from magnetite ferrogel subjected to an alternating magnetic field (375 kHz) reaches a stable maximum temperature ranging from 43 ^{0}C to 47 ^{0}C within 5-6 minutes [59].

Here, we demonstrated the alignment of the ferrogel of NiFe nanorods inside gelatin methacrylate (GelMA) in a uniform magnetic field. GelMA is a hydrogel that can be polymerized by photocrosslinking, and GelMA composes of modified natural extracellular matrix component [61], and it is biocompatible with low viscosity [62]. These properties make it an attractive material for tissue engineering applications.

7.1.1 Experiments Details

GelMA synthesis

GelMA was synthesized following the method described by Van DenBulke Al et.al. in literature [62]. Type A porcine skin gelatin (3g) was mixed at 10% (w/v) into Dulbecco's phosphate buffered saline (DPBS) at 50 ^{0}C and stirred until fully dissolved at 500 rpm. While 0.375 ml of methacrylic anhydride (MA) was added to the gelatin solution at 0.5ml/min and allowed the reaction occurred for 1 h. To stop the reaction, the solution was diluted by adding 5x warm (40^{0}C) DPBS. Then the mixture was dialyzed against deionized water using 12-14kDa cutoff dialysis tubing for 1 week at 40 ^{0}C to remove salt and methacrylic acid. Figure 7.1 shows GelMA macromers containing amine group react with MA.

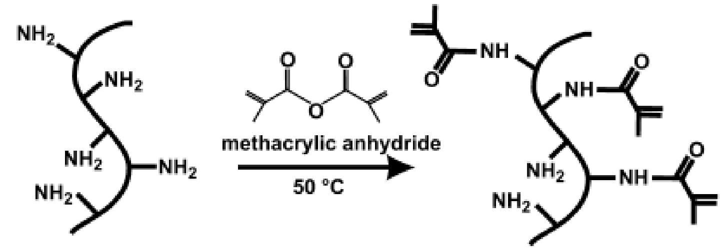

Figure 7.1 Gelatin macromers react with MA [61]

NiFe nanorod fabrication

NiFe nanorods were electrodeposition in AAO template using an electrolyte containing Ni and Fe ions at -1.1 V (Vs. Ag/AgCl Sat. (KCl)), and the length of nanorods was controlled by passing charge of 1C. The NiFe nanorods were released from template by dissolution of AAO in 2M NaOH. The prepared NiFe nanorods have diameter approximately 70nm and 1 um in length as shown in Figure 7.2.

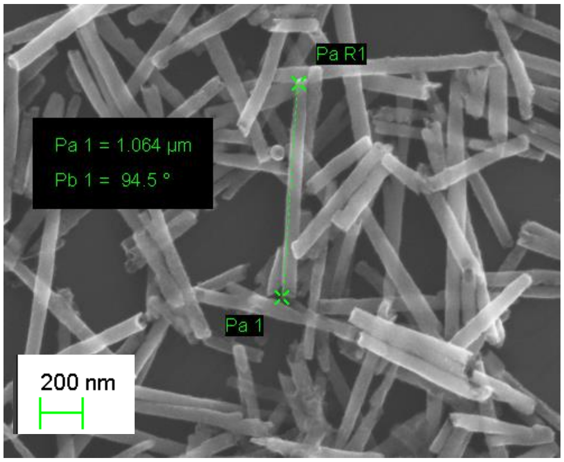

Figure 7.2 SEM micrograph of fabricated NiFe nanorods for ferrogel

Ferrogel preparation

Ferrogel was prepared by adding 0.1mg NiFe nanorods in 1mL of 10% GelMA which was liquefied in 40^0C water bath. Ultrasonicator was used to enable uniform dispersion of NiFe nanorods in GelMA. Then 3mM of photoinitiator was added to the mixture which enables photopolymerization under

UV irradiation. Photoinitiator used in this experiment is lithium phenyl-2, 4, 6-trimethylbenzoylphosphinate (LAP), and its chemical structure is shown in Figure 7.3.

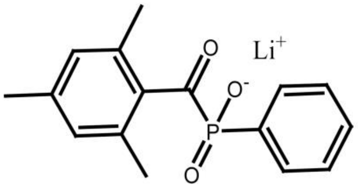

Figure 7.3 Chemical structure of lithium phenyl-2, 4, 6-trimethylbenzoylphosphinate (LAP) [63].

After that, the mixture was transferred to 5x5x5 mm^3 polystyrene container. In order to align NiFe nanorods along magnetic field direction, the mixture was magnetized in 10 kOe uniform magnetic under the irradiation of UV light for 6 min. LAP enables photocrosslink in GelMA and then the mixture was solidified to form ferrogel with aligned magnetic rods. The alignment setup is shown in Figure 7.4.

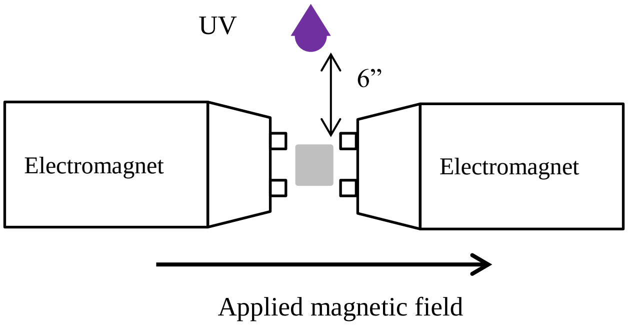

Figure 7.4 Schematic diagram of magnetic alignment of ferrogel

7.1.2 Magnetic Properties of Ferrogel

Magnetic properties of ferrogel were measured using VSM with magnetic field in parallel and perpendicular to the alignment field direction. The NiFe in AAO was measured by VSM as well and used as reference sample to verify the alignment of ferrogel. The hysteresis loops of ferrogel and reference sample are shown in Figure 7.5 and the magnetic parameters are listed in Table 7.1.

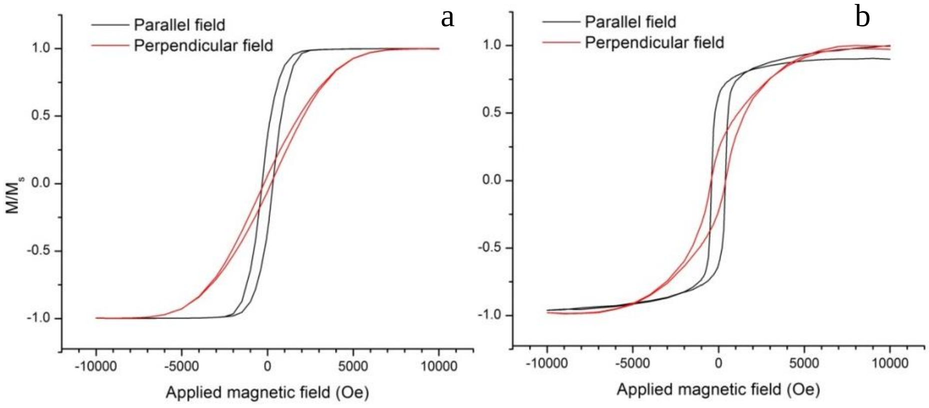

Figure 7.5 Hysteresis loops of (a) NiFe nanorods in AAO template and (b) ferrogel in parallel and perpendicular direction

Table 7.1 Magnetic properties measured by VSM of NiFe nanorods inside AAO and ferrogel with applied field in parallel and perpendicular to the long axis of the nanorods.

Sample	Parallel direction				
	Remanence (M_r, memu)	Saturation moment (M_s,memu)	Remanence ratio (M_r/M_s)	Coercivity field (H_c, Oe)	Saturation field (H_s, Oe)
NiFe	1.2	3.4	0.35	300	3000
Ferrogel	0.34	0.44	0.77	400	2000
Perpendicular direction					
NiFe	0.2	3.4	0.06	200	7000
Ferrogel	0.06	0.34	0.18	350	7000

NiFe nanorods in AAO template is used as a reference sample since the nanorods are fixed and the long axis direction is known.. Therefore, the alignment of nanorods in ferrogel can be verified by simply comparing the hysteresis loops.

The hysteresis loop of NiFe nanorods in AAO shows clear shape anisotropy with easy axis in parallel to the long axis (channel direction) and hard axis in short axis. Hysteresis loop of ferrogel shows similar behavior to the nanorods in AAO, indicating the alignment of NiFe nanorods inside the gel matrix. The hysteresis loop in parallel direction of NiFe nanorods in AAO template is slightly shear while in ferrogel is relatively squarer. This suggests that there is dipole-dipole interaction between nanorods in AAO since they are closely packed while in ferrogel the interaction is negligible because of much lower concentration of nanorods leading to well separated configuration.

The high remanence for NiFe nanorods in AAO suggests that they are single domain particles. The prepared NiFe nanorods have diameter of 70nm and the length is approximately 1 um, which makes aspect ratio of 14. They can be considered as prolate spheroids. A critical radius r_{sd} (radius of nanorod) for single domain particle can be expressed [15] as

$$r_{sd} = \sqrt{\frac{6A}{N_C M_S^2}[\ln(\frac{2r_{sd}}{a_1} - 1)]} \qquad (7.1)$$

where A is stiffness constant (erg/cm), N_C is the demagnetizing factor in long axis, M_s is the saturation magnetization (emu/cm^3), and a_1 is lattice parameter (cm). To calculate critical radius for NiFe rods, $A=1.3 \times 10^{-6}$ erg/cm, $M_s=800$ emu/cm^3, and $a_1=0.355$ nm (parameters for $Ni_{80}Fe_{20}$) are used, and N_c is calculated according to prolate spheroid :

$$N_C = 4\pi \frac{1}{m^2 - 1} \times [\frac{m}{2(m^2-1)^{1/2}} \times \ln(\frac{m + (m^2-1)^{1/2}}{m - (m^2-1)^{1/2}}) - 1] \qquad (7.2)$$

where m is the aspect ratio of spheroid.

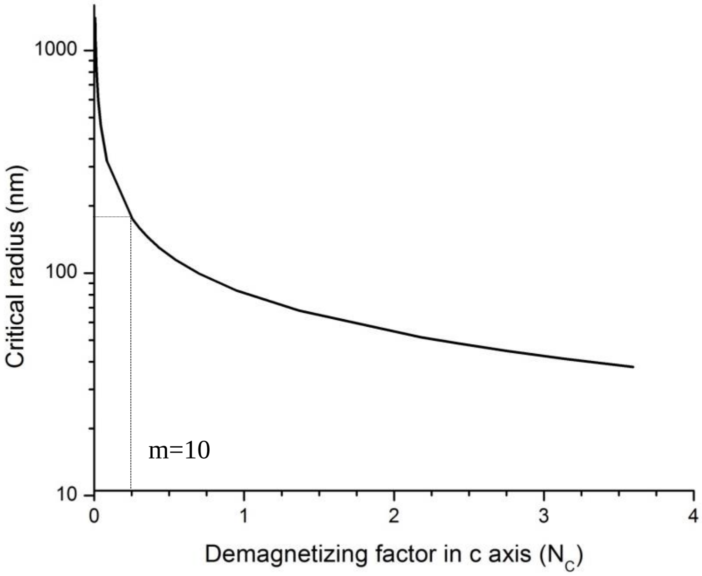

Figure 7.6 Calculation of critical radius for single domain particle for Ni80Fe20 as a function of demagnetizing factor in c axis.

The critical radius for single domain particle at aspect ratio of 10 is about 200nm. The radius of nanorods is about 35nm, way below the critical radius. It is confirmed in both calculation and experiment that Prepared NiFe nanorods are single domain particles.

Considering magnetization reversal in single domain particles, two magnetization reversal models are proposed; coherent model and curling model. In coherent rotation model, all magnetic moment remain parallel to each other and rotate away from easy axis during reversal process. In this process, the demagnetization energy increases when there is a magnetization component along hard axis while exchange energy is minimized. In curling model, the magnetic moments are not maintained to parallel to each other so that there is no net magnetization along hard axis, then demagnetization energy is minimized whereas the exchange energy increased. Figure 7.7 shows coherent and curling model of the magnetization reversal in single domain prolate spheroid.

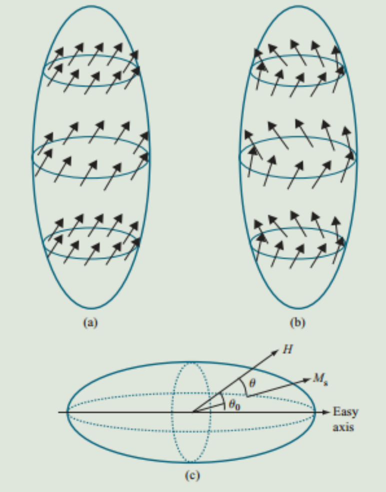

Figure 7.7 Coherent (a) and curling (b) model of the magnetization reversal in single domain prolate spheroid, (c) configuration of applied magnetic field H, saturation magnetization Ms and easy axis of spheroid [15].

The competition between exchange energy and demagnetization energy determines the magnetization reversal mode. There is a critical size for the transition between these two magnetization reversal modes that can be calculated as followed equation.

$$r_c = q\left(\frac{2}{N_a}\right)^{1/2} \frac{A^{1/2}}{M_s} \qquad (7.2)$$

where r_c is the critical radius (cm), q is the smallest solution of the Bessel functions which related to aspect ratio of spheroid, N_a is demagnetizing factor in short axis, A is the exchange stiffness constant (erg/cm), and M_s is saturation magnetization (emu/cm^3). The value of q varies between the limit of 1.8412 for an infinite aspect ratio cylinder and 2.0816 for a sphere with aspect ratio of 1 [15]. Using this equation, the critical radius for prepared NiFe nanorods is calculated as approximately 15nm. The actual radius of nanorods is 35 nm which is larger than the critical radius, so that the magnetization reversal process in these nanorods will be in curling mode.

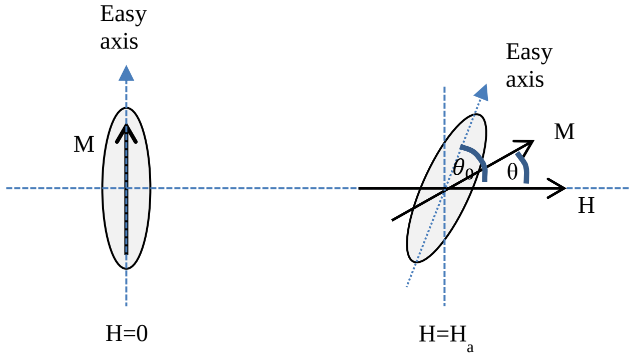

Figure 7.8 Schematic demonstrations the rotation of magnetic nanorods in gel matrix in presence of an external magnetic field

As illustration in Figure 7.8, in absence of an external magnetic field the magnetization $\overrightarrow{M}$ prefers to align along easy axis. When an external magnetic field is applied, magnetization $\overrightarrow{M}$ rotates out of the easy axis by curling and tends to align in field direction. However, at a finite external field, H, the torque acting on the magnetic moment will be transferred to the nanorod, as a result, the entire particle will rotate until the magnetic torque is balanced by the torque due to the elastic deformation of the gel.

7.2 Cytotoxicity Study ofNanorods using MTT Assay

Cytotoxicity of Au/Co nanorods and Au/Co multilayered nanorods was performed using MTT assay. In this experiment, approximately 3000 3T3 fibroblast cells were seeded in 96-well plate with DMEM (Dulbecco's modified eagle medium) cell culture media, and then were incubated in incubator for 24 hours at 37 ^{0}C in a 5% CO_2 atmosphere. The suspensions of nanorods in DMEM at three different concentrations, 12.5, 50, 100 $\mu g / ml$, were prepared and then were added to the plates. The cells that were exposed to nanorod solutions were separated into two groups according to different incubation time. Group I was incubated for 24 hours and group II was incubated for 72 hours. Cells exposed to Au/Co nanorods solution were named as AuCo samples while cells that exposed to Au/Co multilayered nanorod solution were named as IS samples.

After incubation, DMEM was aspirated from each well and then the cells were rinsed by phosphate buffered saline (PBS). After that, 90 μl of DMEM and 10 μl of MTT (3-(4,5-dimethylthiazol-2-yl) -2,5-diphenyltetrazolium bromide) were added to each well and the cells were further incubated again for 4 hours. During incubation, living cells or viable cells convert yellow colored MTT to insoluble purple colored formazan. When cells die, they lose this ability so that color formation serves as a useful and convenient marker of the viable cells. Formazan accumulates as an insoluble precipitate inside cells as well as being deposited near the cell surface and in DMEM [64]. After incubation, the remaining MTT solution was removed, and dimethyl sulfoxide (DMSO) was added to dissolve formazan. Then the plates were rotated for 5 minutes for evenly distribution before measuring the absorbance of formazan with a microplate reader with a 490nm light source. The untreated cells with DMEM were used as a control sample (TCPS).

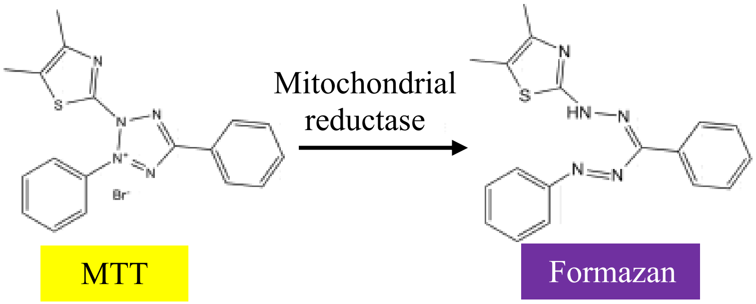

Figure 7.9 Chemical structures of MTT and formazan after MTT was reduced by metabolism of viable cells.

Absorbance is a function of concentration of formazan which correlates to the level of cell metabolism in viable cells. The absorbance of samples in group I is reduced to approximately 50% of the control sample in all cases as shown in Figure 7.10. On the other hand, after 72 hours of incubation of samples in group

II, cells grew and increased in number so that the reduction rate of MTT is higher and consequently the absorbance is higher.

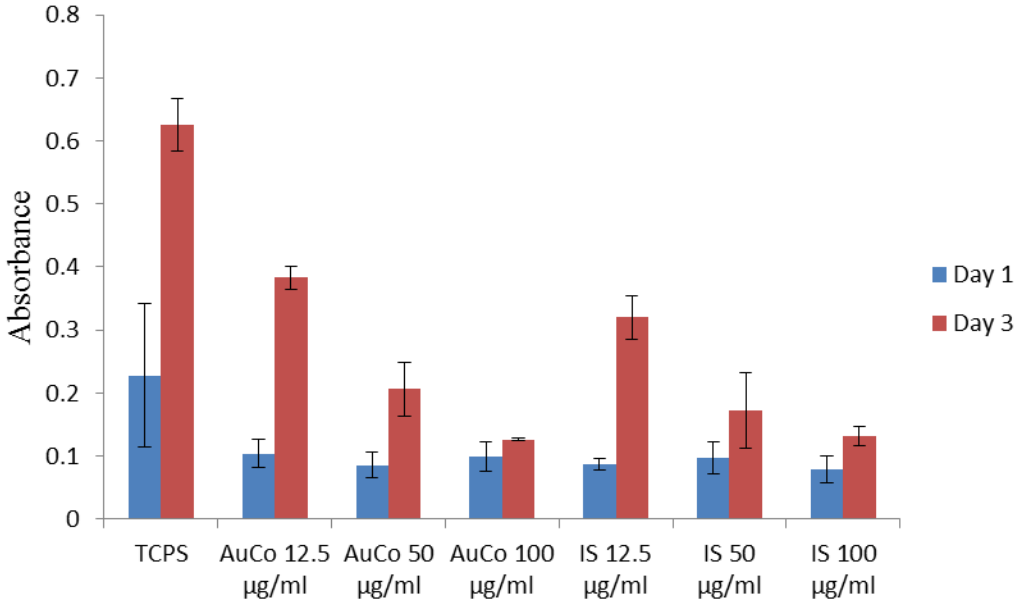

Figure 7.10 Absorbance of fibroblast cell exposed to nanorod solution at different concentration and incubated for 24h and 72h.

Figure 7.11 shows the images of samples that were incubated for 24 hours. The cell morphologies with 12.5ug/ml AuCo and IS are similar to the control TCPS, but the density is slightly lower at the concentration of 50ug/ml. The morphologies are still similar but there are some cells that are not spread out and show circular shape. At the concentration of 100ug/ml, cells are no longer having spindle morphology.

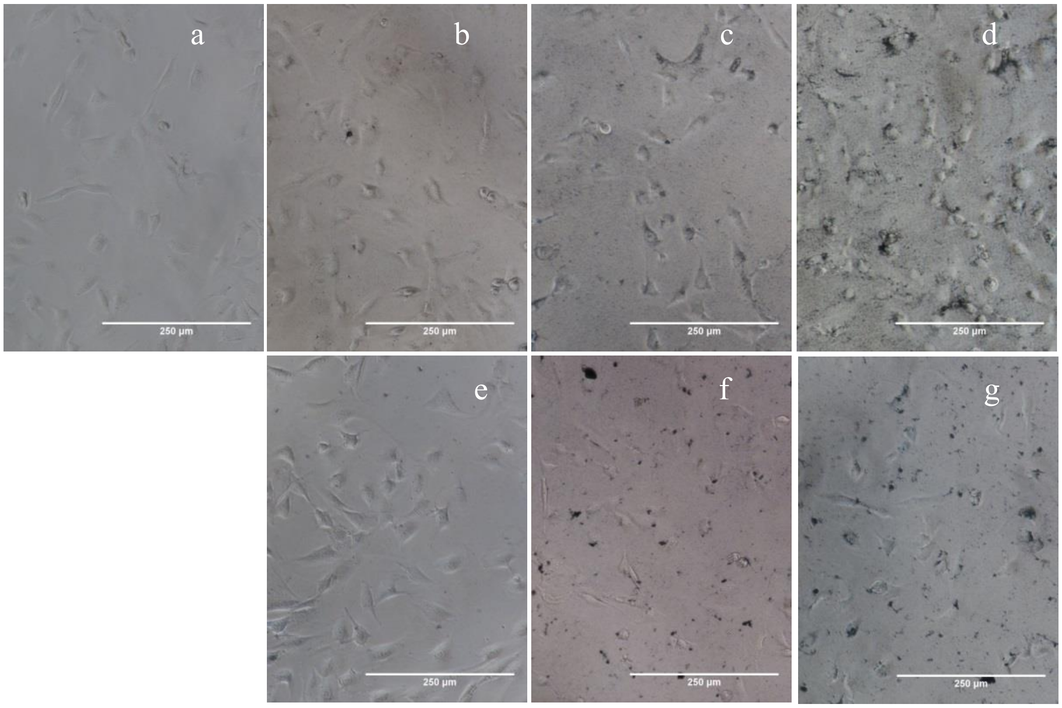

Figure 7.11 Light microscope images of cells incubated 24 h (a) untreated cells (TPCS), (b) with 12.5 ug/ml AuCo, (c) with 50 ug/ml AuCo, (d) 100ug/ml AuCo (e) 12.5 ug/ml IS, (f) 50 ug/ml IS, and (g) 100ug/ml IS.

After 72 hours of incubations, at concentration of 12ug/ml it shows cell proliferate well and cell morphology is similar to TCPS. At concentrations of 50ug/ml and 100ul/mg there are aggregations of nanorods near cells that are not observed in the sample with 24 hour incubation time. In addition, cells did not proliferate well at concentration 100ug/ml.

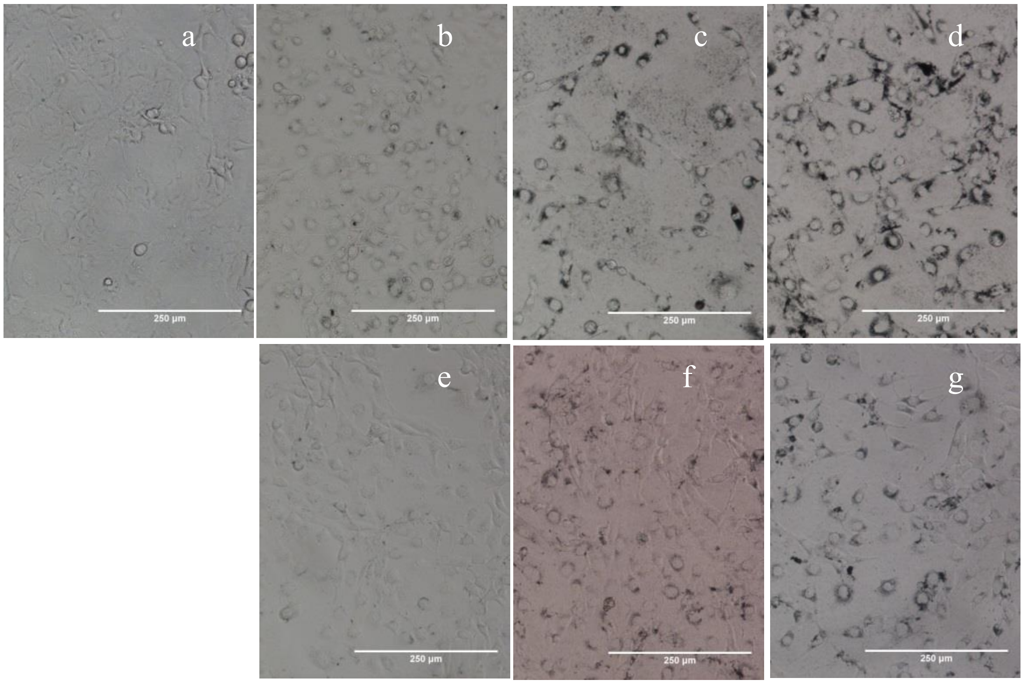

Figure 7.12 Light microscope images of cells incubated 72 h (a) untreated cells (TPCS), (b) with 12.5 ug/ml AuCo, (c) with 50 ug/ml AuCo, (d) 100ug/ml AuCo (e) 12.5 ug/ml IS, (f) 50 ug/ml IS, and (g) 100ug/ml IS

Cells were dyed to distinguish dead and live cells. For 24 hour incubation time, there are increasingly more dead cells as the concentration of nanorods increases whereas cell morphology are similar in all cases. For 72 hour incubation, at the concentration of 12.5 ug/ml cells proliferate well. However, more dead cells are observed at higher concentrations. Cell morphology also starts to change and shows less elongate.

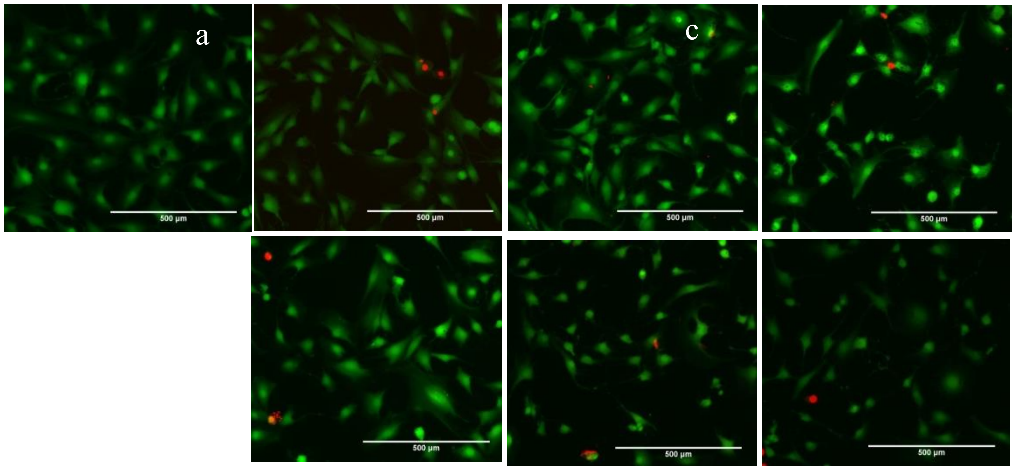

Figure 7.13 Light microscope images of dyed cells incubated 24 h (a) untreated cells (TPCS), (b) 12.5 ug/ml AuCo, (c) 50 ug/ml AuCo, (d) 100ug/ml AuCo, (e) 12.5 ug/ml IS, (f) 50 ug/ml IS, and (g) 100ug/ml IS.

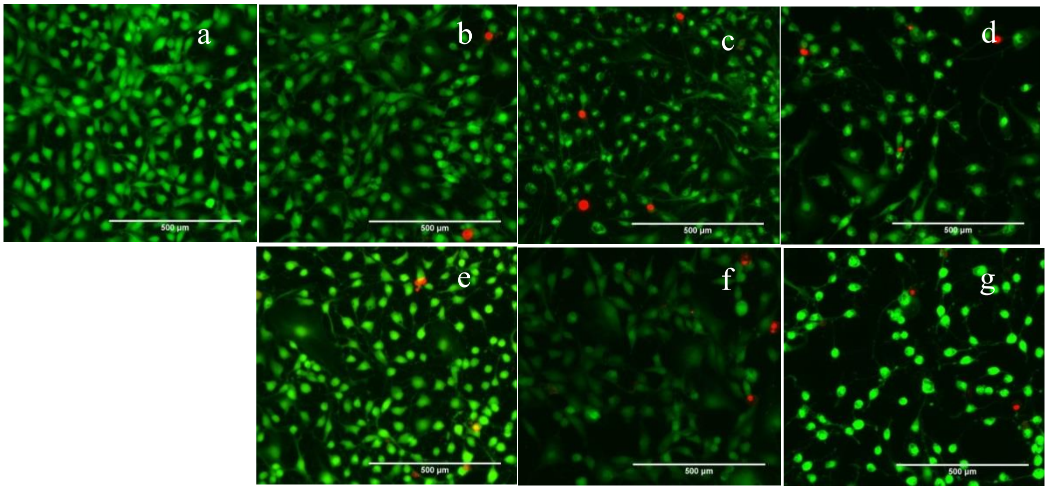

Figure 7.14 Light microscope images of dyed cells incubated 72 h (a) untreated cells (TPCS), (b) 12.5 ug/ml AuCo, (c) 50 ug/ml AuCo, (d) 100ug/ml AuCo, (e) 12.5 ug/ml IS, (f) 50 ug/ml IS, and (g) 100ug/ml IS.

Cell viability was quantified by counting live cells and dead cells in 1200 um x 900 um area, and random areas were chosen in well plate. It shows that cell viability decreases as the concentration of the nanorods increases, indicating some cytotoxicity. The toxicity most likely comes from the Co segments. This result suggests that to use Au/Co nanorods for bioapplications such as the application in the following section, insulating Co is necessary.

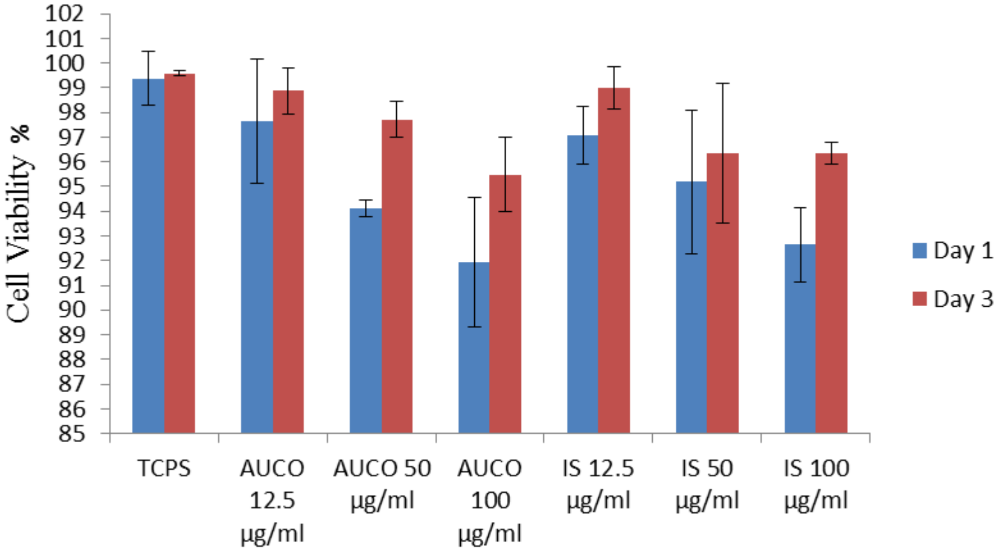

Figure 7.15 Cell viability of fibroblast cell exposed to nanorod solution at different concentration and incubated for 24h and 72h.

7.3 Au/Co Multilayered Nanorods as MRI Contrast Agent

Magnetic resonance imaging (MRI) relies on the counterbalance between the small magnetic moment on a proton and the large numbers of protons present in the tissue, and this effect can be measured in the presence of a large magnetic field [65]. In magnetic field, spins of hydrogen nuclear align parallel or antiparallel to the external magnetic field (B_0) as shown in Figure 7.16. The energy difference between these two states of spins can be defined as

$$\Delta E = \gamma h B_0 / 2\pi \tag{7.3}$$

where γ is gyromagnetic ratio, $\gamma = 2.67 \times 10^{8} rads^{-1} T^{-1}$, B_0 is external magnetic field (Tesla,T), h is Plank's constant, $h = 6.62 \times 10^{-27} erg \sec$.

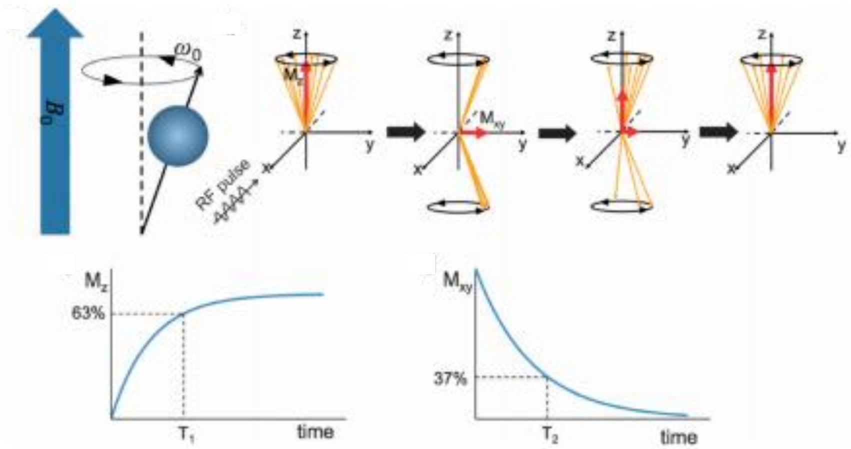

Figure 7.16 Schematic drawing the principle of MRI [66].

By applying a time varying radiofrequency (rf) field perpendicular to external magnetic field B_0 with frequency corresponds to Larmor frequency, ω_0 ,($\omega_0 = \gamma B_0$) which is typically 5-100MHz, the nuclei absorb the electromagnetic energy and the antiparallel spin population increases. As a result, longitudinal magnetization (M_Z) decreases, while transverse magnetization (M_{xy}) is generated. In absence of rf field, the nuclear spins return to their initial state termed as relaxation. The relaxation signals are given as [60]

$$M_Z = M(1 - e^{-t/T_1}) \tag{7.4}$$

And

$$M_{xy} = M \sin(\omega_0 t + \phi) e^{-t/T_2} \tag{7.5}$$

where T_1 and T_2 are longitudinal (spin-lattice) and transverse (spin-spin) relaxation times, respectively, and ϕ is phase constant.

In relaxation processes, T_1 is the time required for M_z to recover back to 63% of the equilibrium value, whereas T_2 is the time required for M_{xy} to decay to 37% of its initial magnitude. The longitudinal relaxation reflects a loss of energy as a heat to the surrounding lattice. It is primarily a measure of dipole coupling of the photon moments to their surroundings. On the other hand, the transverse relaxation in xy-plane is driven by the loss phase coherence in the precessing protons due to their magnetic interactions with each other. Local inhomogeneity in the applied longitudinal field affects dephasing, leading to shorter relaxation time T_2^* which is defined as

$$\frac{1}{T_2^*} = \frac{1}{T_2} + \gamma \frac{\Delta B_0}{2} \tag{7.6}$$

where ΔB_0 is the variation in the field caused by either distortion in homogeneity of applied field or by local variations in magnetic susceptibility of system. Because of difference in relaxation, tissues can be differentiated.

The effect of T_1 and T_2 relaxation times on MR signal intensity is dependent on 1) the repetition time (T_R) which is defined as time interval between application of transverse rf pulse, and 2) the echo time (T_E) which is the time between the initial transverse rf pulse and the measurement. For standard spin echo pulse sequence with repetition time T_R and spin echo time T_E the MRI signal intensity is expressed [67] by

$$SI = \rho(H)\exp(-T_E / T_2)[1 - \exp(-T_R / T_1)] \tag{7.7}$$

where $\rho(H)$ is the local proton density.

T_1-weigthed image uses a short T_R ($T_R < 1000$ms) and short T_E ($T_E <$ 30ms) [68], allowing full recovery of tissues with short T_1 and partially recovery of tissues with long T_1 so that tissues with short T_1 appear bright in T_1-weighted images. On the other hand, T_2-weigthed image uses long T_R ($T_R > 2000$ms) and long T_E ($T_E > 80$ms) [68], so that tissues with short T_2 lose their transverse magnetization and appear dark. In addition, at short T_E ($T_E < 30$ms) and long T_R ($T_R > 2000$ms) neither T_1 nor T_2 is weighted [66]. In this case, the signal intensity is proportional to the amount of proton and proton-weighted images are obtained. In contrary, low contrast images were generated if T_R is short and T_E is long. The relationship between T_R and T_E and tissue contrast corresponding to each condition are shown in Figure 7.17.

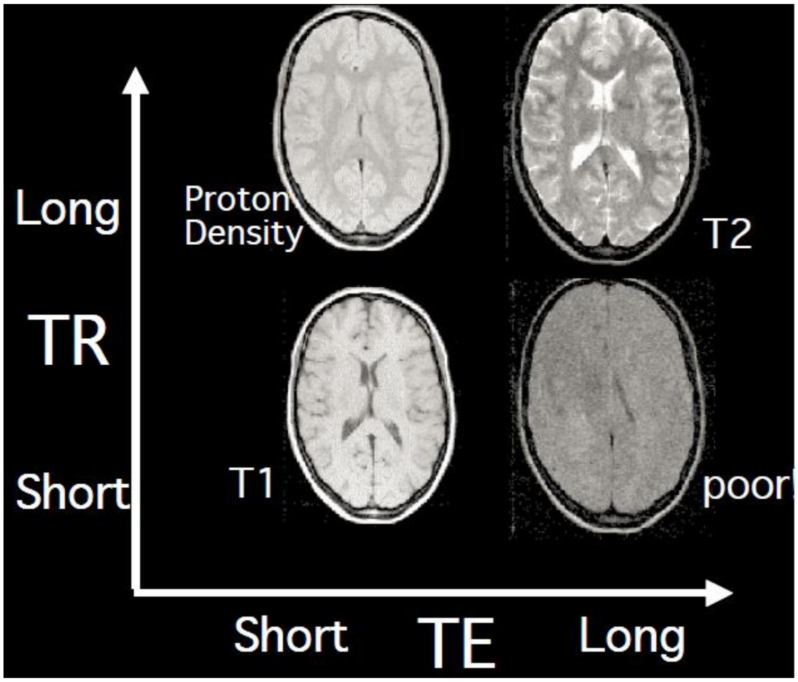

Figure 7.17 Relationship between TR and TE and tissue contrast corresponding to each condition [69].

Contrast agents are employed to improve the visibility of substances by changing the relaxation time around the agents. The efficiency by which these contrast agents shorten the relaxation times are called relaxivities r_1 and r_2 according to

$$R_i = \frac{1}{T_i} = \frac{1}{T_{i0}} + r_i C \qquad (7.8)$$

where R_i is the relaxation rate of the aqueous solution, T_{i0} is the relaxation time in the absence of the contrast agent, C is the concentration of the contrast agent (mM), and r_i is its relaxivity ($s^{-1}mM^{-1}$).

By inserting relaxation rate in equation 7.8 to equation 7.7, the MRI signal intensity of any chosen pair of T_E and T_R becomes a function of the relaxivity value r_1 and r_2 and concentration C of the contrast agent and can be expressed as

$$SI = \rho(H)\exp(-T_E / T_{20})\exp(-T_E r_2 C)[1 - \exp(-T_R / T_{10})\exp(-T_R r_1 C)] \qquad (7.9)$$

Here, Au/Co multilayered nanorods were studied for the possibility of using them as MRI contrast agent. Au/Co multilayered nanorods were coated with inert metal palladium (Pd) to make it more biocompatible, a two-step coating process developed in our lab was used. The nanorods were first coated with Cu by an electroless deposition process. Then, the Cu layer is replaced by Pd through a galvanic reaction. The HRTEM image in Figure 7.18 clearly shows the core-shell configuration with multilayered nanorod in the center and a Pd layer in shell.

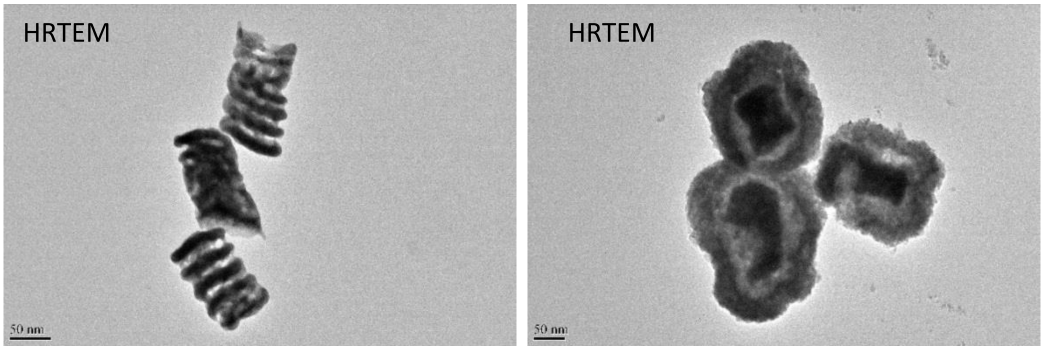

Figure 7.18 HRTEM images of (a) Au/Co multilayered nanorods before and (b) after coated with ^{103}Pd .

The samples with 5 difference concentrations of Co were prepared. Using Di water as control, these samples were tested as T2 contrast agent. The samples were subjected to magnetic field strength of 1T, and T_2–weighted images corresponding to difference concentrations of Co are shown in Figure 7.19. The quantitative analysis of the results gives the relaxivity of the nanorods as 56.3 $mM^{-1}s^{-1}$. These results clearly show that Au/Co multilayered nanorods can act as T_2-contrast agent

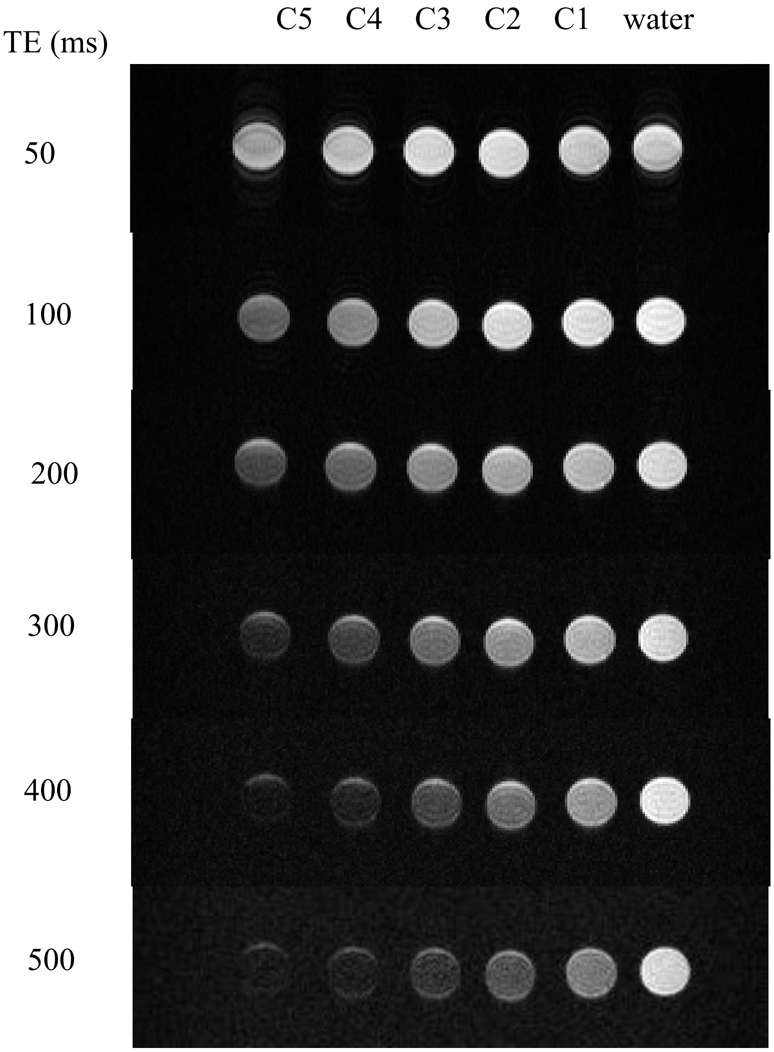

Figure 7.19 T2-weighted MR images of Au-Co nanorods samples with their corresponding concentrations

Table 7.2 Relaxation time (T2) corresponding to Co concentration

	T2 (ms)	Cobalt (uM)
water	833	0
C1	416	18.47965648
C2	344	32.1181811
C3	250	45.35475633
C4	222	66.9383479
C5	161	83.11391967

7.4 Summary

In summary, two bioapplications of multilayered nanorods are discussed: 1) as magnetic components in orientation-adjustable ferrogel for cell culture and 2) as MRI contrast agent. In ferrogel, VSM measurements confirm alignment of magnetic phase in gel matrix, demonstrating such nanorods can be mixed with hydrogel to produce 3D cell culture matrix with the capability to change the alignment. Cytotoxicity of Au/Co nanorods and Au/Co multilayered nanorods were also studied by MTT assay with 3T3 cells. The results show that cell proliferation decreases as the concentration of nanorods increases and the nanorods tend to aggregate around the cells causing the cell mophology change. These results indicate that the nanorods need to be covered with inert material to prevent the direct cell exposure to Co. The nanorods were coated with Pd and tested as MRI contrast agent. The MRI images clearly show significant contrast enhancement with nanorods. A high relaxivity was also observed. More experiments and theoretic considerations are needed to fully understand such phenomenon.

Chapter 8

Summary

We fabricated multilayered nanorods consisting of alternating layers of Au and magnetic materials. Three types of multilayered nanorods were synthesized using templated electrodeposition into Anodic Aluminum Oxide (AAO) membrane: Au/NiFe; Au/Fe and Au/Co. AAO template was chosen because of its well defined structure of hexagonally arranged straight pores and it has been utilized to generate large quantity of nanorods without requirement of a sophisticated lithographic instrument. We made our own AAO membranes in the lab with feature size ranging from 40nm to 80 nm of pore diameter and thickness of 10um to 12um.

The magnetic properties of such nanorods are tunable through their shape anisotropy. They can vary from single domain nanoparticles to superparamagnetic nanoparticles.

Au/NiFe nanorods were synthesized by respective electrodeposition of Au and NiFe. NiFe segment was deposited using an electrolyte containing both Ni and Fe ions, and electrodeposition conditions including electrolyte composition and deposition potential and time were tuned to make the alloy with the composition of Ni 80% and Fe 20% that is called permalloy. Permalloy was chosen owing to its soft magnetic properties; its magnetocrystalline anisotropy is near zero and its high magnetization of 800emu/cm^3. Au/NiFe/Au nanorods with aspect ratio of about one show no shape anisotropy. However, as the aspect ratio increases the hysteresis loops reveal stronger shape anisotropy with easy axis parallel to nanorod axis and hard axis perpendicular to nanorod axis.

Au/Fe nanorods were fabricated by electrodeposition using an electrolyte containing both Au and Fe ions. In such electrolyte, Au ion concentration was much less than that of Fe ions. Taking advantage of the large difference in equilibrium reduction potentials of Au and Fe, simply varying deposition potential, Au and Fe segments can be deposited. When Au was deposited, no deposition of Fe took place. When Fe was deposited, Au could also be deposited. However, since the Au ion concentration is much lower than Fe, co-deposited Au was negligible. It has been found that Au/Fe nanorods exhibit superparamagnetic behavior when Fe layer is thinner than 10nm.

Au/Co nanorods were also fabricated by electrodeposition of Au and Co using an electrolyte containing both Au and Co ions. In nanorods with long Co segments, strong shape anisotropy with easy axis along nanorod axis and hard axis perpendicular to nanorod axis was observed and compared with calculated values. However, in nanorods with thin Co layers(Au/Co multilayered nanorods), a very weak anisotropy with the easy axis aligned on nanorods axis and hard axis perpendicular to nanorod axis is observed, indicating strong interaction between neighboring Co layers through a thin Au layer. Also this also leads to a low remanence. Further decreasing the electrodeposition time of Co, Co layers are no longer as continuous film, forming Co islands covered by Au. This kind of nanorods exhibits superparamagnetic behavior which is a desirable property for bioapplications.

Au layers in multilayered nanorods not only can serve as anchorage sites for biomolecule attachment, but also possess special optical properties, surface plasmon resonance (SPR) properties. SPR properties of Au/Co nanorods was measured and studied in both experiments and Finite Difference Time Domain (FDTD) simulations. Au layers were kept constant at approximately 10nm whereas Co layers were varied from 200nm to a few nanometers and eventually to Co islands. It has been found that SPR peak of Au/Co nanorods can be tuned ranging from 540nm to 820 nm. For Au/Co nanorods with long Co segments SPR peak is shifted to short wavelength as aspect ratio of Co segment increases. For Au/Co-Co islanded nanorods with aspect ratio about two have SPR peaks ranging from 640nm-670nm. Moreover, for Au/Co multilayered nanorods at aspect ratio 3.5 show two SPR peaks at 600nm and 820nm.

The magnetic nanorods were explored for two bioapplications: 1) as magnetic components in orientation-adjustable ferrogel for cell culture, 2) as MRI contrast agent. In ferrogel made of NiFe nanorods embedded in GelMA matrix, VSM measurements confirmed the alignment of the nanorods along applied magnetic field direction during gel curing process. Cytotoxicity of Au/Co nanorods and Au/Co multilayered nanorods was studied via MTT assay in 3T3 fibroblast cells. The results show that cell proliferation decreases as concentration of nanorods increases after cells were incubated with nanorods for 3 days. Also, nanorods tend to aggregate around cells causing cell morphology change. This cytotoxicity suggests the need to cover the nanorods with other inert metals to prevent direct Co exposure. Au/Co multilayered nanorods were coated with Pd, and were tested as contrast agents for MRI. The experimental results clearly show the significant contrast enhancement with the nanorods.

In the future, besides the further exploration of the applications of the multilayered nanorods, two systematic studies are needed to fully understand two new phenomena: 1) the effect of Co layer thickness on the SPR properties of multilayered nanorods. More FDTD computer simulations can reveal the physics behind such effect, and the fabrication and measurements of corresponding structures can verify the simulated results. If successful, it will provide a new way to tune SPR absorption peaks, which will make a big impact in the SPR research field. 2) the large magnetic resonance imaging T2 relaxivity of the multilatered nanorods. More nanorod systems with different lengths of Co and Au layers need to be fabricated, and more experiments are needed to confirm such phenomenon. If it can be confirmed, a theory needs to be developed to explain this important discovery.

References

1. Chen, M., Yamamuro, S., Farrell, D., & Majetich, S. A. (2003). Gold-coated iron nanoparticles for biomedical applications. *Journal of Applied Physics, 93*(10), 7551.
2. Aslam, M., Fu, L., Li, S., & Dravid, V. P. (2005). Silica encapsulation and magnetic properties of FePt nanoparticles. *Journal of Colloid and Interface Science, 290*(2), 444-449.
3. Bai, J., & Wang, J.-P. (2005). High-magnetic-moment core-shell-type FeCo–Au⁄Ag nanoparticles. *Applied Physics Letters, 87*(15), 152502.
4. Brian, L. C., Vladimir, O. G., Marcia, H., Brittany, L. O., Ebony, C., Corey, W. H., & Charles, J. O. C. (2005). Effects of annealing on the magnetic properties, size and strain of gold-coated Permalloy nanoparticles. *Nanotechnology, 16*(9), 1701.
5. Díaz, L., Santos, M., Ballesteros, C., Maryško, M., & Pola, J. (2005). IR laser-induced chemical vapor deposition of carbon-coated iron nanoparticles embedded in polymer. *Journal of Materials Chemistry, 15*(40), 4311. doi: 10.1039/b509365a
6. Fu, W., Yang, H., Chang, L., Li, M., Bala, H., Yu, Q., & Zou, G. (2005). Preparation and characteristics of core–shell structure nickel/silica nanoparticles. *Colloids and Surfaces A: Physicochemical and Engineering Aspects, 262*(1), 71-75. doi: 10.1016/j.colsurfa.2005.03.028

7. Lai, C.-H., Wu, T.-F., & Lan, M.-D. (2005). Synthesis and property of core-shell Ag@Fe3O4 nanoparticles. *IEEE Transactions on Magnetics, 41*(10), 3397-3399. doi: 10.1109/TMAG.2005.855212
8. Liu, W., Zhong, W., Jiang, H. Y., Tang, N. J., Wu, X. L., & Du, W. Y. (2005). Synthesis and magnetic properties of FeNi3/Al2O3 core-shell nanocomposites. *The European Physical Journal B, 46*(4), 471-474.
9. Salgueiriño-Maceira, V., Correa-Duarte, M. A., & Farle, M. (2005). Manipulation of Chemically Synthesized FePt Nanoparticles in Water: Core–Shell Silica/FePt Nanocomposites. *Small, 1*(11), 1073-1076.
10. Hu, M., Chen, J., Li, Z.-Y., Au, L., Hartland, G. V., Li, X., . . . Xia, Y. (2006). Gold nanostructures: engineering their plasmonic properties for biomedical applications. *Chemical Society Reviews, 35*(11), 1084. doi: 10.1039/b517615h
11. Jain, P. K., El-Sayed, I. H., & El-Sayed, M. A. (2007). Au nanoparticles target cancer. *Nano Today, 2*(1), 18-29.
12. Link, S., & El-Sayed, M. A. (2000). Shape and size dependence of radiative, non-radiative and photothermal properties of gold nanocrystals. *TRPC, 19*(3), 409-453. doi: 10.1080/01442350050034180
13. Kelly, K. L., Coronado, E., Zhao, L. L., & Schatz, G. C. (2003). The Optical Properties of Metal Nanoparticles: The Influence of Size, Shape,

and Dielectric Environment. *The Journal of Physical Chemistry B, 107*(3), 668-677. doi: 10.1021/jp026731y

14. Link, S., Mohamed, M. B., & El-Sayed, M. A. (1999). Simulation of the Optical Absorption Spectra of Gold Nanorods as a Function of Their Aspect Ratio and the Effect of the Medium Dielectric Constant. *The Journal of Physical Chemistry B, 103*(16), 3073-3077. doi: 10.1021/jp990183f
15. Sun, L., Hao, Y., Chien, C. L., & Searson, P. C. (2005). Tuning the properties of magnetic nanowires. *IBM Journal of Research and Development, 49*(1), 79-102.
16. Cooper, E. I., Bonhôte, C., Heidmann, J., & Hsu, Y. (2005). Recent developments in high-moment electroplated materials for recording heads. *IBM Journal of Research and Development, 49*(1), 103-126. doi: 10.1147/rd.491.0103
17. Li, C.-Z. L., J.C. (1990). The influence of the packing density on the magnetic behavior of alumite media. *Journal of Magnetism and Magnetic Materials, 88*, 236-246.
18. Schlörb, H., Haehnel, V., Khatri, M. S., Srivastav, A., Kumar, A., Schultz, L., & Fähler, S. (2010). Magnetic nanowires by electrodeposition within templates. *physica status solidi (b), 247*(10), 2364-2379.

19. Shi, J. B., Chen, Y. J., Lin, Y. T., Wu, C., Chen, C. J., & Lin, J. Y. (2006). Synthesis and Characteristics of Fe Nanowires. *Japanese Journal of Applied Physics, 45*(12R), 9075.

20. Yin, A. J., Li, J., Jian, W., Bennett, A. J., & Xu, J. M. (2001). Fabrication of highly ordered metallic nanowire arrays by electrodeposition. *Applied Physics Letters, 79*(7), 1039-1041.

21. Liang, H.-P., Guo, Hu, J.-S., Zhu, C.-F., Wan, L.-J., & Bai, C.-L. (2005). Ni−Pt Multilayered Nanowire Arrays with Enhanced Coercivity and High Remanence Ratio. *Inorganic Chemistry, 44*(9), 3013-3015. doi: 10.1021/ic0500917

22. Choi, J.-r., Oh, S. J., Ju, H., & Cheon, J. (2005). Massive Fabrication of Free-Standing One-Dimensional Co/Pt Nanostructures and Modulation of Ferromagnetism via a Programmable Barcode Layer Effect. *Nano Letters, 5*(11), 2179-2183.

23. Guan, M., & Podlaha, E. J. (2007). Electrodeposition of AuCo alloys and multilayers. *Journal of Applied Electrochemistry, 37*(5), 549-555.

24. Lee, J. H., Wu, J. H., Liu, H. L., Cho, J. U., Cho, M. K., An, B. H., . . . Kim, Y. K. (2007). Iron–Gold Barcode Nanowires. *Angewandte Chemie International Edition, 46*(20), 3663-3667.

25. Chen, M., Searson, P. C., & Chien, C. L. (2003). Micromagnetic behavior of electrodeposited Ni/Cu multilayer nanowires. *Journal of Applied Physics, 93*(10), 8253-8255.
26. Punnakitikashem, P. (2011). *Templated Synthesis and Characterizations of High Moment Magnetic Nanoparticles for Bioapplications.* (Ph.D.), University of texas at Arlington.
27. Doefman, J., & Frenkel, J. (1930). Spontaneous and Induced Magnetisation in Ferromagnetic Bodies. *Nature, 126*(3173), 274-275. doi: 10.1038/126274a0
28. Leslie-Pelecky, D. L., & Rieke, R. D. (1996). Magnetic Properties of Nanostructured Materials. *Chemistry of Materials, 8*(8), 1770-1783.
29. Mie, G. (1908). Beiträge zur Optik trüber Medien, speziell kolloidaler Metallösungen. *Annalen der Physik, 330*(3), 377-445.
30. Gans, R. (1912). Über die Form ultramikroskopischer Goldteilchen. *Annalen der Physik, 342*(5), 881-900.
31. Yin, A. J., Li, J., Jian, W., Bennett, A. J., & Xu, J. M. (2001). Fabrication of highly ordered metallic nanowire arrays by electrodeposition. *Applied Physics Letters, 79*(7), 1039-1041.
32. Ono, S., Saito, M., & Asoh, H. (2005). Self-ordering of anodic porous alumina formed in organic acid electrolytes. *Electrochimica Acta, 51*(5), 827-833.

33. Ono, S., Saito, M., Ishiguro, M., & Asoh, H. (2004). Controlling Factor of Self-Ordering of Anodic Porous Alumina. *Journal of the Electrochemical Society, 151*(8), B473.
34. Gösele, U., Nielsch, K., Lee, W., & Ji, R. (2006). Fast fabrication of long-range ordered porous alumina membranes by hard anodization. *Nature Materials, 5*(9), 741-747. doi: 10.1038/nmat1717
35. Eftekhari, A. (2008). *Nanostructured materials in Electrochemistry*: WILEY-VCH.
36. Han, C. Y., Willing, G. A., Xiao, Z., & Wang, H. H. (2007). Control of the Anodic Aluminum Oxide Barrier Layer Opening Process by Wet Chemical Etching. *Langmuir, 23*(3), 1564-1568.
37. Han, C. Y., Willing, G. A., Xiao, Z., & Wang, H. H. (2007). Control of the Anodic Aluminum Oxide Barrier Layer Opening Process by Wet Chemical Etching. *Langmuir, 23*(3), 1564-1568.
38. Na, W., Wen-Di, Z., Ji-Peng, X., Bin, M., Zong-Zhi, Z., Qing-Yuan, J.,Bochem, H. P. (2010). Fabrication of Anodic Aluminum Oxide Templates with Small Interpore Distances. *Chinese Physics Letters, 27*(6), 066801.
39. Han, X. Y., & Shen, W. Z. (2011). Improved two-step anodization technique for ordered porous anodic aluminum membranes. *Journal of Electroanalytical Chemistry, 655*(1), 56-64.

40. Tian, Z.-P., Lu, K., & Chen, B. (2010). Unique nanopore pattern formation by focused ion beam guided anodization. *Nanotechnology, 21*(40), 405301.
41. Michalska-Domańska, M., Norek, M., Stępniowski, W. J., & Budner, B. (2013). Fabrication of high quality anodic aluminum oxide (AAO) on low purity aluminum—A comparative study with the AAO produced on high purity aluminum. *Electrochimica Acta, 105*, 424-432.
42. Aerts, T., De Graeve, I., & Terryn, H. (2008). Study of initiation and development of local burning phenomena during anodizing of aluminium under controlled convection. *Electrochimica Acta, 54*(2), 270-279.
43. Kelly, K. L., Coronado, E., Zhao, L. L., & Schatz, G. C. (2003). The Optical Properties of Metal Nanoparticles: The Influence of Size, Shape, and Dielectric Environment. *The Journal of Physical Chemistry B, 107*(3), 668-677.
44. Huang, X., & El-Sayed, M. A. (2010). Gold nanoparticles: Optical properties and implementations in cancer diagnosis and photothermal therapy. *Journal of Advanced Research, 1*(1), 13-28.
45. Fox, M. (2008). *Optical Properties of Solids*. Great Britain: Oxford University press.
46. Ashcroft, N. W., & Mermin, N. D. *Solid State physics*. United States of America: Thomson Learning, Inc.

47. Link, S., Mohamed, M. B., & El-Sayed, M. A. (1999). Simulation of the Optical Absorption Spectra of Gold Nanorods as a Function of Their Aspect Ratio and the Effect of the Medium Dielectric Constant. *The Journal of Physical Chemistry B, 103*(16), 3073-3077.
48. Lumerical Solutions, I. *FDTD Solutions User manual*.
49. Johnson, & Christy. Refractive Index.info http://refractiveindex.info/?shelf=main&book=Co&page=Johnson
50. KAMINSKIENĖ, Ž., PROSYČEVAS, I., STONKUTĖ, J., & GUOBIENĖ, A. (2013). Evaluation of Optical Properties of Ag, Cu, and Co Nanoparticles Synthesized in Organic Medium. *ACTA PHYSICA POLONICA A*, *123*(1), 111-114.
51. Scaffardi, L. B., Pellegri, N., Sanctis, O. d., & Tocho, J. O. (2005). Sizing gold nanoparticles by optical extinction spectroscopy. *Nanotechnology, 16*(1), 158.
52. Bender, P., Günther, A., Tschöpe, A., & Birringer, R. (2011). Synthesis and characterization of uniaxial ferrogels with Ni nanorods as magnetic phase. *Journal of Magnetism and Magnetic Materials, 323*(15), 2055-2063.
53. Schulz, L., Schirmacher, W., Omran, A., Shah, V. R., Böni, P., Petry, W., & Müller-Buschbaum, P. (2010). Elastic torsion effects in magnetic

nanoparticle diblock-copolymer structures. *Journal of Physics: Condensed Matter*, *22*(34), 346008.

54. Snyder, R. L., Nguyen, V. Q., & Ramanujan, R. V. (2010). Design parameters for magneto-elastic soft actuators. *Smart Materials and Structures, 19*(5), 055017.
55. Monz, S., Tschöpe, A., & Birringer, R. (2008). Magnetic properties of isotropic and anisotropic CoFe2O4-based ferrogels and their application as torsional and rotational actuators. *Physical review.E, Statistical, nonlinear, and soft matter physics, 78*(2 Pt 1), 021404.
56. Szabó, D., Szeghy, G., & Zrínyi, M. (1998). Shape Transition of Magnetic Field Sensitive Polymer Gels. *Macromolecules*, *31*(19), 6541-6548.
57. Gollwitzer, C., Turanov, A., Krekhova, M., Lattermann, G., Rehberg, I., & Richter, R. (2008). Measuring the deformation of a ferrogel sphere in a homogeneous magnetic field. *The Journal of Chemical Physics*, *128*(16), 164709.
58. Gonzalez, J., Hoppe, C., Muraca, D., Sánchez, F., & Alvarez, V. (2011). Synthesis and characterization of PVA ferrogels obtained through a one-pot freezing–thawing procedure. *Colloid and Polymer Science, 289*(17-18), 1839-1846.

59. Lao, L. L., & Ramanujan, R. V. (2004). Magnetic and hydrogel composite materials for hyperthermia applications. *Journal of Materials Science: Materials in Medicine, 15*(10), 1061-1064.
60. Babincová, M., Leszczynska, D., Sourivong, P., Čičmanec, P., & Babinec, P. (2001). Superparamagnetic gel as a novel material for electromagnetically induced hyperthermia. *Journal of Magnetism and Magnetic Materials, 225*(1–2), 109-112.
61. Nichol, J. W., Koshy, S. T., Bae, H., Hwang, C. M., Yamanlar, S., & Khademhosseini, A. (2010). Cell-laden microengineered gelatin methacrylate hydrogels. *Biomaterials, 31*(21), 5536-5544.
62. Ramon-Azcon, J., Ahadian, S., Obregon, R., Camci-Unal, G., Ostrovidov, S., Hosseini, V., Matsue, T. (2012). Gelatin methacrylate as a promising hydrogel for 3D microscale organization and proliferation of dielectrophoretically patterned cells. *Lab on a Chip, 12*(16), 2959-2969.
63. Fairbanks, B. D., Schwartz, M. P., Bowman, C. N., & Anseth, K. S. (2009). Photoinitiated polymerization of PEG-diacrylate with lithium phenyl-2,4,6-trimethylbenzoylphosphinate: polymerization rate and cytocompatibility. *Biomaterials, 30*(35), 6702-6707.
64. TL, R., RA, M., & al., N. A. e. (2013). *Cell Viability Assays* M. L (Ed.) Retrieved from http://www.ncbi.nlm.nih.gov/books/NBK144065/

65. Pankhurst, Q. A., Connolly, J., Jones, S. K., & Dobson, J. (2003). Applications of magnetic nanoparticles in biomedicine. *Journal of Physics D: Applied Physics, 36*(13), R167-R181.
66. Lee, N., & Hyeon, T. (2012). Designed synthesis of uniformly sized iron oxide nanoparticles for efficient magnetic resonance imaging contrast agents. *Chemical Society Reviews*.
67. Lawaczeck, R., Menzel, M., & Pietsch, H. (2004). Superparamagnetic iron oxide particles: contrast media for magnetic resonance imaging. *Applied Organometallic Chemistry*, *18*(10), 506-513.
68. Hesselink, J. R.). BASIC PRINCIPLES OF MR IMAGING. from http://spinwarp.ucsd.edu/neuroweb/Text/br-100.htm
69. VanMeter, J. Basics of Magnetic Resonance Imaging https://cfmi.georgetown.edu/downloads/training/2/MRI-basics.pdf

Biographical Information

Orathai Thumthan was born in Sisaket, Thailand on 25 December 1981. She received her B.Sc. degree in Physics from Ubon Rachathani University in 2004. In fall2007, she stated her Master degree in Materials Science and Engineering in University of Texas at Arlington and pursued her Ph.D. degree in 2009. During her study at UTA, she also worked as research assistant for Dr.Yaowu Hao. Her research area is in magnetic nanoparticles for bioapplications.